

Microfabricated Fuel Cells as Power Sources for MEMS



Juan Pablo Esquivel Bojorquez



Microfabricated Fuel Cells as Power Sources for MEMS

Memoria presentada para optar al título de:

Doctor en Ingeniería Electrónica

Por:

Juan Pablo Esquivel Bojorquez

Director:

Neus Sabaté Vizcarra

Tutor:

Marc Porti Pujal

Noviembre 2010

La presente tesis doctoral titulada “*Microfabricated Fuel Cells as Power Sources for MEMS*” ha sido realizada por Juan Pablo Esquivel Bojorquez dentro del programa de Doctorado en Ingeniería Electrónica de la Universidad Autónoma de Barcelona bajo la dirección de la Dra. Neus Sabaté Vizcarra del Instituto de Microelectrónica de Barcelona, IMB-CNM (CSIC) y bajo la tutela del Dr. Marc Porti Pujal del Departamento de Ingeniería Electrónica de la Universidad Autónoma de Barcelona.

Bellaterra, Noviembre 2010

Neus Sabaté Vizcarra

Marc Porti Pujal

Para todos con los que comparto este viaje

Acknowledgements

In the following lines I would like to express my appreciation to the people who have contributed to make this thesis possible.

First of all, I gratefully acknowledge my supervisor, Dr. Neus Sabaté, for thrusting in me, taking risks and teach me to enjoy the process. I thank her for giving me the opportunity to *get on the ship* and then allow me to *steer* it a little bit sometimes. I appreciate her enthusiasm, friendship and support in and out of the laboratory. Although I was the first student under her charge, she has performed the duty with a natural expertise. I strongly recommend the experience to all those under graduate students seeking for a project. One could hardly find a better supervisor.

I would like to express my gratitude to Dr. Carles Cané for his support and advice as our scientific guru. Also to the rest of the microDMFC team, Dr. Joaquin Santander to start with the fuel cell frenzy and Nuria Torres for her endless willingness to help. Special thanks to Dr. Albert Tarancón, his fleeting but fruitful stay in our group represented an important injection of energy. I would like to thank Johannes Hauer for his valuable and enthusiastic assistance during this last year. Thanks also to the rest of the Gas Sensors Group for all their help and brainstorming sessions (with and without pizzas). Additionally, I would like to thank Dr. F. Xavier Muñoz for responding my call and send me to the right people, Dr. Javier del Campo for his absolute availability in case of any electrochemical emergency and Dr. Neus Godino for sharing the joy of finite element modeling.

A lot of people have contributed to providing a nice working atmosphere at IMB-CNM. I feel very fortunate for having shared this time with my officemates and fellow students. I can say that among these people I have found more than colleagues but very good friends.

During the course of this work many processes were performed in the IMB-CNM clean room, I thank the technical staff for making this possible. A special mention goes to Marta Duch and Marta Gerbolés from the Microsystems Lab, for their helpful and immeasurable assistance. In addition I would like to recognize the IMB-CNM administrative staff for their availability, kindness and support solving urgent problems, making urgent purchases or urgent travel arrangements. Also the library staff who guided me to find out all kinds of information.

The work developed in this thesis has been certainly multidisciplinary and would have not been achieved without the collaboration with several external groups. I would like to acknowledge Dr. Jordi Mas from UAB, for his help in the microbial field, and Diana Dávila for starting together this particular adventure and overcome the adversities presented in the way.

I am indeed grateful to the staff of the AZM at the Helmholtz Zentrum Berlin for supplying all the resources to develop my projects during both of my stays in that institute. I thank Dr. Marcus Lörger and Dr. Bernd Löchel for their warm welcome and full support. A very special thank goes to Tobias Senn for all his help and overwhelming effectiveness, which made possible many of the developments in this collaboration. I would also like to thank Dr. Sergio Rojas and Dr. Patricia Hernández from ICP (CSIC) for their help with the catalysts deposition and Dr. Marc Castellarnau from IBEC for his ideas, orientation and characterization of microfluidic components.

Now I wish to thank my family, my parents and sisters, to whom I dedicate this thesis. My deepest gratitude goes for their unconditional support in all the projects of my life, their endless patience, understanding and encouragement when it was most required, no matter the distance. These efforts have been done to make you feel proud of me.

Finally, I thank Nerea for taking such a good care of me during the tough writing period. I cannot thank you enough. I hope we never get tired of *walking* together. ><

INDEX

1. Introduction	1
1.1 Fuel Cell Working Principle	3
1.2 Micro Fuel Cell Characterization	7
1.3 Summary	10
References.....	12

SECTION I.

MICRO FUEL CELL TECHNOLOGY INSIGHT: from MACRO to MICRO

2. Hybrid Micro Fuel Cell	17
2.1 Device design and assembly	17
2.1.1 Membrane Electrode Assembly	18
2.1.2 Silicon current collectors.....	20
2.1.3 Device packaging and assembly	22
2.2 Micro Fuel Cell Characterization	24
2.2.1 Measurement setup	24
2.2.2 Influence of operating conditions on fuel cell performance	25
2.2.2.1 Methanol concentration	25
2.2.2.2 Temperature	28
2.2.2.3 Device orientation	30
2.2.3 Influence of current collectors geometry on fuel cell performance	31
2.2.3.1 Influence of current collector geometry on power density.....	33
2.2.3.2 Influence of current collector geometry on measurement repeatability.....	35
2.2.4 Fuel cell efficiency.....	39
2.2.4.1 Fuel cell operated at constant current	40
2.2.4.2 Fuel cell operated at constant voltage	41
2.3 Micro Fuel Cell Modeling	44
2.3.1 Model description	44
2.3.1.1 Mass transport in anode side	46
2.3.1.2 Mass transport in membrane	47
2.3.1.3 Mass transport in cathode side	48
2.3.1.4 Electrochemical kinetics	49
2.3.1.5 Cell performance.....	50
2.3.2 Validation	50
2.3.2.1 Polarization curves	50
2.3.2.2 Methanol consumption and fuel cell efficiency	51
2.4 Discussion and summary	54
References	56

**SECTION II.
TECHNOLOGY INNOVATIONS ON FUEL CELL COMPONENTS TOWARDS A COMPACT
DEVICE**

3. Silicon-PDMS Micro Fuel Cell	61
3.1 Device design	62
3.2 Silicon current collectors design and fabrication	63
3.2.1 Silicon microfabrication process	64
3.2.2 Catalyst electrodeposition	66
3.3 Hybrid polymer electrolyte membrane	71
3.3.1 Membrane fabrication process	71
3.3.2 Proton conductivity characterization	75
3.4 Fuel cell assembly and characterization	77
3.5 Discussion and summary	81
References	82
4. SU-8 Micro Fuel Cell	85
4.1 Description of device design	85
4.2 Fabrication and characterization of SU-8 fuel cell components	87
4.2.1 Fabrication of the Membrane Electrode Assembly	87
4.2.1.1 SU-8 Porous structure	88
4.2.1.2 Nafion [®] -filled SU-8 membranes	89
4.2.1.3 Carbon-based electrode layers	91
4.2.2 Fabrication of fuel cell current collectors	92
4.3 Micro fuel cell assembly and characterization	93
4.4 Discussion and summary	97
References	98
5. Fuel delivery system for liquid-fed micro fuel cell	99
5.1 Device design	100
5.2 Fabrication process	101
5.3 Fluidic characterization	106
5.4 Discussion and summary	109
References	110

SECTION III.**MICRO FUEL CELL APPLICATIONS**

6. Microfabricated Microbial Fuel Cell	115
6.1 Microbial Fuel Cell working principle	115
6.2 Device assembly and characterization	117
6.2.1 Assembly and system set-up of macro MFC	117
6.2.2 Characterization of macro MFC	119
6.2.3 Micro MFC fabrication and assembly	121
6.2.4 Micro MFC performance characterization	122
6.3 Microfabricated MFC as toxicity biosensor	125
6.3.1 Biosensors for toxicity measurement	126
6.3.2 Toxicity sensing application	126
6.4 Discussion and summary	128
References	129
7. Fuel cell-powered microfluidic platform for Lab-on-a-Chip applications	131
7.1 Design and fabrication of the system	133
7.1.1 Microfluidic system fabrication	135
7.2 Microfluidic platform characterization	138
7.2.1 Preliminary testing of micropumps	138
7.2.2 Characterization of microfluidic platform power and flow rates	141
7.2.2.1 Volume transfer measurement	142
7.2.2.2 Particle image velocimetry analysis	143
7.3 Discussion and summary	147
References	148
Conclusions	151
List of publications	153
Appendix	155
Resumen en español	157
List of abbreviations	159

1. Introduction

The vast proliferation of MEMS/NEMS (Micro and Nano Electro-Mechanical Systems) in the last decade, has led to the miniaturization of many components - that were formerly built by standard fabrication methods - and has raised the development of a big variety of new applications. Among them, the most mature include RF communications (antennas, resonators, filters), biotechnology (DNA amplification, identification), biomedical (pressure sensors, neuronal detection/stimulation) and inertial sensing (accelerometers, gyroscopes) [1, 2]. Moreover, the emerging integration technologies together with the rapid evolution of nanoelectronics have increased radically the functional density and computational power in constantly shrinking volumes and power consumptions.

The possibility of integrating microsystems and nanosystems with diverse functionalities into a single component together with the associated signal processing and transmission modules has led to the concept of *Smart System*. Such systems are envisaged to interact with their surrounding environment by performing sensing, actuating and diagnosis functions. They are also expected to be capable of taking decisions, networked and energy autonomous [3]. Figure 1.1 shows a schematic diagram of the composition of a Smart System.

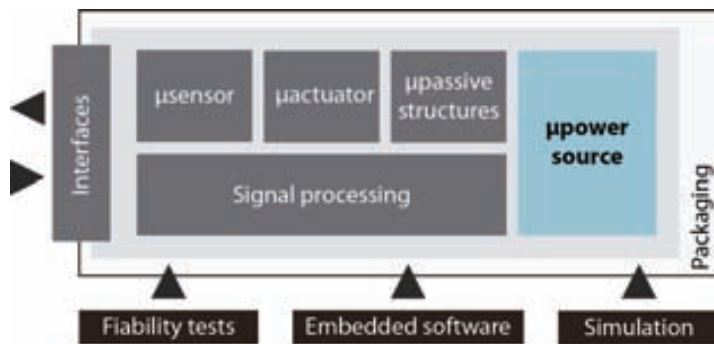


Figure 1.1 Smart System components.

In order to provide the Smart System with the required autonomy, its power supply must be integrated within the same system packaging or at least, built in similar dimensions. This has impelled the search of a new generation of integrated power sources that satisfy the requirements of high power density, long operation lifetime and low cost. Several solutions have been proposed to overcome these challenges by applying MEMS-based fabrication technologies. Most of the works reporting

these powering devices, known as powerMEMS, have focused on the development of energy scavenging microsystems [4], microreactors [5], microbatteries [6] and micro fuel cells [7].

Energy scavenging systems convert the energy from their surroundings (thermal, electromagnetic, vibrations) into electrical energy. These systems – whose ability to be scaled down successfully by microfabrication technologies has been widely proved – are always limited to the presence of the external source of energy, which obligate in most cases to have a secondary powering source to guarantee a continuous power supply to the system. In contrast, electrochemical power sources – such as batteries, fuel cells and supercapacitors – offer the advantage of delivering energy in a continuous way. As it can be seen in Figure 1.2, miniaturized power sources are nowadays capable of generating a wide range of power densities and output voltages depending on their working principle and the limitations of the state-of-the-art technology.

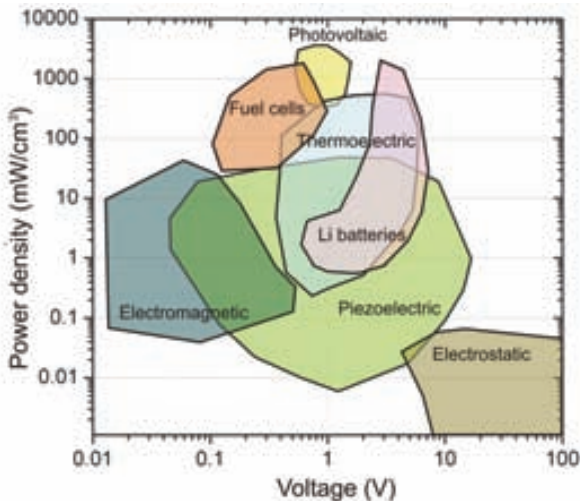


Figure 1.2 Specific power density versus voltage of the different portable power sources, updated from [8].

Among electrochemical-based power sources, batteries are currently the most well-established ones, enabling the wealth of battery powered wireless systems (laptops, smart phones, mp3 players, GPS systems...). However, they are facing difficulties to keep up with the ratio of miniaturization of microsystems. In a hand-held portable application, the size of the power source is usually occupied by 30-50% the total size of the system. In the microscale, the drastic reduction of the devices dimensions makes the battery become the largest part of the system due to the direct relation between energy storage capacity and the electrode size. In this sense, micro fuel cells promise to provide a longer operation times than batteries due to the high energy density associated to their fuel (Table 1.1). Since the energy is stored in a fuel reservoir aside from the fuel cell body, these devices offer the advantage of allowing an instant recharge, which is very convenient regarding their application to MEMS

powering. Therefore, current research in this field is focused on the achievement of higher integrated devices that minimize the volume ratio between fuel cell and fuel reservoir as well as the improvement of their efficiency by finding new strategies to fabricate MEMS-compatible components.

Table 1.1 Energy density comparison of various fuels to practical battery power sources, adapted from [9].

Technology	Energy density (Wh/l)	Energy density (Wh/kg)
Primary batteries		
Alkaline	330	125
Zn-air	1050	340
Secondary batteries		
NiMH	175	50
Li-ion	200	120
Li-polymer	350	200
Fuels		
Hydrogen (300 bar)	1690	2805
Methanol	4384	5600
Ethanol	6660	8300

This thesis is devoted to the development of micro fuel cells architectures and components based in technologies compatible with microsystems fabrication. The work was focused in Polymer Electrolyte Membrane Fuel Cells (PEMFCs), particularly attractive due to their capability of working at room temperature using both hydrogen and liquid fuels, such as methanol. This represents an important advantage for portable applications due to the great simplification of fuel storage and handling processes. The following section presents the basic concepts of the fuel cell operation as well as the characterization procedure used along this thesis.

1.1 MICRO FUEL CELL WORKING PRINCIPLE

A micro fuel cell is an electrochemical device that converts the chemical energy of a fuel into electric energy and heat, as long as the reactants are supplied [10]. One of the key components of a fuel cell is its electrolyte and generally, fuel cells are classified depending on the electrolyte employed, e.g., Solid Oxide Fuel Cell (SOFC), Molten Carbonate Fuel Cell (MCFC), Phosphoric Acid Fuel Cell (PAFC), Proton Exchange Membrane Fuel Cell (PEMFC) and in second term, they are distinguished by the type of fuel used e.g. Direct Alcohol Fuel Cells (DAFC) or by the nature of the catalysts employed (BioFC). Table 1.2 summarizes the basic information about these systems, mainly their operating conditions, kind of electrolyte, fuel employed and type of catalysts used in the electrodes.

Table 1.2 Basic description of fuel cells types.

Fuel cell type	Mobile ion	Electrolyte operating temperature	Catalyst	Fuel compatibility	Applications
Alkaline (AFC)	OH ⁻	50 – 200 °C	Platinum	H ₂	Space vehicles
Polymer electrolyte membrane (PEMFC)	H ⁺	30– 100 °C	Platinum	H ₂ , alcohols	Vehicles, mobile applications, low power CHP systems
Biological (BioFC)	H ⁺	30– 100 °C	Enzymes, bacteria	Glucose, acetate, lactate, etc.	Biosensors, waste water treatment
Phosphoric acid (PAFC)	H ⁺	~ 200 °C	Platinum	H ₂	200-kW CHP systems
Molten carbonate (MCFC)	CO ₃ ²⁻	~ 650 °C	Nickel	H ₂ , CH ₄	Medium to large scale CHP systems
Solid oxide (SOFC)	O ²⁻	500–1000 °C	Perovskites (ceramic)	H ₂ , CH ₄ , CO	2kW – MW CHP systems

Among the different types of fuel cells, SOFC and PEMFC are the most promising technologies regarding miniaturization. The interest of micro solid oxide fuel cells is related to their promise of high power densities by using hydrocarbons as fuel without the need of Pt for their catalysis; however, the downscaling of these devices has to overcome different technological challenges such as the thermomechanical stability of thin-film ceramics or the hermetic sealing at the typical operating temperatures of these devices (450-500 °C) [11]. Due to their capability of working at ambient conditions (room temperature and atmospheric pressure), PEM fuel cells are the most widely miniaturized regarding microsystems applications.

The basic structure of a PEMFC can be described as a Membrane Electrode Assembly (MEA) placed between two conducting plates. The MEA consists of a proton conductive polymer electrolyte membrane (typically Nafion[®]) covered on both sides by porous carbon-based electrodes containing the catalyst loads that enhance the chemical reaction. The MEA is put in contact with the plates, which in addition of providing mechanical support to the structure, collect the electron current generated at the electrodes and distribute the fuel towards the membrane. Figure 1.3 shows a schematic diagram of a PEM fuel cell. During normal operation of a PEMFC, hydrogen gas flows across the anode and diffuses through the porous backing until it reaches the active layer, where the catalysts break the molecule into electrons and protons. Electrons are collected at the anode side, establishing a current that can be derived to an external load in order to generate the required power. Meanwhile, protons cross the electrolyte membrane towards the cathode where they recombine with oxygen molecules and the electrons coming from the external circuit to produce water. The overall fuel cell reaction is:



Depending on the origin and nature of the fuel, PEM fuel cells can use both direct and indirect energy conversion methods. Direct conversion may involve fuels such as hydrogen, methanol, ethanol, formic acid, ethylene glycol and sodium borohydride that are converted into electrons through a direct fuel cell system. Indirect conversion method is based in a reformation of complex gas molecules to H₂ followed by a feeding of the reformat gas into fuel cell. However, this last option requires the addition of an extra reform-unit to the system that increases its complexity. On the other hand, direct pure hydrogen feeding is relatively difficult for the application of electronic equipment due to storage problem (lack of efficient hydrogen storage material) in small volumes. There is also concern in terms of safety while carrying hydrogen in wireless portable electronic equipment. The setup of a cost-effective, appropriate infrastructure for hydrogen canister is another major challenge for which most hurdles are unlikely to be overcome in the foreseeable future.

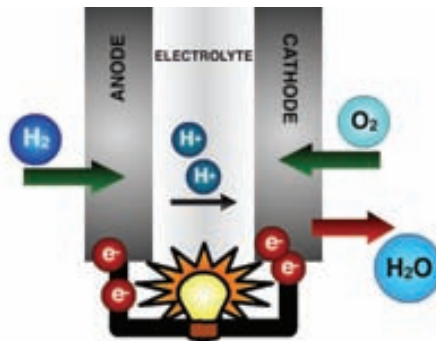
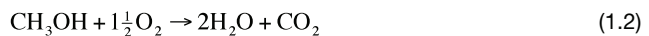


Figure 1.3 Schematic diagram showing the main parts and operation of a PEM fuel cell.

In this sense, the use of liquid fuels has proved to overcome successfully this problem and offers several advantages, mainly related to its higher energy density and easier handling [10]. The DMFC is a particular type of PEMFC that uses the hydrogen contained in the methanol molecule to produce energy. Compared to hydrogen-driven PEMFC, this kind of fuel cell has the advantage of using a liquid fuel which simplifies the difficulties associated to the fuel storage and handling. However, the catalysis of methanol – a carbon containing molecule – generates carbon dioxide (CO₂) as a side product. CO₂ is produced during the middle stages involved in the anode reaction and therefore its degassing has to be ensured in order to avoid the blocking of reaction sites. The overall reaction of the direct methanol fuel cell is:



Depending on the way methanol is supplied, fuel cells can be classified in two groups: active and passive fuel cells. In active fuel cells, the fuel is provided by external pumping systems creating a continuous flow of reactants, whereas in passive fuel cells a reservoir is filled with a fixed volume of fuel that is used until its consumption [12]. In contrast with active systems where the fuel is supplied with a constant flux where the same concentration and pressure conditions are maintained continuously, in a passive fuel cell, fuel distribution relies on diffusion.

The miniaturization of fuel cells by using silicon-related microtechnologies is a research field relatively new with no more than a decade. In the last few years, microPEM fuel cells yielding competitive power outputs have been reported [7, 13-17]. Generally these devices are implemented with a broad range of materials, operated in a wide range of temperatures (25-90 °C) and use either passive or active delivery of reactants. Table 1.3 summarizes some of the most significant micro fuel cell approaches reported. The efficiency of these devices is usually difficult to evaluate as in most of these works there is a lack of balance-of-plant computation, i.e. the subtraction of the power consumed by the ancillary systems, components and structures that provide the fuel cells of an incoming fuel flow or a determined operating temperature, which clearly reduces the net power obtained from the device. This is somehow easier in passive fuel cells, because although the elimination of the ancillary devices needed to provide the flux of fuel lowers the device performance, it simplifies the system as well as its balance-of-plant. In fact, in a passive approach, the overall DMFC system becomes more compact and easier to integrate with other silicon-based device. Furthermore, if operated at ambient temperature and with air-breathing conditions at the cathode side the fuel cell generates a net power output with typical values around 5-10 mW/cm². However, passive fuel delivery makes design and optimization of the architecture and microfluidic structures of the microdevice a critical issue, which is still being investigated.

Table 1.3 Experimental micro PEM fuel cell approaches.

Fuel	Fuel delivery	Max. Power density (mW/cm ²)	Operating temperature	Anode Catalyst	Main Feature	Ref.
H ₂	Active	80	25 °C	Pt	Flexible architecture	[18]
H ₂	Active	37	40 °C	Pt	Porous silicon electrodes	[19]
H ₂	Active	315	25 °C	Pt 1 mg/cm ²	PMMA flow structures	[20]
H ₂	Active	0.35	25 °C	Pt 5nm	PDMS casing	[21]
H ₂	Active	75	25 °C	Pt	Carbon nanotubes GDL	[22]
H ₂ (LiAlH ₄)	Passive	78	25 °C	Pt 20 mg/cm ²	Metal hydride reaction	[23]
MeOH	Active	0.33	25 °C	Pt-Ru 5 mg/cm ²	Photosensitive glass substrate	[24]
MeOH	Active	0.78	25 °C	Pt-Ru 2.85 mg/cm ²	Anodic bonding Pyrex	[25]
MeOH	Active	0.38	25 °C	Pt-Ru 2.5 mg/cm ²	Si collectors, electroplating	[26]
MeOH	Active	16.5	23 °C	Pt-Ru 4-6 mg/cm ²	Silicon flow channels	[27]
MeOH	Active	8	68 °C	Pt-Ru 3.3 mg/cm ²	Polymer current collectors	[28]
EtOH	Passive	8.1	25 °C	Pt 80-200 nm	Porous silicon current collectors	[29]

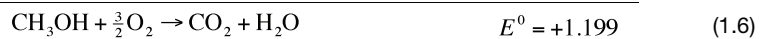
1.2 MICRO FUEL CELL CHARACTERIZATION

The performance of a fuel cell is described mainly by its Intensity-Voltage (I-V) curve. An ideal fuel cell would supply any amount of current at a constant voltage determined by thermodynamics. The thermodynamic potential of the fuel cell is given by the Nernst equation, which outlines how the reversible electrochemical cell voltages vary as a function of different parameters such as species concentration, pressure, etc. The equation takes the general form:

$$E = E^0 - \frac{RT}{nF} \ln \frac{\prod a_{\text{products}}^{v_i}}{\prod a_{\text{reactants}}^{v_i}} \quad (1.3)$$

where E^0 is the standard-state reversible voltage, R is the gas constant, T is temperature, n is the number of moles of electrons transferred, F is the Faraday constant, a is the activity of the species depending on its chemical nature and v_i is the stoichiometric coefficient of the specie.

In a direct methanol fuel cell the standard-state reversible potential is calculated from the individual potentials of the two half reactions in the cell:



However, in practice the voltage obtained from a fuel cell is lower than the electrochemical voltage associated to the overall chemical reactions taking place in the fuel cell. This is due to the existence of several additive irreversible losses associated to different physical factors.

These limitations give the I-V curve the characteristic shape shown in Figure 1.4 and can be classified in three types according to their nature and the region of the curve where they show their effects:

- a) *Activation losses* due to electrochemical reaction
- b) *Ohmic losses* due to ionic and electronic conduction
- c) *Concentration losses* due to mass transport

The losses on each of the three curve regions associated to different fuel cell parameters can be minimized by different means as described in Table 1.4.

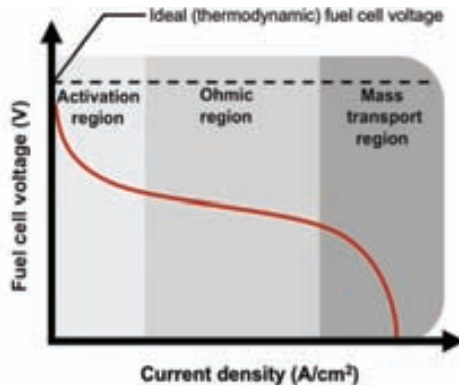


Figure 1.4 Fuel cell polarization curve indicating the different regions, from [30].

Table 1.4 Different fuel cell limitations affecting its performance.

Type of the loss	Minimized by
Activation losses	Increase fuel concentration Increase temperature Increase catalyst load Increase reaction sites
Ohmic losses	Reduce resistance (electrodes, electrolyte, interconnects...) Reduce electrolyte thickness Increase electrodes conductance Increase pressure of assembly
Concentration losses	Optimize mass transport: Electrodes (diffusion), Flow structures (convection)

Taking into consideration all of this different losses the output power that can be obtained from a fuel cell can be written as follows:

$$V = E_{thermo} - \eta_{act} - \eta_{ohmic} - \eta_{conc} \quad (1.7)$$

where V is the output fuel cell voltage, E_{thermo} is the ideal thermodynamic potential, η_{act} , η_{ohmic} and η_{conc} correspond to the activation, ohmic and concentration losses respectively associated to the different regions of the curve. The aspects emphasized in bold in the previous table are the ones being explored in the present thesis - either directly or indirectly- as they are associated to operating conditions, current collector geometry, electrode and electrolyte properties and final device assembly.

One of the main aspects to evaluate fuel cell performance is the generated output power. Values of current and power are given per unit of active area of the fuel cell in order to allow comparison of the performance between different device architectures as well as larger scale fuel cells. The Figure 1.5 shows a typical set of voltage-intensity and power-intensity polarization curves.

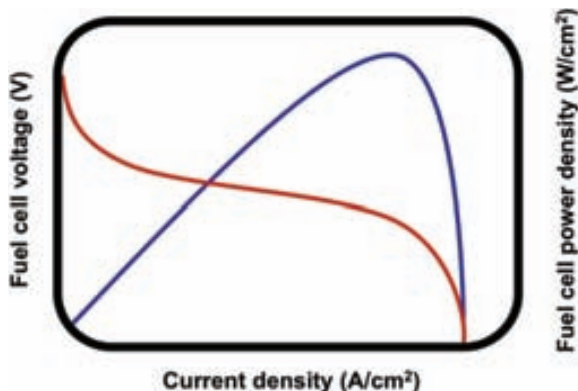


Figure 1.5 Typical polarization curves of a fuel cell. Adapted from [30].

There are two distinct aspects in a passive direct methanol fuel cell that have a visible effect in the device performance. On one hand, the fact that mass transport of reactants to the electrodes of the cell is mainly diffusion-driven stresses the need of optimized flow structures that enhance fuel transport and avoid the accumulation of reaction products like water and carbon dioxide in the electrodes. Yet, it can be expected that in comparison with active systems [17], passive fuel cells deliver lower power densities due to the absence of a convective flux that continuously renews the fuel concentration. However, the elimination of the power consumption associated to the auxiliary devices needed to maintain that flow can result in a positive balance of plant for certain optimized passive fuel cell designs.

Besides, the fact that the polymer electrolyte membrane is not completely impermeable to methanol affects also significantly to fuel cell performance. When the fuel reservoir is filled with methanol a fraction of the fuel crosses from anode to cathode through the electrolyte because of the combined effect of molecular diffusion and electro-osmotic drag. This phenomenon is called methanol crossover effect. It results not only in a fuel loss, but also a decrease in the overall cell voltage due to the mixed potential on the cathode caused by the methanol reaction with the Pt in the catalyst layer. Furthermore, this reaction releases CO molecules that block the catalyst reaction sites in the cathode reducing even more the performance of the fuel cell [31]. Methanol crossover depends on different factors, being the most important ones the membrane permeability and thickness [32], the concentration of methanol [33], the operating temperature [34] and the catalyst load in the electrodes [35]. The crossover effect plays a major role in passive fuel cells performance because it causes a decrease in the methanol concentration even when the fuel cell is not in operation. Finally, it has to be mentioned that all μ DMFCs developed in this work are intended to operate as a simple and compact power source. For this reason the characterization of the devices was performed pointing toward the target conditions: room temperature - in order to avoid the need of heating systems - and the use of oxygen taken directly from air.

1.3 SUMMARY

This thesis presents the first developments and technological contributions to the micro fuel cell field performed at IMB-CNM (CSIC). Particularly, this work is dedicated to the design and fabrication of micro fuel cells as power sources to be integrated within the microsystems to be powered. The work is organized in seven chapters: the current introductory chapter and six experimental chapters that have been divided in three sections. A graphic representation of the thesis organization is presented in Figure 1.7.

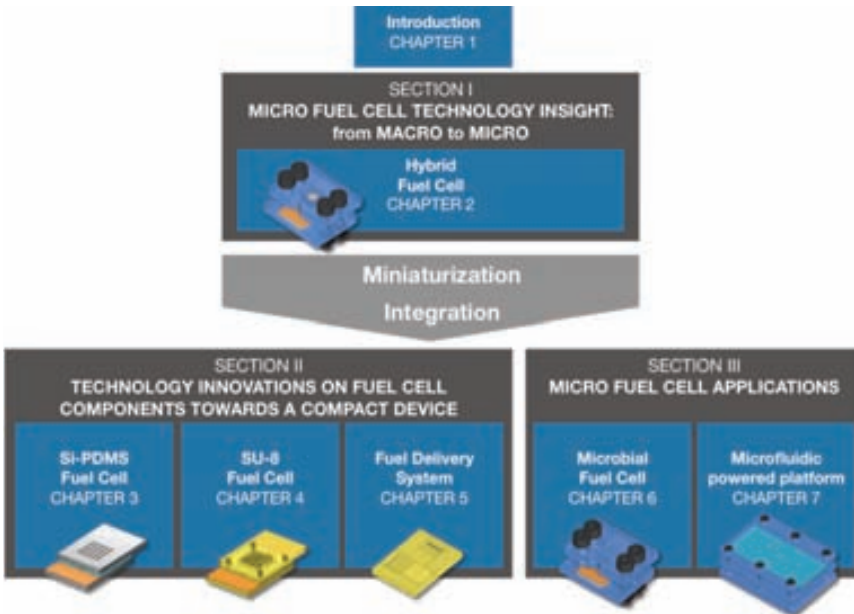


Figure 1.7 Schematic summary of the thesis contents and chapter organization.

The first section (Chapter 2) is devoted to the development of a micro direct methanol fuel cell by using a hybrid approach in which some components of the fuel cell are fabricated in silicon with the use of microfabrication technologies whereas others like the electrodes and electrolyte are commercial components. This device is considered as a first approach in micro fuel cell development that allows identifying and measuring the parameters that influence the most on the device performance at a microscale. In this way, the micro fuel cell is tested under different operation conditions such as fuel concentration, working temperature and device orientation. Moreover, the effect of the geometry of the silicon microfabricated parts such as the current collectors on the fuel cell response and efficiency is explored. A transient three-dimensional computational model of the fuel cell is also presented in this section as an effective tool to predict device performance when all the mentioned parameters are modified.

The second section of the current thesis presents different strategies regarding the integration of all micro fuel cell components into a more compact device. These approaches take advantage of the use of different polymer micropatterning techniques as a way to optimize the device dimensions and reduce materials and production cost. The approach presented in Chapter 3 consists on one side, of the addition of an electrode layer to the silicon current collectors by the incorporation of a fine silicon grid containing the catalysts. On the other side, the Nafion® commercial sheet used in the micro fuel cell developed in Section I is substituted by a hybrid polymeric electrolyte membrane composed of a PDMS matrix filled with a proton conducting polymer. The advantage of this approach is based on the capability of PDMS to bond to silicon by plasma oxidation, which would allow the assembly of all components into a highly compact device. A second approach, described in Chapter 4, makes use of SU-8 photoresist to fabricate all of the micro fuel cell components. In this case, the resist structures of the current collectors and the matrix for the MEA were done by standard UV-lithography and then functionalized. Current collectors were metalized to provide electrical conduction; the MEA-matrix was filled with polymer electrolyte and then coated with a catalyst layer. Taking advantage of the SU-8 bonding capabilities, the components were assembled by hot-pressing, achieving a planar all-polymer micro fuel cell. Finally, Chapter 5 describes a polymeric fuel delivery system fabricated with replica moulding techniques that can be incorporated onto a micro fuel cell to facilitate the fluid distribution in a passive way and allow the future stacking of several devices. In this system, fuel distribution is performed by the definition of different hydrophobic and hydrophilic areas. Hydrophobicity was obtained by micropatterning the polymeric surfaces. In this way, the replication of three-dimensional multilevel structures was possible using a fast and scalable fabrication process.

The third section presents two particular applications of the micro fuel cells developed in previous chapters. Chapter 6 presents a microfabricated bio fuel cell using microorganisms as biocatalysts of organic compounds. The effect of the device dimensions reduction was evaluated and compared against a macro scale device. Additionally, the device was used to evaluate its capability to work as a microfabricated biosensor measuring the change in the output signal after the microorganisms are exposed to a toxic material. Chapter 7 shows the combined capability of a micro fuel cell to deliver electrical power and pump a liquid through a microfluidic platform. The driving force responsible of making the sample flow in this device is the pressure produced by the CO₂ gas generated in the fuel cell reaction. These features provided by the fuel cell operation can be of great interest for microfluidic applications such as Lab-on-a-Chip or micro Total Analysis Systems (μTAS).

Finally, general conclusions of this work are presented together with some remarks about the trends that will follow the future work.

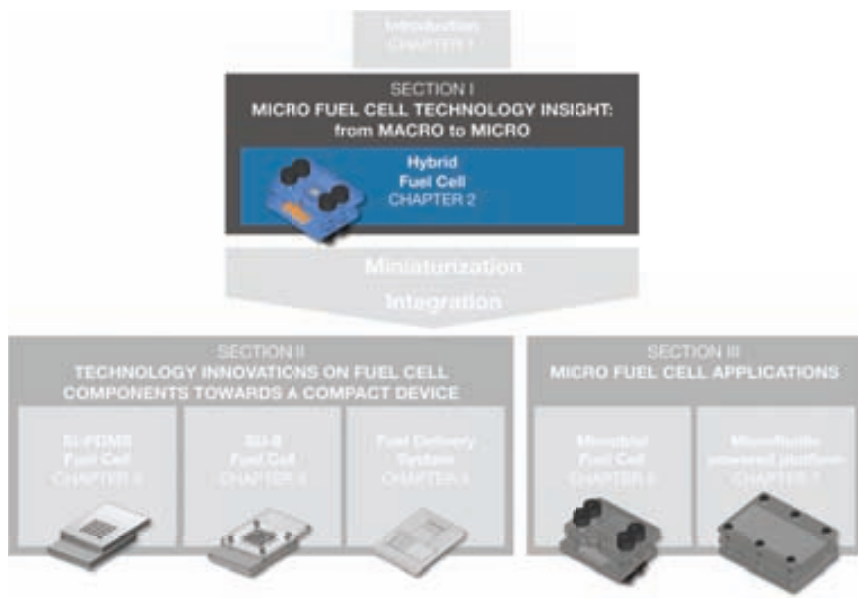
References in Chapter 1.

- [1] Madou M. *Fundamentals of microfabrication: the science of miniaturization* 2002: CRC Press)
- [2] Franssila S. *Introduction to microfabrication* 2004 (West Sussex, England: John Wiley and Sons)
- [3] Eposs STRATEGIC RESEARCH AGENDA of EPoSS *The European Technology Platform on Smart Systems Integration* (2009)
- [4] Meninger S., Mur-Miranda J.O., R Amirtharajah, Chandrakasan A.P. and Lang J.H. A micropower programmable DSP powered using a MEMS-based vibration-to-electric energy converter *Proc. IEEE Int. Conf. Solid State Circuits* (2000) 362 - 3
- [5] Jacobson S.A. and Epstein A.H. An informal survey of power MEMS. In: *The International Symposium on Micro-Mechanical Engineering*, 2003 (Tsuchiura, Japan
- [6] Hart R.W., White H.S., Dunn B. and Rolison D.R. 3-D Microbatteries *Electrochemistry Communications* **5** (2003) 120-3
- [7] Kamarudin S.K., Daud W.R.W., Ho S.L. and Hasran U.A. Overview on the challenges and developments of micro-direct methanol fuel cells (DMFC) *Journal of Power Sources* **163** (2007) 743-54
- [8] Cook-Chennault K.A. and Et Al. Powering MEMS portable devices—a review of non-regenerative and regenerative power supply systems with special emphasis on piezoelectric energy harvesting systems *Smart Materials and Structures* **17** (2008) 043001
- [9] Morse J.D. Micro-fuel cell power sources *International Journal of Energy Research* (2007)
- [10] Larminie J. and Dicks A. *Fuel Cell Systems Explained* 2003 (West Sussex, England: John Wiley & Sons)
- [11] Evans A., Bieberle-Hütter A., Galinski H., Rupp J., Ryll T., Scherrer B., Tölke R. and Gauckler L. Micro-solid oxide fuel cells: status, challenges, and chances *Monatshefte für Chemie / Chemical Monthly* **140** (2009) 975-83
- [12] Chen R. and Zhao T.S. Performance characterization of passive direct methanol fuel cells *Journal of Power Sources* **167** (2007) 455-60
- [13] Nam-Trung N. and Siew Hwa C. Micromachined polymer electrolyte membrane and direct methanol fuel cells—a review *Journal of Micromechanics and Microengineering* **16** (2006) R1
- [14] Kamarudin S.K., Achmad F. and Daud W.R.W. Overview on the application of direct methanol fuel cell (DMFC) for portable electronic devices *International Journal of Hydrogen Energy* **34** (2009) 6902-16
- [15] Kjeang E., Djilali N. and Sinton D. Microfluidic fuel cells: A review *Journal of Power Sources* **186** (2009) 353-69
- [16] Wang Y., Chen K.S., Mishler J., Cho S.C. and Adroher X.C. A review of polymer electrolyte membrane fuel cells: Technology, applications, and needs on fundamental research *Applied Energy* **In Press, Corrected Proof**
- [17] Nguyen N.-T. Micromachined polymer electrolyte membrane and direct methanol fuel cells—a review *Journal of Micromechanics and Microengineering* **16** (2006) R1
- [18] Hahn R., Wagner S., Schmitz A. and Reichl H. Development of a planar micro fuel cell with thin film and micro patterning technologies *Journal of Power Sources* **131** (2004) 73-8
- [19] Yamazaki Y. Application of MEMS technology to micro fuel cells *Electrochimica Acta* **50** (2004) 663-6
- [20] Chan S.H., Nguyen N.T., Xia Z.T. and Wu Z.G. Development of a polymeric micro fuel cell containing laser-micromachined flow channels *Journal of Micromechanics and Microengineering* **15** (2005) 231-6
- [21] Shah K., Shin W.C. and Besser R.S. A PDMS micro proton exchange membrane fuel cell by conventional and non-conventional microfabrication techniques *Sensors and Actuators B: Chemical* **97** (2004) 157-67

- [22] Kuriyama N., Kubota T., Okamura D., Suzuki T. and Sasahara J. Design and fabrication of MEMS-based monolithic fuel cells *Sensors and Actuators A: Physical* **145-146** (2008) 354-62
- [23] Moghaddam S., Pengwang E., Lin K.Y., Masel R.I. and Shannon M.A. Millimeter-Scale Fuel Cell With Onboard Fuel and Passive Control System *Microelectromechanical Systems, Journal of* **17** (2008) 1388-95
- [24] Ito T. and Kunitatsu M. Fabrication of a micro DMFCs array made of photosensitive glass *Electrochemistry Communications* **8** (2006) 91-4
- [25] Motokawa S., Mohamedi M., Momma T., Shoji S. and Osaka T. MEMS-based design and fabrication of a new concept micro direct methanol fuel cell (μ -DMFC) *Electrochemistry Communications* **6** (2004) 562-5
- [26] Yeom J., Mozsgai G.Z., Flachsbarth B.R., Chohan E.R., Asthana A., Shannon M.A. and Kenis P.J.A. Microfabrication and characterization of a silicon-based millimeter scale, PEM fuel cell operating with hydrogen, methanol, or formic acid *Sensors and Actuators B: Chemical* **107** (2005) 882-91
- [27] Lu G.Q., Wang C.Y., Yen T.J. and Zhang X. Development and characterization of a silicon-based micro direct methanol fuel cell *Electrochimica Acta* **49** (2004) 821-8
- [28] Cha H.-Y., Choi H.-G., Nam J.-D., Lee Y., Cho S.M., Lee E.-S., Lee J.-K. and Chung C.-H. Fabrication of all-polymer micro-DMFCs using UV-sensitive photoresist *Electrochimica Acta* **50** (2004) 795-9
- [29] Aravamudhan S., Rahman A.R.A. and Bhansali S. Porous silicon based orientation independent, self-priming micro direct ethanol fuel cell *Sensors and Actuators A: Physical* **123-124** (2005) 497-504
- [30] O'hayre R. *Fuel Cell Fundamentals* 2006 (New York: John Wiley & Sons)
- [31] Shen M. and Scott K. Power loss and its effect on fuel cell performance *Journal of Power Sources* **148** (2005) 24-31
- [32] Liu J.G., Zhao T.S., Liang Z.X. and Chen R. Effect of membrane thickness on the performance and efficiency of passive direct methanol fuel cells *Journal of Power Sources* **153** (2006) 61-7
- [33] Kim Y.-J., Bae B., Scibioh M.A., Cho E. and Ha H.Y. Behavioral pattern of a monopolar passive direct methanol fuel cell stack *Journal of Power Sources* **157** (2006) 253-9
- [34] Kho B.K., Bae B., Scibioh M.A., Lee J. and Ha H.Y. On the consequences of methanol crossover in passive air-breathing direct methanol fuel cells *Journal of Power Sources* **142** (2005) 50-5
- [35] Bae B., Kho B.K., Lim T.-H., Oh I.-H., Hong S.-A. and Ha H.Y. Performance evaluation of passive DMFC single cells *Journal of Power Sources* **158** (2006) 1256-61

SECTION I

MICRO FUEL CELL TECHNOLOGY INSIGHT: from MACRO to MICRO



2. Hybrid Micro Fuel Cell

This chapter presents the initial approach to the development of a silicon microfabricated fuel cell. In this first fuel cell version, the current collectors were fabricated in silicon by microfabrication technologies whereas the membrane electrode assembly (MEA) was the same commercial component used in macro direct methanol fuel cells, for this reason the device was considered hybrid.

The objective of this development was to study the effect of miniaturization of the fuel cell system and obtain its main performance characteristics. Among the different fuel cells types, a direct methanol was chosen for this study because of their already proved advantages as portable power sources, i.e. high-energy density, easy handling and storage of liquid fuel. This kind of fuel cell is capable of working at room temperature, which significantly reduces the thermal management challenges for small systems and increase device simplicity. Moreover, the present approach is based on a passive fuel delivery, using only a diffusion mechanism to supply the fuel to the system. In this way, the need of additional heating systems, pumps and controls in the fuel cell can be eliminated, simplifying the system balance-of-plant (BOP) considerably.

The following chapter is divided in three sections. In the first one, the design, fabrication and assembly of the different components of the micro direct methanol fuel cell is presented. The second section presents a thoughtful characterization of the device under several operating conditions, such as methanol concentration, temperature and orientation. Additionally, the influence of geometrical parameters in the device performance, as well as the fuel cell efficiency is evaluated in this section. Finally, a transient 3D finite element model of the system developed as a tool to predict the device performance under different conditions is presented in the last section.

2.1 DEVICE DESIGN AND ASSEMBLY

The micro direct methanol fuel cell has been conceived as a hybrid device consisting of a commercial and already assembled membrane electrode assembly sandwiched between two microfabricated silicon current collectors. All these parts are joined with a custom-made acrylic casing. The simplicity of this approach allowed a clear understanding of the fundamental operation of a fuel cell, as well as the influence of each of the components in the device performance. Figure 2.1 shows a schematic diagram of the micro fuel cell parts and its assembly. In the following section, the design and composition of each part of the micro fuel cell is described in detail.

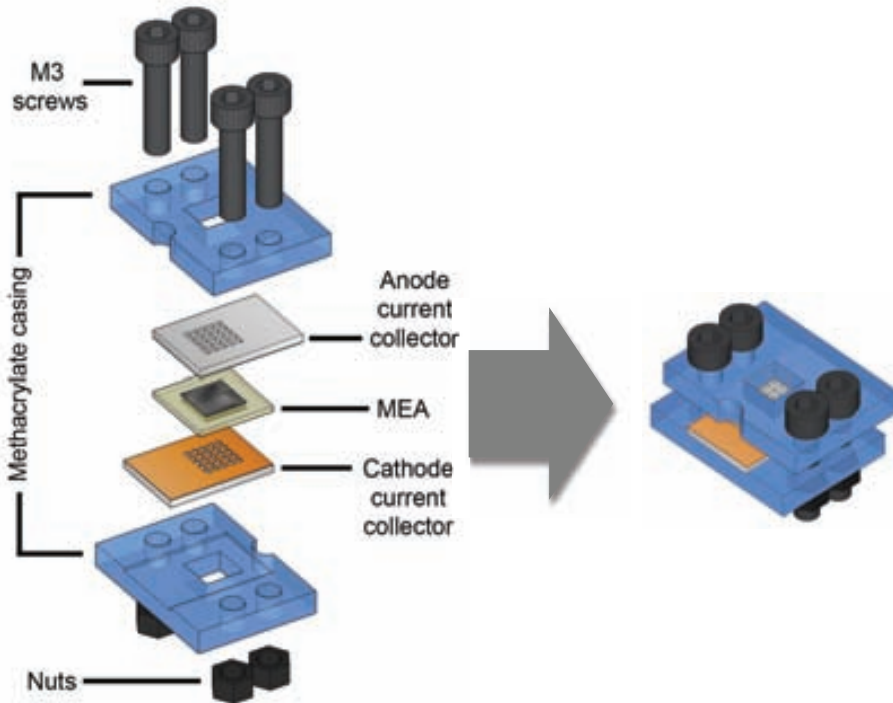


Figure 2.1 Hybrid micro fuel cell parts and assembly.

2.1.1 Membrane Electrode Assembly

A typical membrane electrode assembly of a direct methanol fuel cell consists of a polymer electrolyte membrane, being Nafion[®] by Dupont the most widely used, covered on both sides by thin carbon-based porous electrodes. These electrodes contain the catalyst particles that enhance the chemical reactions taking place both at the anode and at the cathode. A common method for MEA fabrication consists on the preparation of a catalytic ink from a mixture of catalyst powder, ionomer solution and carbon particles. This ink is then applied to the polymeric electrolyte surface by methods such as printing, impregnation, spray or electrospray [1-5]. A conductive diffusion layer, commonly carbon paper or carbon cloth, can also be used to incorporate the catalysts while improving the distribution of reactants throughout the membrane surface [6].

The fabrication and optimization of membrane electrode assemblies was out of the scope for this first approach on micro fuel cell development, so it was decided that the use of a commercial MEA was more convenient. The MEA used in this work

consists of a Nafion® 117 membrane electrolyte with 4.0 mg/cm² Pt-Ru catalyst load for the methanol reaction in the anode side and 4.0 mg/cm² Pt on the cathode (from E-TEK®). This configuration of catalysts has been extensively used for methanol fuel cells due to its high catalytic activity. The ruthenium component in the anode side is included to reduce the platinum poisoning by CO produced at one stage of the methanol oxidation reaction. Nafion® 117 membrane is a typical electrolyte used in DMFC because its high thickness reduces significantly the permeability of methanol, which is one of the main problems of this kind of fuel cells [7]. Figure 2.2 shows on one side, a SEM image of the MEA cross-section where the thickness of the different layers can be seen, and on the other side, a simplified scheme of the components and structure of the electrode.

The electrode in the MEA is mainly composed of small Pt or Pt-Ru catalysts particles covering larger particles of carbon black powder (in this case, carbon black XC-72 from Cabot Corp.). The catalyst is widely spread over the carbon in a way that the surface in contact with the reactants is maximized. The carbon-supported catalyst particles are mixed with a solution of the polymer electrolyte and spread over the electrolyte membrane. As shown in Figure 2.2b, a thin layer of the electrolyte also reaches the catalyst, which promotes the contact between electrolyte, reactant and electrode catalyst. This three-phase contact is usually called *triple-point* and it is important to maximize its number to increase the performance of the MEA [8].

Due to the unavailability of MEAs in the market with the required dimensions for this application, a 30 cm x 30 cm MEA was purchased from Fuel Cell Store [9]. From this component, small squared pieces (1.0 cm²) were cut out. In order to ensure electrical insulation, catalyst layers had to be removed from the borders of the small MEAs, leaving only a 5 mm x 5 mm active area in the middle. Figure 2.3 shows a picture of the as-purchased MEA and one of the small MEAs used for the implementation of the micro fuel cell.

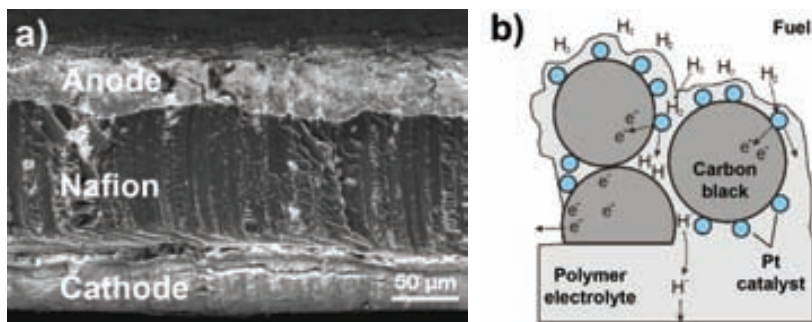


Figure 2.2 (a) SEM image of MEA cross-section. The Nafion® membrane average thickness is around 115 µm while catalysts layers are around 40 µm. (b) Diagram of the composition of the electrode layer in the MEA.

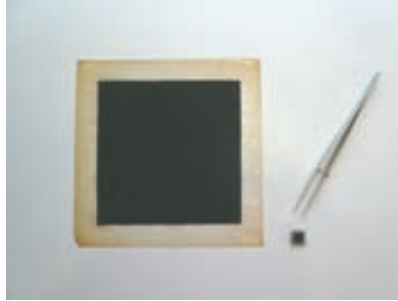


Figure 2.3 Membrane Electrode Assembly purchased (left) and used in the micro fuel cell (right).

2.1.2 Silicon current collectors

Currents collectors are responsible of extracting the electrons generated in the anode and driving them to the cathode through an external circuit. In addition to that, they generally provide the mechanical support to the fuel cell structure and facilitate the mass transport of the reactants. All these issues have been taken into account when designing the silicon microfabricated plates. Therefore, the plates have been provided with an array of vertical squared channels of 300 micrometers long covering an area of 5 mm x 5 mm (yielding a total active area of 0.28 cm²). Channels dimensions have been set to 80 μm x 80 μm in order to ensure the prevalence of the capillary force versus gravity regardless of device orientation [10] and facilitate mass transport in the system, ensuring that the fuel reaches the membrane and CO₂ is correctly degassed. In addition, due to their role as current collectors, they also have to be provided with good electrical conductivity to reduce ohmic losses when driving the electrons.

In order to test the influence of the exposed area of the MEA to the fuel, three different designs were fabricated varying the distance between channels with separations of 20, 40 and 80 μm. The first generation of current collectors were done of 500 μm thick silicon wafers, therefore a 200 μm deep cavity was defined at the silicon wafer backside and aligned with the channel array to be used as a fuel reservoir. Figure 2.4 shows a scheme of the basic silicon-based micro fuel cell structure. A later update of the collectors design was fabricated using silicon wafers with a thickness of 300 μm where the backside etching for the cavity was not needed, simplifying the fabrication process.

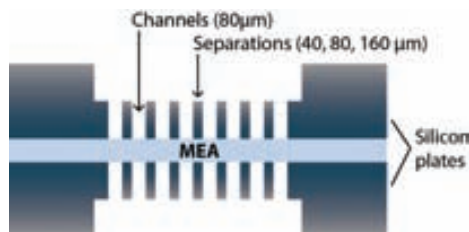


Figure 2.4 Diagram of fuel cell with silicon plates showing the fuel reservoir, the array of 80 μm channels and separations between channels.

The main steps of the microfabrication process of the silicon current collectors have been summarized in Table 2.1. The process for the first generation of silicon current collectors starts with 100 mm double-side polished Si wafers 500 μm thick. A first photolithography is done on the front side to define an array of squared windows with 80 μm size distributed over a squared surface of 5 mm x 5 mm. Subsequently, a second photolithography is performed on the back side to define the cavity for the fuel container. Then, a Deep Reactive Ion Etching (DRIE) is realized first on the front side to obtain 300 μm -deep channels, and secondly at the back until the wafer is completely perforated. In the updated version of current collectors, only the first etching is needed to perforate the 300 μm wafer completely. Figure 2.5 shows a SEM image of the channels array, indicating the dimensions of the channel and the separations between channels. In order to provide the current collectors with an appropriate electrical conductivity, a 150 nm Ti/Ni sputter layer is deposited covering the front side of the wafer and the channels walls. This last conductive layer is used as a seed layer for the 2 μm thick Ni layer that is electrodeposited afterwards. The Ni layer that significantly reduces the resistivity of the current collector is then covered by a thin Au layer to prevent oxidation. Finally, the wafer is cut into 10 mm x 14 mm chips as shown in Figure 2.6.

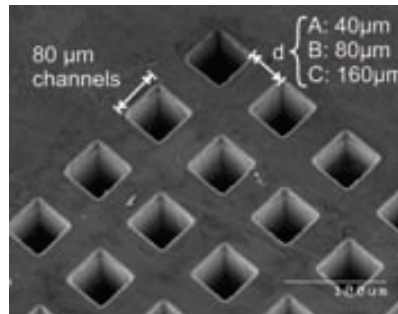


Figure 2.5 SEM image of the front side of the silicon wafer showing the array of 80 μm channels and the different separations between channels.

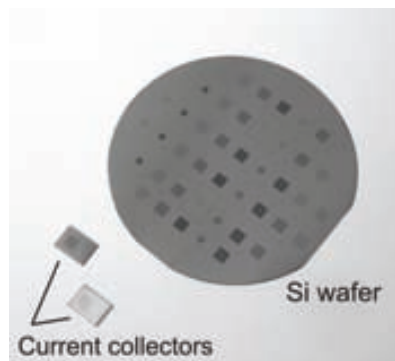









Figure 2.6 A complete microfabricated silicon wafer and a pair of current collectors.

Table 2.1. Simplified microfabrication process of the silicon plates.

Step	Description
	Double side polished wafer
	Photolithography front side
	Photolithography back side
	DRIE front side
	DRIE back side
	Sputter deposition Ti/Ni
	Electrodeposition Ni/Au

2.1.3 Device packaging and assembly

One of the main issues in micro fuel cell development is the device packaging. While successful advances in the improvement of each of the fuel cell components (membranes, catalysts, current collectors, etc.) have been achieved during the last years, their integration in a compact and simple package is still an important challenge. In order to ensure an efficient performance of a fuel cell, sufficient pressure between the MEA and current collectors has to be applied to minimize ohmic resistance between the different fuel cell components and avoid fuel leaks. This becomes particularly challenging due to the changes in volume of the polymeric electrolyte depending on its water content. For this reason the implementation of an external casing using elements such as plates or adhesives is needed, increasing the size and complexity of the devices.

For the micro fuel cell presented in this work, two methacrylate pieces were fabricated to be positioned onto the plates and tight all the components together with four bolts. In this way, the pieces give mechanical support to the device and provide a larger fuel reservoir while testing.

The pieces with external dimensions of 16 mm x 25 mm were milled from a 5 mm thick methacrylate plaque using a BASIC 540-16 CNC milling machine (STEP-FOUR GmbH). Each of the pieces was provided with a 300 μ m-depth pocketing with the size of the silicon chip on one side. A squared window of 5.2 mm x 5.2 mm was

milled through the plaque. Once the silicon chip correctly aligned, this cavity allowed to define a fuel reservoir of 125 microliters approximately. Four holes were drilled at the external sides to allocate the M3 screws that allow assembling all the fuel cell parts together. A rounded rabbet on one edge was finally defined to fit the cable jacks for the electrical connection to the fuel cell current collectors. Figure 2.7 depicts a photograph of the fabricated methacrylate casing.



Figure 2.7 Milled methacrylate pieces for micro fuel cell packaging.

The device is finally assembled by fitting the cathode silicon current collector into one of the pocketings milled in the methacrylate piece. Then the MEA is placed on the silicon chip and its cathode active area is aligned over the chip area with the microchannels array. The anode current collector previously fitted in its corresponding methacrylate casing is then placed against the anode side of the MEA. Finally, the screws are inserted through the holes of the methacrylate pieces and tightened with the nuts on the other side. In this way, the anode fuel reservoir of the fuel cell is faced upwards for fuel feeding. Figure 2.8 shows a picture of the micro fuel cell assembly being filled with the methanol solution.

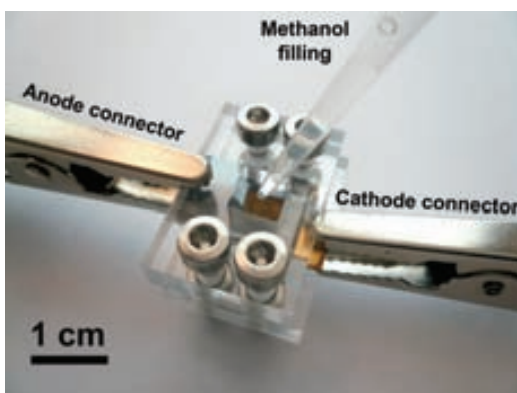


Figure 2.8 The anode reservoir of the micro fuel cell is filled with 100 μl of methanol while cathode side is left open to the air.

2.2 MICRO FUEL CELL CHARACTERIZATION

The micro fuel cell was extensively characterized by measuring its performance under different operating conditions and current collectors geometries. This part of the characterization was performed by measuring the evolution of the fuel cell open circuit voltage and its polarization curves at the different conditions. Moreover, the fuel cell efficiency was calculated from long-term operation measurements, in which the device was subjected to constant current or voltage conditions. The obtained measurements and discussion of the results are presented in the following sections.

2.2.1 Measurement Setup

I-V polarization curves of the microdevices were obtained using a Keithley 2400 Sourcemeter and a Keithley 2700 Multimeter / Data Acquisition System interfacing with a computer with an in-house program built on LabVIEW. The program allows the control and recording of voltage and current in the fuel cell, as well as a monitoring of the anode and cathode temperatures. Figure 2.9 shows the LabVIEW virtual instrument interface of the program.

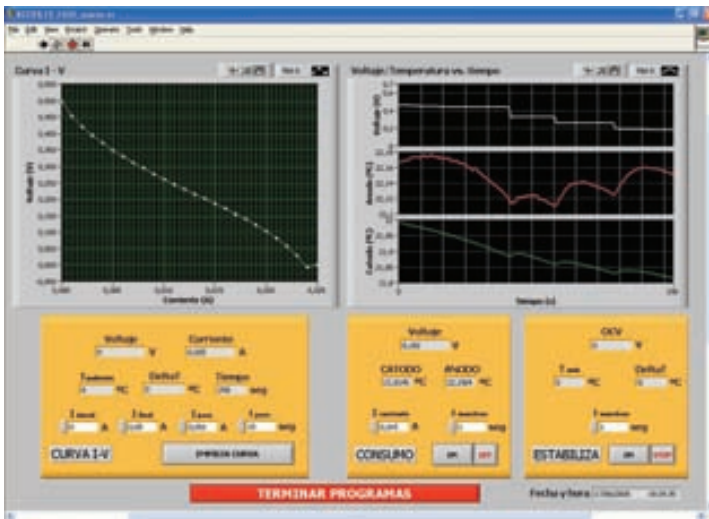


Figure 2.9 LabVIEW VI interface of the program used for characterization.

Before the characterization of the device a pre-treatment process had to be done to the MEAs to activate the electrolyte membrane. The process consisted on wetting the anode side with a concentration of 0.25M methanol for several hours and afterwards submitting the fuel cell to working conditions at a constant current for a short period of time [30].

In order to obtain the characterization measurements, the micro fuel cell was placed inside a small chamber equipped with a holder to keep it still and thermally isolated. The chamber was provided with the electrical connections to contact the anode and

cathode current collectors and also with small thermistors that are inserted on both sides of the fuel cell to monitor its temperature. Each of the measurements was performed after filling the anode fuel reservoir with a methanol volume of 100 μl using a micropipette.

2.2.2 Influence of operating conditions on fuel cell performance

The influence of different parameters that modulate fuel cell activation losses such as methanol concentration and temperature has been studied. Moreover, the device has been submitted to changes in device orientation in order to validate its performance in portable applications. In this section the results obtained from these measurements are presented and discussed.

2.2.2.1 Methanol concentration

Open circuit voltage evolution

In a direct methanol fuel cell, open circuit voltage (OCV) is strongly dependent on the methanol concentration due to the effect of methanol crossover. In order to evaluate the influence of methanol concentration on the open circuit voltage of cell at room temperature in the device, the evolution of the OCV when filling the fuel reservoir with 100 μl of methanol at different concentrations has been measured and depicted in Figure 2.10. This figure shows the changes in the OCV with time from the moment of fuel injection of a particular methanol solution into the fuel reservoir until it reaches a steady value. As expected, increasing methanol concentrations lead to lower OCV values. As seen in the figure, when the reservoir is filled, the OCV experiences an abrupt jump when the methanol reaches the anode and then drops slowly to a steady value, as part of the fuel permeates the membrane and reaches the cathode. In order to compensate the decrease in methanol concentration associated to fuel losses originated by the methanol crossover, the fuel reservoir was refilled after a few minutes. It can be observed that the initial voltage jump becomes smaller when refilling the reservoir a second time. This is due to the accumulation of both methanol and water in the cathode, which limit access of oxygen to the catalytic sites and leads to a decrease in the methanol oxidation rate both in the anode and cathode sides [11, 12]. This effect was also visible when the reservoir was refilled with higher concentrations of methanol.

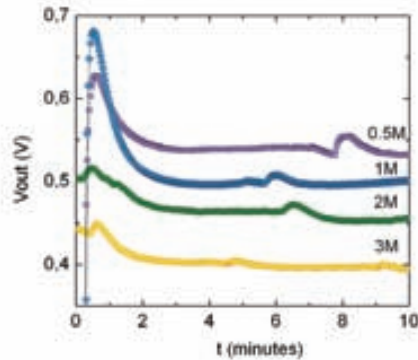


Figure 2.10 Open circuit voltage evolution at different methanol concentrations.

Operation performance

The current collector design with 80- μm separation between channels was chosen to evaluate the behavior of the micro fuel cell working at different methanol concentrations. The system was tested at concentrations of 0.5M, 1M, 2M, 3M, 4M and 5M. The measured I-V curves have been depicted in Figure 2.11a. Measurements were taken after the OCV stabilization sequence shown in previous section. As already discussed, a reduction in OCV due to the effect of methanol crossover through the membrane was observed.

It has to be noted that generally, the methanol concentration to obtain the maximum power in a passive cell is much higher than in an active cell, which has an appropriate concentration of around 1M [13]. This is due to the need of compensating the slower mass transport rate of methanol, which in passive cells is performed by diffusion. However, increasing concentration leads to higher methanol crossover and consequent deterioration of cell performance. In practice, a compromise between transport benefits and crossover negative effects is found at concentrations between 4M and 5M [14]. Figures 2.11a and 2.11b show that the maximum power density delivered by the device increases with the concentration and reaches a maximum power density of 11.5 mW/cm^2 at 5M. This power density is higher than any of the values reported before in silicon-based methanol fuel cells without external fuel pumping [14] and close to the values reported for stainless-steel fabricated passive micro cells working at methanol concentrations of 1M and 2M [15, 16]. Nevertheless, the increment in power density obtained when filling the fuel cell with higher methanol concentrations is smaller than the one observed in passive macro devices, in which increases between 15-50% of maximum power density have been reported when comparing performance at low and high concentrations [16-18].

The reason of obtaining a better performance at higher concentrations has been attributed in the past to the compensation of the mass transport limitations arising in a diffusion-driven methanol distribution in this kind of cells. In fact, this effect can be observed in the differences shown in the limiting current behaviour by the curves corresponding to 0.5M, 1M and 2M methanol concentrations. However, the fuel cell characteristic curves for 3M, 4M and 5M show a very similar behaviour. In this case, the explanation can be found in the observations performed recently by Liu et al., who discovered that the better performance of a passive fuel cell at high methanol concentrations could be mainly attributed to a cell temperature increase caused by the exothermic reaction of the crossed-over fuel [19]. To evaluate the role of temperature in the device performance, its effect on the micro fuel cell is explored in the next section.

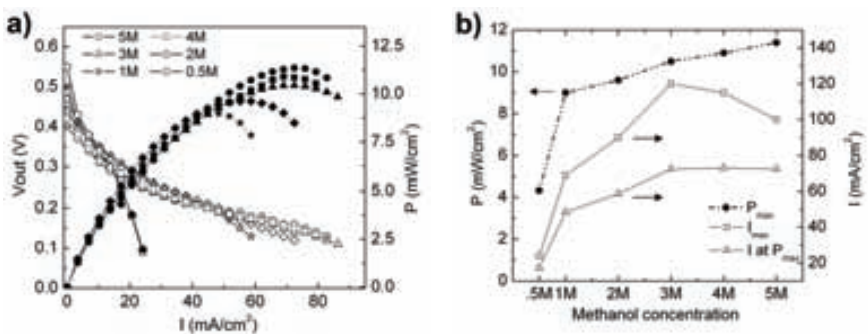


Figure 2.11 (a) Performance of device working at different methanol concentrations. (b) Values of maximum power density, maximum current density and current density at maximum power of the fuel cell depending on methanol concentrations.

2.2.2.2 Temperature

In order to test the relation between temperature and methanol concentration and their influence on the fuel cell performance the temperature of the device was evaluated using a tiny thermistor placed in the anode current collector reservoir. Figure 2.12 shows both the OCV and temperature evolution when filling the micro fuel cell reservoir with 2.0 M and 4.0 M concentrations. As presented previously, it can be seen that at the moment of fuel injection, the OCV experience an abrupt jump from 0 to 0.6 V and then drops to a stable value that, as it has been shown before, depends on the methanol concentration. As expected, temperature of the micro fuel cell shows a higher increase at 4.0 M concentration due to the larger heat production from methanol oxidation at the cathode. However, the micro fuel cell did not heat up above 1°C in any case, which is a variation far below to the 10-15°C reported by other authors [11, 16, 20].

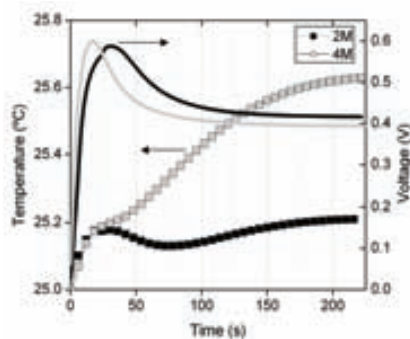


Figure 2.12 Evolution of the open circuit voltage and temperature of the cell when filling the fuel reservoir with two different methanol concentrations.

The temperature change of the cell at different electric loads was measured for 2M and 4M concentrations and depicted in Figure 2.13. As it has been shown before, the cell temperature at open circuit conditions depends on the methanol concentration. Moreover, the evolution of fuel cell temperature at increasing current densities was also concentration dependent: with a methanol concentration of 2M, the fuel cell temperature rises as it happens with active cells. This is due to the heat produced by the oxygen reduction reaction at the cathode [20]. However, at a concentration of 4M, the temperature keeps constant around a value of 25.6 °C. This is probably due to a temperature compensation effect. As before, the increase of current production in the device leads to an increase of heat produced by oxygen reduction reaction. However, as methanol starts to be consumed at the anode, the methanol flux to the cathode diminishes and so it does the heat production associated to the methanol crossover reaction. This decrease of the heat associated to the crossed-over methanol is significant due to the fact that at 4M concentration the crossover effect is higher than at 2M. Despite the different temperature behaviour at the tested methanol concentrations, temperature difference between both cases did not exceed 0.5 °C. This explains the low influence of the methanol concentration on the maximum power density provided by the silicon-based device. The cause for such a

small temperature increase can be found in the combined effect of the high thermal conductivity of the silicon current collectors [21, 22] and the absence of a Gas Diffusion Layer in the MEA of the device, which could have increased significantly the fuel cell heat losses.

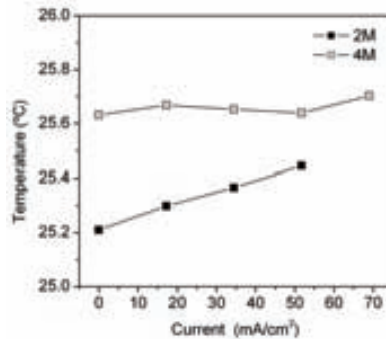


Figure 2.13 Fuel cell temperature at different operation points and methanol concentrations.

Finally, the effect of temperature on the performance of the silicon micro fuel cell was tested by heating externally the device up to a constant temperature of 40 °C. Results are shown in Figure 2.14. It can be seen that the maximum power density achieved at 40 °C is significantly higher than at room temperature, reaching a value of 20 mW/cm². It has to be noted that while the maximum power densities between 2M and 4M concentrations obtained at room temperature showed the slight difference reported in previous sections, when the fuel cell is heated to 40 °C the maximum power densities obtained at the two concentrations are practically the same. These results show that temperature plays a major role in passive fuel cell performance whereas methanol concentration has a mild impact in the achieved maximum power density for concentrations over 2M and concentrates mainly its effects in the concentration losses region that yields beyond the maximum power peak.

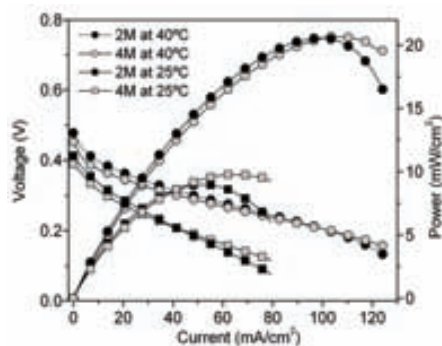


Figure 2.14 Performance at 25°C and at 40°C for 2M and 4M MeOH concentrations.

2.2.2.3 Device orientation

The dimensions of the channels etched in the silicon current collectors were designed small enough to create a capillary force that overcomes gravity. Because of the hydrophilic metal layer covering the channel surface, the capillary force maintains the liquid inside the cavities. In this way, the methanol in the anode reservoir keeps in contact with the membrane regardless of the fuel cell position. This would provide the fuel cell with the capability of keeping its operation regardless of its orientation.

The capability of the device to work under random orientation conditions was tested. The system was characterized with a methanol concentration of 3M in three different orientations, with the methanol reservoir facing up, facing down and placed sideways. The resulting polarization curves are depicted in Figure 2.15. It can be observed that all of the curves start at the same OCV but present different mass transport limitations. The maximum current density was recorded for the fuel cell working upwards. In this case, capillary force and gravity work in the same direction. The worst case was recorded when the cell was placed on its side, with a 20 mA/cm² decrease of the maximal current density, which means a 15% change at the highest intensity point. However, the variation in the maximum power density measured at the different orientations supposed only a 13% decrease in the performance for the case when the cell is placed sideways.

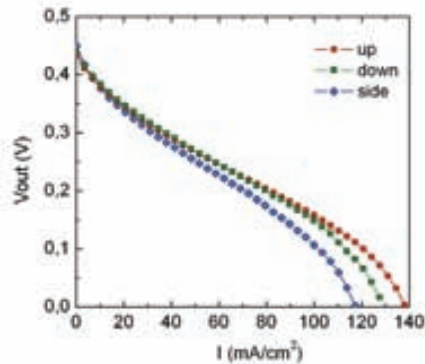


Figure 2.15 Performance at different cell orientations. Fuel cell operating with methanol reservoir facing up, facing down and sideways.

2.2.3 Influence of current collectors geometry on fuel cell performance

Although most of the parameters regulating the performance of passive methanol micro fuel cells are common with active devices, the fact that passively-fed cells rely on diffusion as fuel transport mechanism lead to the necessity of using higher methanol concentrations to enhance fuel distribution [23, 24]. In this sense, the microfluidic structures implemented in the fuel cell current collectors have to be designed carefully as they must ensure an effective methanol distribution and at the same time, avoid the accumulation of both carbon dioxide and water in the electrodes. Whereas the influence of the fluidic structures geometry on active micro fuel cells performance - either in single-cell or fuel cell stacks - has been widely explored in the past, only a few works about this subject have been published in passive micro fuel cells literature [25, 26]. Particularly, it has been shown that in this type of devices, the most influent parameter is the current collector open ratio (i.e. the electrode area exposed to the fuel). Up to now, the effect of the open ratio on fuel cell performance has been explored through experimental studies [27-29], as well as through analytic and computer-based models [30-36]. However, these studies report on current collectors with geometrical features in the millimeter range, whereas there is a lack of experimental results concerning passive fuel cells in micro-scaled technologies.

In particular, this section explores the influence of the current collector geometries on the operation of the micro fuel cell by measuring the performance using current collectors with the same and different open ratio on anode and cathode. Characterization of the devices is performed by obtaining their polarization curves and these results are compared in terms of power density and repeatability.

For these measurements the three different designs of current collectors fabricated are named A, B and C corresponding to the current collector with distance between channels d of 40 μm , 80 μm and 160 μm , respectively. Since the arrays of channels are all delimited in the same chip area, this distance determines the number of channels in the chip, hence the open ratio of the plates. In this way, open ratio is set to 40% for the current collectors with distance A, to 23% for distance B and to 10% for distance C. These geometric features are summarized in Table 2.2. A set of optical microscope images of the microfabricated current collectors of different channel density is shown in Figure 2.16.

Table 2.2. Summary of the microfabricated current collectors.

Design	d	Open ratio
A	40 μm	40%
B	80 μm	23%
C	160 μm	10%

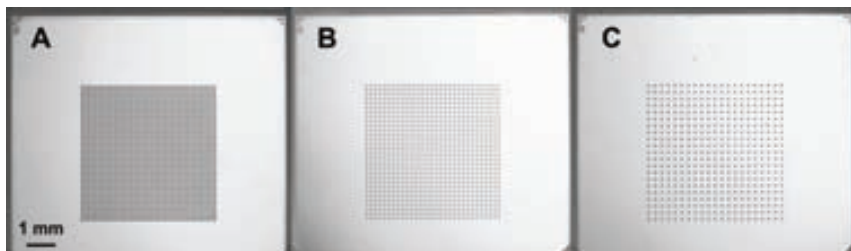


Figure 2.16 Detail of the three silicon current collectors with different open ratio.

The device mounted with the same current collector with an intermediate open ratio (type B) in anode and cathode was set as reference configuration. The influence of the variation of the area exposed to reactants was tested by comparing the performance obtained when using one of this B-type collectors with another using a current collector with larger (type A) or smaller (type C) open ratio. As it has been summarized in Table 2.3, these tests were performed subsequently for the anode and the cathode sides (allowing in this way the discrimination between the cases when the performance of the device is being limited by the supply of methanol – anode - or oxygen –cathode-). The effect of the open ratio unbalance was measured in greater extend by measuring the performance of fuel cells mounted with an extreme combination of A and C current collector types.

Table 2.3 Fuel cell configurations measured.

Fuel cell label	Current collector design	
	ANODE	CATHODE
fc – BB (reference)	B	B
fc - AB	A	B
fc - CB	C	B
fc - BA	B	A
fc - BC	B	C
fc - AC	A	C
fc - CA	C	A

The experimental results are reported in the following two sections. In the first one, the polarization curves obtained from the different fuel cells configurations are presented and discussed in terms of the obtained power densities. In the second one, the same configurations are subjected to consecutive characterizations to evaluate the repeatability of the measurements.

2.2.3.1 Influence of current collector geometry on power density

This section reports on the influence of the current collector open ratio on the power density delivered by a ready-mounted micro fuel cell. The performances of the measured configurations are compared to the reference device fc-BB.

Influence of the anode open ratio

The effect of anode open ratio on the fuel cell power density was evaluated by testing fc-AB, fc-BB and fc-CB fuel cell configurations at methanol concentrations of 2M and 4M. Figure 2.17a shows that at 2M concentration, the obtained maximum power density of the fuel cell is enhanced at larger anode open ratios (values of 8.5 mW/cm², 9.0 mW/cm² and 11.7 mW/cm² were subsequently achieved when increasing the anode open ratio from to 10%, 23% and 40%). The reason for this increase can be simply attributed to the enhancement of the mass transport mechanisms associated to a larger area of electrode exposed to methanol, as evidenced by the progressive extension of the limiting current region of the polarization curves.

However, a different trend was obtained when testing the same fuel cell configurations at a 4M methanol concentration. Figure 2.17b shows that in this case, although higher power densities than at 2M concentration were obtained in some cases, fuel cell performance got worse at increasing anode open ratios (values of 10.2 mW/cm², 10.0 mW/cm² and 8.0 mW/cm² were subsequently obtained when setting the anode open ratio to 10%, 23% and 40% respectively). The reason for this behavior can be explained by taking into account the methanol crossover phenomena through the membrane [11]. At a concentration of 4M, the amount of methanol crossing the membrane to the cathode is significantly higher than at 2M – which is evidenced by a decrease of open circuit voltages (OCV) recorded at 4M – and becomes severe when the anode open ratio is elevated to 40%. The abrupt voltage drop at current densities of 40 mA/cm² observed for the fc-AB configuration is probably due to the blocking of cathode reaction sites by the crossovered methanol.

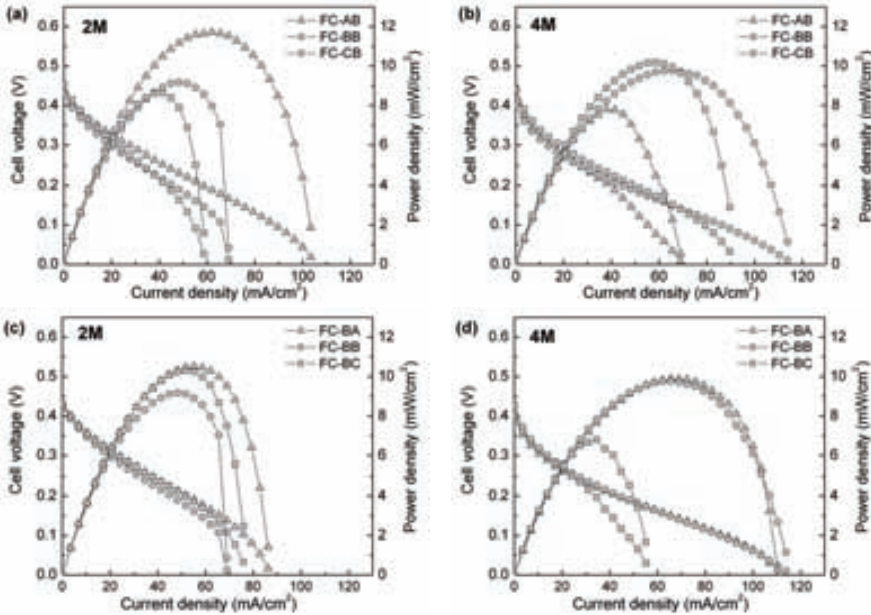


Figure 2.17 Performance of micro FC when testing different silicon current collectors at the anode (a,b) and cathode (c,d) working with methanol concentrations of 2M (a,c) and 4M (b,d).

Influence of the cathode open ratio

The effect of the cathode open ratio was explored by testing fc-BA, fc-BB and fc-BC fuel cell configurations. Figures 2.17c and 2.17d show the polarization curves obtained at methanol concentrations of 2M and 4M respectively. Measurements show that at a methanol concentration of 2M, the maximum power output of the cell was placed at around 10 mW/cm² and did not show any significant variation when the cathode open ratio was subsequently decreased down to 10%. These results proved that the reduction of the cathode open ratio did not cause any limitation in the oxygen transport required in the operation of the cell. A similar trend in the obtained power densities was observed at 4M methanol concentrations for configurations fc-BB and fc-CB (i.e. cathode open ratio \geq anode open ratio). However, unlike what had been observed at 2M concentration, when decreasing the cathode open ratio to 10% while maintaining the anode at 23% (configuration fc-BC) a clear deterioration of cell performance was observed. This decrease can be attributed to the combined effects of reduced oxygen supply and a severe methanol crossover similar to the one observed in the previous section for configuration fc-AB.

Effect of high open ratio unbalance on fuel cell performance

In order to explore further effects of electrode open ratio asymmetry on the micro fuel cell performance, devices with both anode and cathode current collectors set to 10% and 40% (configurations fc-AC and fc-CA) were tested at 2M and 4M methanol concentrations. The obtained performance at 2M methanol concentration is depicted in Figure 2.18a. It can be seen that the maximum power density achieved with fc-AC is comparable to the reference fuel cell fc-BB (around 9 mW/cm^2). In this case, the hypothetical advantages of having a higher open ratio in the anode are compensated by the oxygen transport limitations taking place in the low cathode open ratio. On the other hand, fuel cell configuration fc-CA presents an overall lower performance due to the reduction of methanol contribution (7.2 mW/cm^2). The obtained power density is similar to the one obtained with fc-CB (Figure 2.17a) and lower than fc-BA (Figure 2.17c), confirming that when working at this concentration, the highest the open ratio in the anode current collector, the highest the obtained power density.

Finally, Figure 2.18b shows the results obtained at 4M methanol concentration. It can be seen that for fuel cell configuration fc-AC the maximum power density value falls to 6 mW/cm^2 . As observed before, the reduction in fuel cell performance can be attributed to the blocking of cathode sites caused by the crossoverd methanol. On the contrary, the configuration fc-CA shows an improvement (8.3 mW/cm^2) with regard to 2M concentration performance. The low open ratio in the anode limits the methanol crossover whereas the high open ratio in the cathode side keeps it well ventilated.

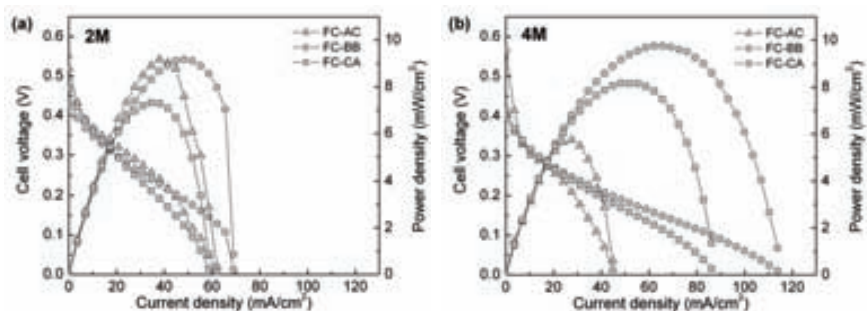


Figure 2.18 Polarization curves for micro fuel cell configurations fc-AC and fc-CA, where very distinct current collectors are tested in anode and cathode sides, working at methanol concentrations (a) 2M and (b) 4M.

2.2.3.2 Influence of current collector geometry on measurement repeatability

In addition to the impact on the output power density, some configurations of current collectors showed a clear effect on the repeatability of the measures. This was observed by performing a set of consecutive polarization curves to the previous fuel

cell configurations at 2M and 4M methanol concentrations. After each of these measurements the concentration of methanol in the anode reservoir of the fuel cell was renewed. Results are presented by depicting pairs of I-V curves corresponding to polarization curves taken at the beginning of the experiment (labeled as 1st) and after having measured a set of polarization curves (between 10-15) with the same device (labeled as 2nd).

Figures 2.19a and 2.19b show the effect in repeatability when varying the open ratio of the anode at 2M and 4M methanol concentrations. These figures indicate that for both methanol concentrations, the polarization curves are repetitive when the open ratio in the anode is lower than in the cathode whereas for equal ratios at both sides (fc-BB), repeatability is only achieved at the lower methanol concentration. On the contrary, when the channel density in the cathode was lower than in the anode, fuel cell performance deteriorated considerably after some measurements.

The same trend can be observed in Figures 2.19c and 2.19d, which show the I-V curves obtained for different cathode open ratios i.e. repeatability is only achieved when the current collector in the anode has a smaller open ratio than the cathode. The deterioration observed on the polarization curves was attributed to the flooding of the cathode electrode [20, 37-41]. When the cathode has a smaller open ratio than the anode, the amount of water generated during the subsequent polarization curves cannot be drained out efficiently, thus resulting in a partial cathode blockage.

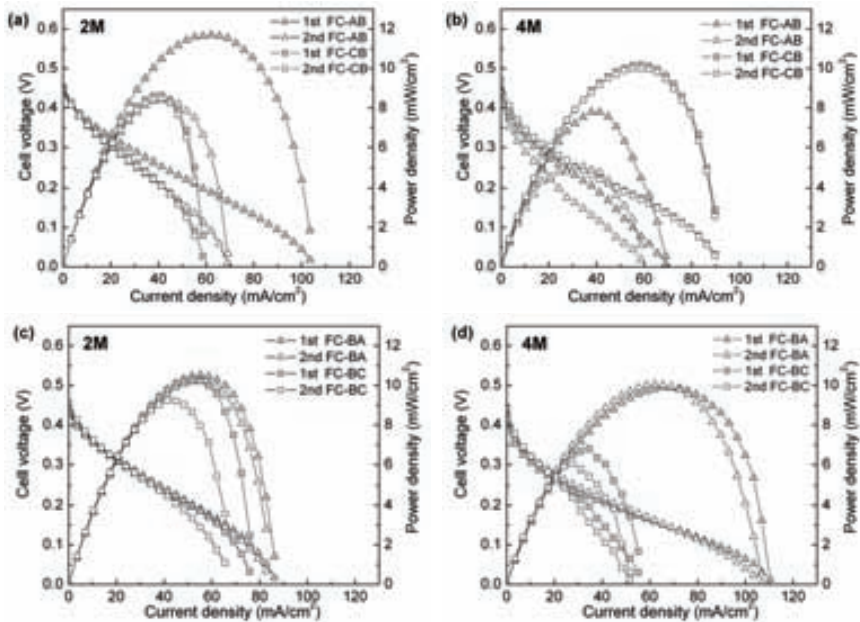


Figure 2.19 Consecutive measurements of micro fuel cell with different current collector design in the anode (a,b) and in the cathode (c,d) working at methanol concentrations of 2M (a,c) and 4M (b,d).

These trends were confirmed again when measuring devices with a high open ratio unbalance (configuration fc-AC and fc-CA). Figures 2.20a and 2.20b show the polarization curves of these fuel cells working at the two tested methanol concentrations. The results from the figures make evident that when the anode open ratio is lower than the cathode (fc-CA), the measurements are quite repetitive for both tested concentrations. On the contrary, when fuel cells are operated with high open ratio on anode current collector and restricted oxygen supply (fc-AC), the performance degraded rapidly (sometimes even after the first measurement). As pointed out before, this behavior could be explained by considering the cathode flooding due to an inefficient water removal. In order to corroborate this, a picture of the cathode side of the MEA was taken just after the measurement of the last polarization curve in one of the configuration showing performance degradation. Figure 2.21 shows that indeed, a water film had partially covered the electrode.

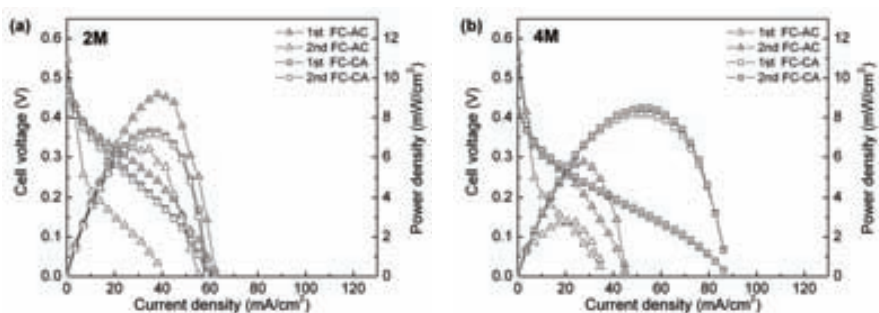


Figure 2.20 Consecutive polarization curves for micro fuel cell configurations fc-AC and fc-CA, working at methanol concentrations (a) 2M and (b) 4M.

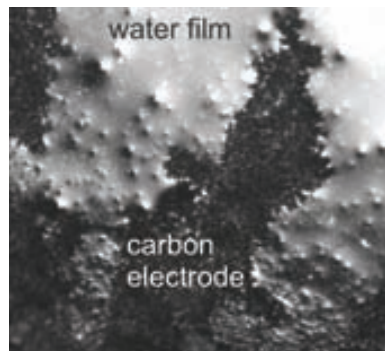


Figure 2.21 Picture of a flooded cathode after performing a set of polarization curves.

The results obtained in the present study have been summarized graphically in Figure 2.22. As it can be seen, the experiments allow to obtain a current collector design chart to be taken into account when determining the most adequate combination for achieving both high power density and stable operation. In the figure, power densities are shown in a gray-scale (darker tones representing higher power values) whereas non-repeatability is outlined with a white grid.

Results show that for some configurations of passive fuel cells, a dissimilar open ratio of the current collectors can yield better performance than a symmetric fuel cell arrangement. It has to be pointed out though, that the best choice regarding power density is strongly related to the methanol concentration of the fuel. That is, when the fuel cells are operated at 2M methanol concentration, the maximum achieved power density increases with the anode open ratio, whereas no significant influence is observed when the cathode open ratio is varied. However, when the fuel cell is supplied with 4M concentration, the anode open ratio must be reduced with regard to the cathode in order to keep a moderate methanol crossover.

Another important result of this study concerns repeatability. It has been observed that some promising configurations turn to show unstable performance. As a general rule, it has been found out that if stability of the fuel cell is to be ensured, current collector open ratio in the cathode must be larger than in the anode so generated water can be effectively evaporated.

Finally, taking into account these guidelines, fuel cell fc-BA (consisting of an anode current collector with 20% open ratio and 40% in the cathode) would be selected as the optimal design, showing good stability and a maximum power density of around 10 mW/cm² at the both tested methanol concentrations.

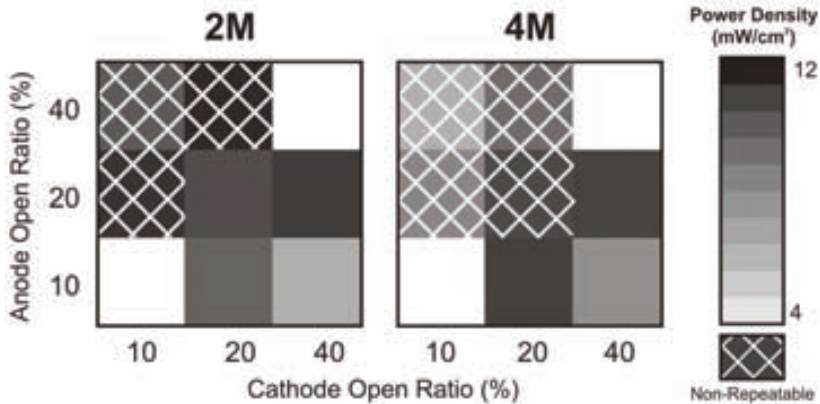


Figure 2.22 Maximum power densities and repeatability of the different micro fuel cell tested configurations.

2.2.4 Fuel cell efficiency

The long-term performance of an active fuel cell is usually characterized by a stable current/voltage output versus time curve depending only on the operation point. However, for passive devices, the current/voltage values vary with time because methanol concentration in the fuel reservoir keeps decreasing during the discharging process.

Methanol consumption and fuel cell efficiency under continuous operation have been evaluated by two methods. First the device is subjected to a constant current value and voltage is monitored until it drops down to zero. Usually, this means that the fuel concentration has decreased in a way that the current demanded in the cell cannot be generated any longer. In the second method the device is operated at a constant voltage and the generated current is monitored until it goes down to zero. In this case, the obtained curves are known as the discharging curves of the micro fuel cell because the fuel cell current decreases steadily until the complete depletion of methanol in the reservoir.

Generally, the performance of the fuel cell at long-term runs depends significantly on the operation point. The operating range is placed within the ohmic region on the I-V curve, as it is the region where the fuel cell is able to provide the highest power values without suffering from mass transport limitations. Due to that, the microDMFC has been tested at different voltage/current values. The device was mounted with the intermediate-open ratio current collector design with 80 μ m separation between channels and the fuel reservoir was filled with fresh 100 μ l of fuel at the beginning of every measurement.

A quantitative evaluation of the efficiency of fuel cell can be assessed by taking into account the Faradic and energy efficiency concepts [42]. The Faradic efficiency allows to evaluate the percentage of the theoretical fuel capacity that is actually being converted to current and it is computed by the following expression:

$$\eta = \frac{\int_0^t i(t) dt}{6C_{MeOH} V F} \quad (2.1)$$

being t the operating time, $i(t)$ the measured current, C_{MeOH} the methanol concentration, V the solution volume and F the Faraday constant. Moreover, the energy efficiency of the fuel cell can be evaluated by comparing the power delivered by the cell when it is discharged to the energy that the fuel cell could deliver ideally, that is, when working at its theoretical voltage:

$$\xi = \frac{\int_0^t i(t) \cdot v(t) dt}{6C_{MeOH} V F E_T} \quad (2.2)$$

where $v(t)$ is the operating voltage and E_T is the reversible cell voltage at a temperature T .

2.2.4.1 Fuel cell operated at constant current

The evolution in time of the micro fuel cell voltage was measured at two different and constant density current values. The experiment was performed for methanol concentrations of 2M and 3M. The current density values at which the fuel cell was operated were chosen from the polarization curves shown in Figure 2.23.

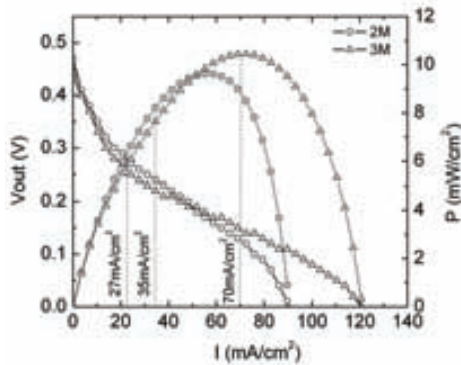


Figure 2.23 Constant current density values chosen for the long-term operation tests.

The first set of current values was chosen so the fuel cell would operate for the two methanol concentrations at a power density of around 9 mW/cm^2 . In this way, the fuel cell was set to provide a current value of 35 mA/cm^2 for methanol at 2M and 27 mA/cm^2 when filled with methanol concentration of 3M. Figure 2.24a shows the obtained transient power density curves. A stable cell performance was observed in both cases until a sudden drop in the output cell power occurred. This is due to a significant decrease of methanol concentration in the reservoir. As expected, the increase of methanol concentration from 2M to 3M extends operation time of the fuel cell from 30 to 50 minutes.

After that, the fuel cell reservoir was filled again with methanol at 3M and operated close to its maximum power density, which corresponded to a current density of 70 mA/cm^2 . Figure 2.24b shows the power density evolution obtained at this new current demand compared with the fuel cell working at 27 mA/cm^2 . As it has been observed, at the first point the fuel cell delivered a stable output power for more than 50 minutes. On the contrary, when the cell was operated at the second current value -corresponding to the maximum power on the P-I curve of the cell- the output power was stable only for a period of about 5 minutes. This is due to the fact that the current delivered by the fuel cell was so high that after a short while, it was difficult to maintain a fuel concentration of 3M at the anode because the overall methanol concentration in the fuel reservoir had started to decrease.

In this case, the operating point migrates towards the I-V curve region regulated by mass transport limitations and immediately the output voltage and therefore the fuel cell power drops down to zero.

The Faradic and Energy efficiencies were computed by integrating the area after the curves in Figure 2.24b. Results are summarized as follows:

Operating current density	Faradic efficiency	Energy efficiency
27 mA/cm ² (corresponding to 9 mW/cm ²)	14.12%	3.65%
70 mA/cm ² (corresponding to 14 mW/cm ²)	4.89%	0.65%

It can be seen that larger efficiencies are achieved when the power demanded to the fuel cell is lower. However, even when a lower value of power is demanded, the Faradic efficiency obtained reveals that the percentage of methanol that is being used is only of 14% whereas for the higher current this value drops down to 5%. These results make clear that operating a passive fuel cell at a fixed current density is only worthy when low current values are demanded; otherwise the diminution in methanol concentration causes a sudden stop in fuel operation.

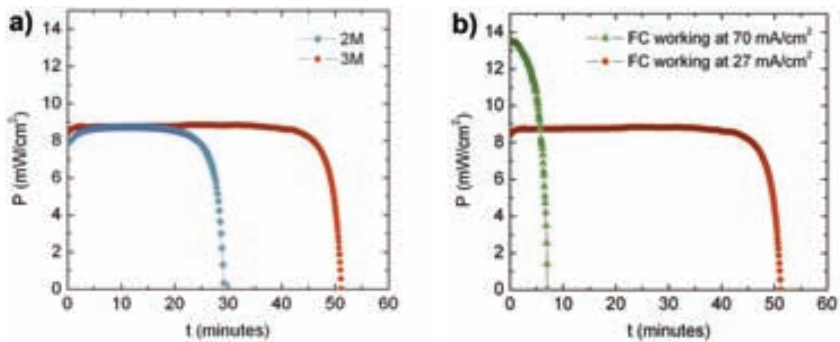


Figure 2.24 Methanol consumption of micro fuel cell. (a) Operating with two methanol concentrations delivering the same power. (b) Fuel cell with 3M methanol concentration working at two different current densities.

2.2.4.2 Fuel cell operated at constant voltage

The performance of the silicon passive DMFC was tested again at different voltage values for 2M and 4M methanol concentrations. As it can be seen in the polarization curves of Figure 2.25, the fuel cell was set at voltages of 300, 180 and 100 mV.

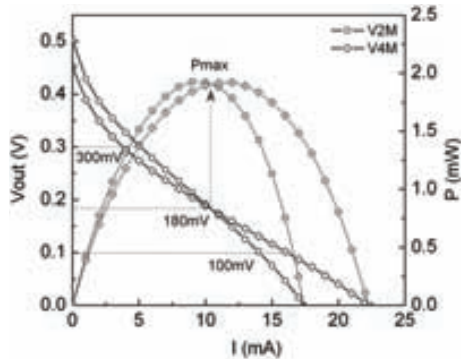


Figure 2.25 Constant voltage values chosen for the long-term operation tests.

Figure 2.26 shows the obtained transient discharging current of the cell and the corresponding delivered power when operating at the three tested voltages of 300, 180 and 100 mV with two different methanol concentrations. It can be seen that as expected, higher current values are achieved at low operating voltages. During the first 45 minutes, there was not a significant difference in the response for the two methanol concentrations except at high operating voltages, when the higher crossover rate at 4M concentration has a visible impact in the fuel cell output current. Moreover, it can be seen that a higher methanol concentration leads to a longer discharging time. The power delivered by the fuel cell at different operating conditions has been depicted in the upper part of Figure 2.26. The total delivered energy (area underneath the curves) is higher for 4M methanol concentration at all operating voltages. It can also be seen that once translated to power, those discharge curves corresponding to 100 mV contain significantly smaller areas.

Figure 2.27 show the Faradic and energy efficiencies computed from the discharge current/power versus time curves shown before. The first thing to be remarked is that the Faradic efficiency decreases when methanol concentration is increased from 2M to 4M. This is due to the larger rate of methanol crossover that takes place at higher concentrations. Moreover, the operation voltage has a significant impact on the Faradic efficiency. Maximum values were found at low discharging voltages (corresponding to high density currents). This is related to the combined effect of the partial mitigation of methanol crossover that occurs at higher fuel consumption rates and the duration of the discharging process. Figure 2.27b shows that the energy efficiency, which is much lower than the Faradic efficiency, decreases at low fuel cell operation voltages. This is due to the accumulation of power losses, responsible of the increasing deviation of the cell voltage from the thermodynamically predicted voltage. Again, higher methanol concentrations yielded lower efficiencies; mainly due to the waste of fuel taking place through crossover. A maximum energy efficiency of 6.25% was achieved when operating the cell with 2M methanol concentration at 300 mV whereas a minimum value of 2% was found with a 4M methanol fuel at 100 mV.

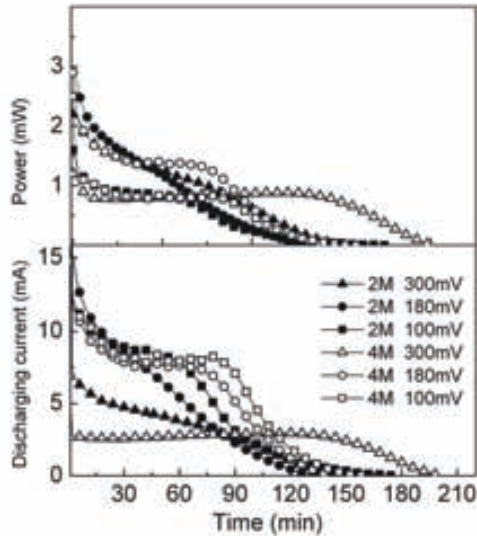


Figure 2.26 Transient discharging current and power at constant voltage for different operating points and at two different methanol concentrations.

In order to establish a comparison with other portable power sources, a line corresponding to the energy efficiency of a methanol fuel cell providing the same specific energy than a lithium-ion battery has been depicted in Figure 2.27b (efficiency calculated on the basis of a theoretical specific energy of 410 Wh/kg for a lithium battery and 6100 Wh/kg for pure methanol). It can be seen that although the efficiencies of the microdevice laid below the line, the maximum efficiency achieved is comparable to the one obtained with an alternative source.

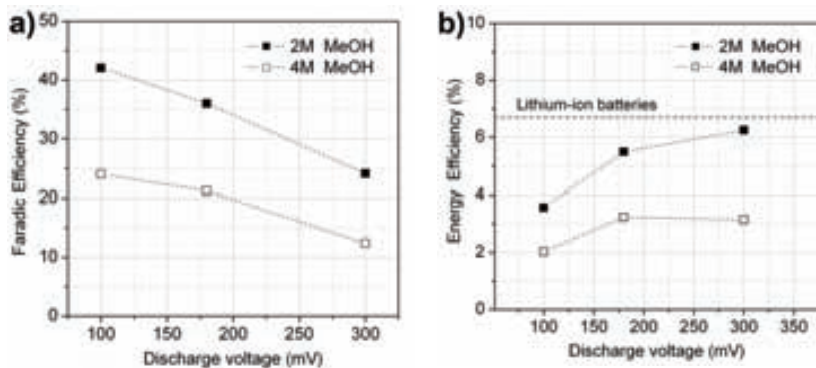


Figure 2.27 Faradic efficiency (a) and energy efficiency (b) of the micro fuel cell fuelled with 100 μ l of methanol at different concentrations and different operating points.

2.3 MICRO FUEL CELL MODELING

A computer-based model of the micro direct methanol fuel cell was developed with the purpose of reproducing the experimental results presented in the previous section. In this sense the model represents a powerful tool for future optimization of the device components and operating conditions.

Up to now, most of the models of passive fuel cells reported in the literature assume steady-state conditions that impose a constant methanol concentration in the fuel reservoir and a fully-developed concentration gradient during fuel cell performance [31, 33, 43-53]. Although this assumption can be acceptable to model the polarization curve of a system where the methanol tank volume is relatively large, this is no longer valid to reproduce the long-term operation of a fuel cell device [54, 55]. In this case, the dynamic evolution of the concentration profiles along the reservoir due to the combined effect of crossover and fuel consumption make steady-state models unable to adjust to the results recorded experimentally. For this reason, in micro fuel cells operating with a reduced methanol volume that significantly decreases during a measurement, the implementation of a transient model that accounts for these effects is mandatory.

2.3.1 Model description

A transient three-dimensional model of the passive fuel cell developed in this work was built using the software COMSOL Multiphysics®. This software uses finite element analysis to solve the system equations and allows visualizing the resulted data. For the sake of simplicity, only a fraction of the device was modeled. This fraction is a single unit that once multiplied represents the behavior of the entire device. Figure 2.28 shows a diagram of the device indicating the selected domain to be simulated.

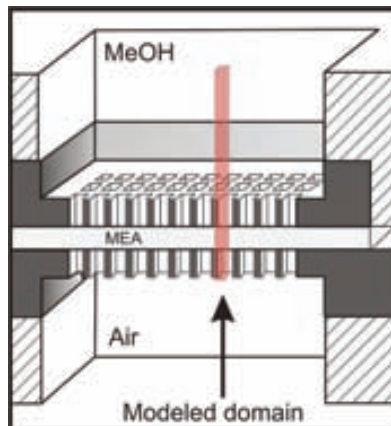


Figure 2.28 Diagram of the device showing the section that was modeled.

This selected unit cell consists of one quarter of a current collector microchannel and half the separation distance between microchannels, as shown in Figure 2.29. From top to bottom, the model includes the methanol reservoir (MR), the anode channel (AC), anode catalyst layer (ACL), proton exchange membrane (MEM), cathode catalyst layer (CCL) and cathode channel (CC). The dimensions of the model are shown in the same figure. Although the total nominal thickness of the commercial MEA is 190 μm (20 μm accounting for the catalyst layers and 170 μm for the polymeric membrane), a the SEM inspection of the cross-section of the MEA revealed the actual dimensions of these layers are 40 μm for the catalysts and 115 μm for the membrane (as seen in Figure 2.2a).

System equations have been solved through the finite element method-based software COMSOL Multiphysics. The model includes electrical, chemical and diffusive mass transport mechanisms, obtaining a complete model that was configured for transient mode simulation.

In order to simplify the model, the following assumptions were made to simplify the model:

- Mass transport in all subdomains is assumed to be only diffusion.
- The electrochemical kinetics are based on the Tafel equation approximation.
- Constant and uniform temperature is imposed in the entire fuel cell. Even though it is well-known that the electrochemical reactions in the fuel cell produce heat, it has already been proved by direct sensing and IR measurement, that due to the high thermal dissipation of silicon, the temperature rise of the device is negligible.
- The convective mass transport of CO_2 bubbles in anode channel and methanol reservoir is taken into account as diffusion transport with a velocity equivalent to the bubble rise by the buoyancy force.
- The methanol reaching the cathode by crossover is assumed to deplete instantly due to the high reaction rate with the cathode catalyst.
- Gas phase in the cathode is an ideal mixture.
- The proton exchange membrane is completely hydrated and well activated.
- Contact resistance is neglected.

All the parameters and baseline conditions employed in the model are summarized in Tables I and II included in the Appendix section.

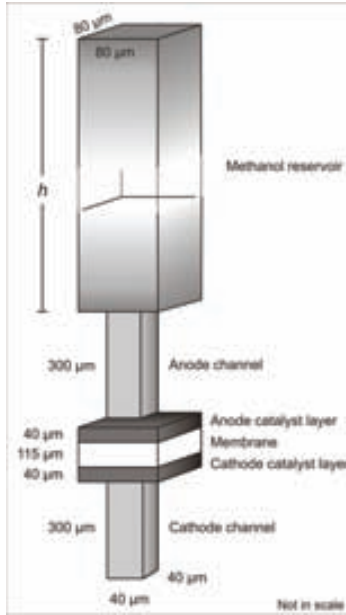


Figure 2.29 Model subdomains and dimensions.

2.3.1.1 Mass transport in anode side

The diffusion-driven mass transport in the MR, AC and ACL subdomains is considered for two species, methanol and CO_2 . Fick's law is used to describe the diffusive transport with the following expression:

$$\frac{\partial c_i}{\partial t} + \nabla \cdot (-D_i \nabla c_i + c_i \mathbf{u}) = R_i \quad (2.3)$$

where c_i denotes the concentration of species i (MeOH and CO_2), D_i denotes its diffusion coefficient, \mathbf{u} the velocity vector and R_i denotes the reaction term. The velocity vector \mathbf{u} corresponds to a convective mass transport, which is assumed to be zero for all three subdomains in the anode side since no convective flux is used to supply the methanol.

For MR and AC subdomains the convective transport of CO_2 bubbles is accounted for with an additional component in its diffusion coefficient, which allows the exit of the CO_2 specie from the fuel cell through the upper boundary of the methanol reservoir. The reaction term in these subdomains is set to zero.

In the ACL subdomain the mass transport is modeled as diffusion in a porous media, so the diffusion coefficients of methanol and CO_2 are adjusted with the porosity parameter of the catalyst layer as follows:

$$D_{\text{MeOH},\text{eff}} = D_{\text{MeOH}} \varepsilon^{1.5} \quad (2.4)$$

and

$$D_{CO_2,diff} = D_{CO_2,H_2O} e^{1.5} \quad (2.5)$$

The reaction term of the diffusion equation is defined in the ACL volume for both species. The methanol consumption N_{MeOH} is determined by the proton current density i_a by:

$$N_{MeOH} = i_a \frac{1}{6F} \quad (2.6)$$

where F is the Faraday constant.

The CO₂ production in the ACL N_{CO_2} is defined as the inverse of the methanol consumption rate:

$$N_{CO_2} = -N_{MeOH} \quad (2.7)$$

Carbon dioxide produced is diluted in the methanol solution for concentrations below its saturation concentration value $C_{CO_2(l)}^{sat}$. For higher CO₂ concentrations, there is bubbles formation, which difficult the methanol diffusion in the electrode and blocks reaction sites of the catalyst layer. This accumulation of CO₂ in the catalyst layer is considered incorporating a liquid saturation factor (s) given by:

$$s = \frac{\rho_{CO_2(g)}(1 - \omega_{CO_2})}{\rho_{CO_2(l)}(\omega_{CO_2} - \omega_{CO_2(l)}^{sat}) + \rho_{CO_2(g)}(1 - \omega_{CO_2})} \text{ for } \omega_{CO_2} \geq \omega_{CO_2(l)}^{sat} \quad (2.8)$$

and

$$s = 1 \text{ for } \omega_{CO_2} < \omega_{CO_2(l)}^{sat}$$

where ω_{CO_2} is the carbon dioxide mass fraction, calculated as:

$$\omega_{CO_2} = \frac{C_{CO_2} M_{CO_2}}{C_{MeOH} M_{MeOH} + C_{CO_2} M_{CO_2} + \frac{\rho_{H_2O}(\rho_{MeOH} - C_{MeOH} M_{MeOH})}{\rho_{MeOH}}} \quad (2.9)$$

2.3.1.2 Mass transport in membrane

Methanol crossover through the membrane is driven by electro-osmotic drag ($n_d^{H_2O}$) and the concentration gradient between anode and cathode. It is defined as an outward flux in the boundary between ACL and MEM subdomains by:

$$N_{cross} = \frac{D_{MeOH,m} C_{MeOH}}{d_m} + n_d^{H_2O} \chi_{MeOH} \frac{i_a}{F} \quad (2.10)$$

where χ_{MeOH} is the methanol molar fraction determined from its concentration in the dilute solution by:

$$\chi_{MeOH} \approx \frac{C_{MeOH}}{C_{MeOH} + 50000} \quad (2.11)$$

The methanol diffusion transport through the proton exchange membrane is based on Scott [48] diffusion coefficient approach for a Nafion membrane. A correction factor (ζ) is added to the expression to approximate it to the actual crossover amount registered in this device, as written below:

$$D_{MeOH,m} = 4.9 \times 10^{-10} \exp(2436(1/333 - 1/T)) \zeta \quad (2.12)$$

2.3.1.3 Mass transport in cathode side

The diffusion-driven transport on the CC and CCL subdomains is based on the Maxwell-Stefan diffusivity definition proposed by Curtiss and Bird [56] for an ideal gas mixture of three gases O_2 , H_2O and N_2 .

The Maxwell-Stefan Diffusion and Convection mass balance expressed in mass fractions is built upon the following equation:

$$\frac{\partial \rho_{mix} \omega_i}{\partial t} + \nabla \cdot \left(\rho_{mix} \omega_i \mathbf{u} - \rho_{mix} \omega_i \sum_{j=1}^n D_{ij} \left(\nabla x_j + (x_j - \omega_j) \frac{\nabla p}{p_{ref}} \right) - D_i^T \frac{\nabla T}{T} \right) = R_i \quad (2.13)$$

where x_j is the mole fraction of species j , ρ_{mix} denotes the density of the gas mixture, ω_j the mass fraction and R_i the reaction rate of species i , while D_{ij} is the ij component of the multicomponent Fick diffusivity matrix. The terms \mathbf{u} and D_i^T are the velocity vector corresponding to convective transport and the generalized thermal diffusion coefficient of species i . Neither of these terms are used in this case since mass transport is exclusively diffusive and the fuel cell temperature is constant and uniform.

Mass fractions are calculated by the model from the initial values defined at the cathode channel entry by $\omega_{O_2}^{ref}$ and $\omega_{H_2O}^{ref}$. The gas mixture density is calculated in the CCL and CC volumes by:

$$\rho_{mix} = \frac{\chi_{O_2} M_{O_2} + \chi_{H_2O} M_{H_2O} + \chi_{N_2} M_{N_2}}{RT} p_{ref} \quad (2.14)$$

The binary diffusivities D_{ij} for species O_2 , H_2O and N_2 used in the cathode channel are specified in Table I. For CCL subdomain the coefficients are adjusted for the porous catalyst layer as $D_{ij} = D_{ij} \epsilon^{1.5}$.

The reaction rate of species R_i is defined for the CCL volume. For the oxygen specie the reduction of concentration is due to the proton current density and the reaction with methanol from crossover through membrane, the reaction rate is defined as:

$$N_{O_2} = \frac{i_c + i_{cross}}{4F} M_{O_2} \quad (2.15)$$

while in the water production rate the electro-osmotic drag component is also included:

$$N_{H_2O} = \frac{i_c + i_{cross}}{F} \left(\frac{1}{2} + n_d^{H_2O} \right) M_{H_2O} \quad (2.16)$$

2.3.1.4 Electrochemical kinetics

The current densities of anode and cathode can be approached by the Tafel equation to simplify the complicated multistep electrochemical reactions in the catalyst layers.

The anode current density is defined in the ACL volume as:

$$i_a = i_{a0} \frac{C_{MeOH}^s}{C_{MeOH,ref}} \exp\left(\frac{\alpha_a F}{RT} \eta_a\right) \quad (2.17)$$

where i_{a0} is the exchange current density on anode, $C_{MeOH,ref}$ is the methanol reference concentration, s is the liquid saturation of ACL, α_a is the anode transfer coefficient and η_a is the anode overpotential.

In order to account for the current losses due to the methanol crossover, the current i_{cross} is obtained from the methanol flux that crosses the membrane:

$$i_{cross} = 6FN_{cross} \quad (2.18)$$

then the cathode current density expression that describes the oxygen reduction on the cathode side is defined as:

$$i_c = i_{c0} \frac{\chi_{O_2}}{\chi_{O_2,ref}} \exp\left(\frac{\alpha_c F}{RT} \eta_c\right) - i_{cross} \quad (2.19)$$

2.3.1.5 Cell performance

Once the electrode overpotentials are obtained from the equations balance and the cell current densities obtained by integrating the expressions of current on the catalysts subdomains, the cell performance can be determined as follows:

$$V_{cell} = \varphi_{eq}^c - \varphi_{eq}^a - \eta_a - \eta_c - I \frac{d_m}{\kappa_m} \quad (2.20)$$

where φ_{eq}^a and φ_{eq}^c are the thermodynamic reduction potentials of methanol oxidation and oxygen reduction. The last term of the equation accounts for the ohmic losses of the membrane, calculated from cell current density, membrane thickness d_m and proton conductivity κ_m .

2.3.2 Model validation

The model developed in this work was validated against the experimental data obtained for the fabricated micro fuel cell presented in previous chapters. In order to reproduce accurately the experimental conditions, the reservoir height h was set to a value of 3.4 mm. This height allows defining a methanol volume of 100 μL with which the fuel container of the device had been experimentally filled. The time dependent parameters included in this model such as the stabilization period before starting the measurement and the duration of the measurement were also adjusted to the ones used in experimental characterization. The methanol concentrations used for this validation were 1M, 2M and 4M. The corresponding polarization curves have been already presented in the previous chapter of this work.

2.3.2.1 Polarization curves

The model was first used to obtain the device polarization curves at different methanol concentrations. Figure 2.30 shows the results obtained by simulation and compares them to the experimental curves. As it can be seen, the simulation is in good agreement with the maximum values of current and power density for the three different modeled concentrations. The differences in the values of maximum power density between the experimental and the modeled polarization curve are smaller than 10%. These results validate the proposed model as a tool to predict the behavior of the micro direct methanol fuel cell.

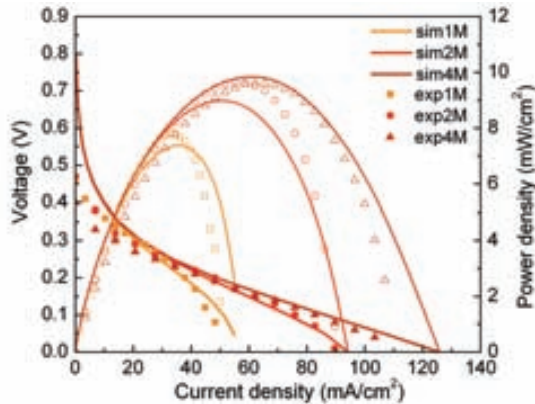


Figure 2.30 Experimental and simulated polarization curves of the micro fuel cell operating at different concentrations.

2.3.2.2 Methanol consumption and fuel cell efficiency

The model capability to simulate the transient fuel cell performance was used to predict the long-term operation of the device and obtain the faradic and energy efficiencies.

The simulated discharging curves were obtained by fixing a volume of 100 μl of methanol in the anode compartment, setting the cell to a constant voltage and computing the generated output current. Simulation was kept running until the methanol concentration in the fuel cell reservoir was completely depleted and consequently, the generated current was close to zero. The simulations were made with methanol concentrations of 2M and 4M at two different working points. These points were set to the voltage in which the device delivered the maximum power (180 mV) and a second point at the beginning of the ohmic region of the I-V curve (300 mV).

The obtained data is compared against the experimental characterization results presented in section 2.2.4.2, which were obtained for the same concentrations, working points and initial volume of methanol. Figure 2.31 shows the methanol concentration profiles in the anode reservoir, channel and electrode for the micro fuel cell working at a constant voltage with a 4M methanol concentration. The images show the concentration distribution at different times (1 min, 30 min and 2 h) visualizing the effect of methanol depletion in time characteristic of passive fuel cells directly affecting the output power withdrawn from the cell.

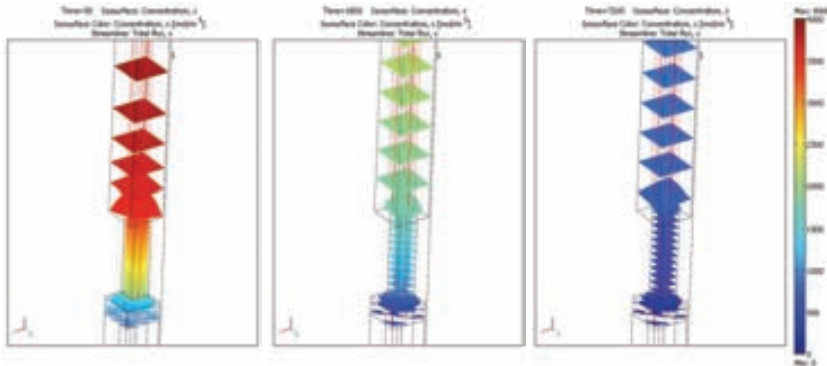


Figure 2.31 Methanol concentration profiles in the micro fuel cell at different times 1 min (left), 30 min (center) and 2 hours (right) when operating at a constant voltage with a 4M methanol concentration.

Figure 2.32 shows the comparison of the experimental and modeled data for methanol concentrations of 2M and 4M respectively. These curves show the evolution in time of the current generated by the device working at the specified voltages. From these figures it can be observed that the simulated curves reproduce quite satisfactorily the experimental behavior - it follows the initial current drop of the curve and give a fair estimate of the time of total methanol depletion.

It has to be noted that the model does not reproduce exactly the experimental behavior of the fuel cell at 4M and 180 mV – although it yields similar values for the faradic and energy efficiencies. This is due to the fact that the model is unable to introduce the experimental local disturbances caused by CO_2 bubble degassing observed experimentally when the device is operated at high current conditions.

From the simulated discharging curves the Faradic and energy efficiencies were obtained based on the equations presented in section 2.2.4. Figure 2.33 shows the comparison of experimental and simulated values of faradic and energy efficiencies obtained for the concentrations and operation points evaluated. As it can be seen, the difference between the measured and simulated efficiencies differs less than 2% in most cases, which supports the validity of the model and ensures the prediction of the micro fuel cell performance in time.

The results obtained with the described 3D transient model of the micro fuel cell suggest that it can be used to explain the system performance at different operating conditions. In this sense, the model will allow an extensive study on the parameters that contribute to the improvement of the device performance.

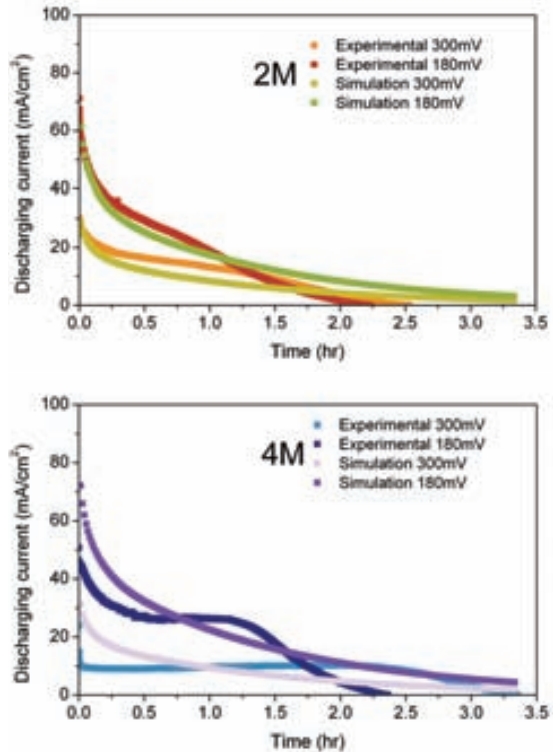


Figure 2.32 Simulated and experimental discharging current curves of the device operating at a methanol concentration of 2M and 4M.

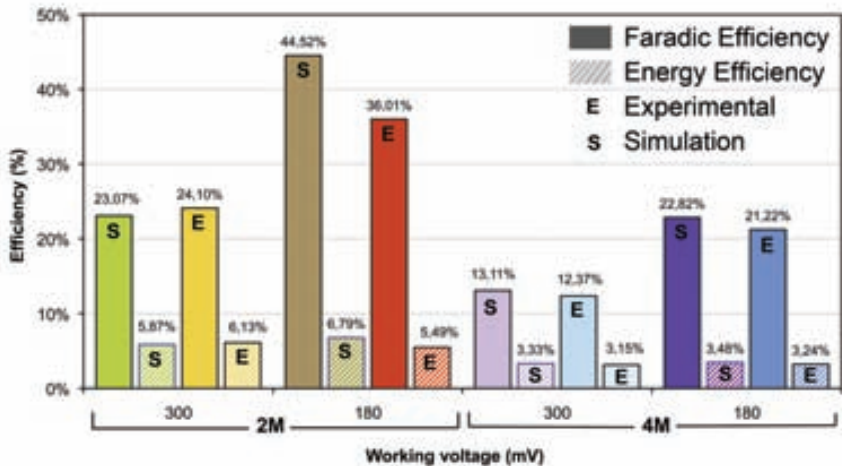


Figure 2.33 Comparison between experimental and modeled Faradic efficiency and energy efficiency of the micro fuel cell fuel at different concentrations and operating points.

2.4 DISCUSSION AND SUMMARY

In this chapter, the fabrication, characterization and modeling of a passive silicon-based direct methanol fuel cell has been presented. The device is based on a hybrid approach consisting of a commercial membrane electrode assembly pressed between two silicon microfabricated current collectors with different geometries. In this system packaging has been achieved satisfactorily by the fabrication of an acrylic casing to keep all components together.

An extensive performance characterization of the device under different conditions has been reported. The I-V characteristic curves of the micro fuel cell have been measured under various methanol concentrations showing a maximal power density around 12 mW/cm^2 at a concentration of 5M despite the mass transport limitations observed at high current densities. When fed with methanol concentration of 2M, the microdevice yields a power density of about 10 mW/cm^2 , a value comparable to values reported for larger and stainless steel microfabricated cells. This shows that in the present approach, the miniaturization of a microDMFC has been achieved successfully and avoiding any performance degradation in the process. However, it was found that unlike in other reported larger devices, feeding the cell with a higher methanol concentration had low impact in the fuel cell performance.

Temperature measurements showed that at a concentration as high as 4M the temperature of the cell did not increase beyond 1°C . Accepting the hypothesis of Liu and co-workers who relate a better performance of passive fuel cells at high concentrations to the temperature increase caused by methanol crossover, the almost insignificant temperature increase registered in the micro fuel cell would explain the small change in power density. The reason for such a small temperature increase probably lies in the high thermal conductivity of the silicon current collectors, making thermal isolation a key topic in passive MEMS-based fuel cells if higher power densities want to be achieved. As the device has been designed to be able to work regardless of its orientation, it has been shown that a maximal difference of 13% is observed at the maximum power density when the device is placed sideways making this device suitable as a portable power source.

The evaluation of current collectors design on the device performance proved that the relation between anode and cathode open ratio affects significantly the output power and stability of the fuel cell. In general, the maximum power density of a fuel cell increases with the anode open ratio whereas no significant influence is observed when the cathode open ratio is varied. This corroborates that mass transport limitations are dominated mainly by the diffusion of methanol in the anode side. Besides, it has been observed that current collector geometry impacts on the repeatability of fuel cell polarization curves. When the current collector channel density at the cathode is lower than at the anode, the device shows a gradual degradation of its performance after consecutive measurements, caused by water flooding that inhibits the cathode catalyst sites. Therefore, if stability of the fuel cell wants to be ensured, current collector open ratio in the cathode must be larger than in the anode.

The long-term discharge performance of the micro fuel cell was evaluated under different operation voltages and current densities for fuel cells working at different methanol concentrations. These tests have shown that when filled with 100 microliters of methanol at 3M, the device is able to provide a power density of 9 mW/cm² for about 50 minutes. However, when the device is operated at its maximum power, lower energy efficiency is obtained, revealing the importance of choosing the appropriate operation point in a passive fuel cell. When operated at constant voltage conditions it was found that both the Faradic and energy efficiency decrease with methanol concentration. More than the 75% of the methanol in the reservoir is wasted due to the methanol crossover when 4M concentration was used. Moreover, the highest Faradic efficiencies were found at low operation voltages due to the partial mitigation of methanol crossover that takes place at high current densities. On the contrary, energy efficiency yielded better results at high operation voltages, showing that accumulation of power losses at high current densities became more important than fuel savings. A maximum energy efficiency of 6.25% was found when discharging the cell at 2M and 300 mV, value that corresponds to 381 Wh/kg. This value is comparable with the theoretical specific energy of lithium-ion batteries (410 Wh/kg), which proves the capability of micro fuel cells to compete against this type of portable energy source.

After the characterization of the micro fuel cell, a finite element model built for this application was tuned and validated by comparing the results against experimental polarization curves and efficiencies. In this way, the model would allow to predict changes in the micro fuel cell performance when subjected to variation of the different design parameters and represents a powerful tool for future device optimization.

References in Chapter 2.

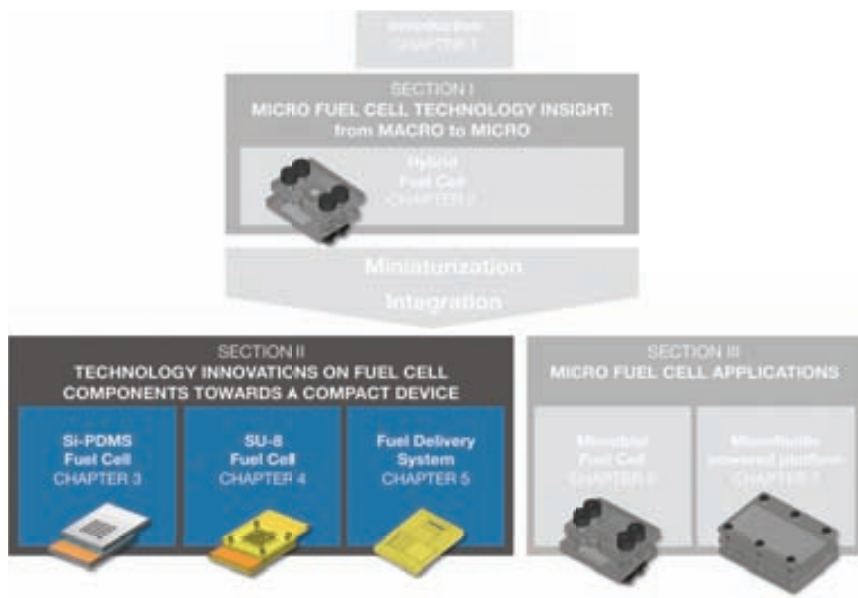
- [1] Shin S.J., Lee J.K., Ha H.Y., Hong S.A., Chun H.S. and Oh I.H. Effect of the catalytic ink preparation method on the performance of polymer electrolyte membrane fuel cells *Journal of Power Sources* **106** (2002) 146-52
- [2] Fernández R., Ferreira-Aparicio P. and Daza L. PEMFC electrode preparation: Influence of the solvent composition and evaporation rate on the catalytic layer microstructure *Journal of Power Sources* **151** (2005) 18-24
- [3] Benítez R., Soler J. and Daza L. Novel method for preparation of PEMFC electrodes by the electrospray technique *Journal of Power Sources* **151** (2005) 108-13
- [4] Dos Santos A., Carmo M., Oliveira-Neto A., Spinacé E., Rocha Poço J., Roth C., Fuess H. and Linardi M. Electrochemical and impedance spectroscopy studies in H₂ and methanol proton exchange membrane fuel cells *Ionics* **14** (2008) 43-51
- [5] Yu K.-C., Kim W.-J. and Chung C.-H. Utilization of Pt/Ru catalysts in MEA for fuel cell application by breathing process of proton exchange membrane *Journal of Power Sources* **163** (2006) 34-40
- [6] Oedegaard A., Hebling C., Schmitz A., Møller-Holst S. and Tunold R. Influence of diffusion layer properties on low temperature DMFC *Journal of Power Sources* **127** (2004) 187-96
- [7] Paganin V., Sitta E., Iwasita T. and Vielstich W. Methanol crossover effect on the cathode potential of a direct PEM fuel cell *Journal of Applied Electrochemistry* **35** (2005) 1239-43
- [8] Larminie J. and Dicks A. *Fuel Cell Systems Explained* 2003 (West Sussex, England: John Wiley & Sons)
- [9] Fuel Cell Store <http://www.fuelcellstore.com/>
- [10] Aravamudhan S., Rahman A.R.A. and Bhansali S. Porous silicon based orientation independent, self-priming micro direct ethanol fuel cell *Sensors and Actuators A: Physical* **123-124** (2005) 497-504
- [11] Kho B.K., Bae B., Scibioh M.A., Lee J. and Ha H.Y. On the consequences of methanol crossover in passive air-breathing direct methanol fuel cells *Journal of Power Sources* **142** (2005) 50-5
- [12] Verbrugge M.W. Methanol Diffusion in Perfluorinated Ion-Exchange Membranes *Journal of The Electrochemical Society* **136** (1989) 417-23
- [13] Liu J., Sun G., Zhao F., Wang G., Zhao G., Chen L., Yi B. and Xin Q. Study of sintered stainless steel fiber felt as gas diffusion backing in air-breathing DMFC *Journal of Power Sources* **133** (2004) 175-80
- [14] Kamarudin S.K., Daud W.R.W., Ho S.L. and Hasran U.A. Overview on the challenges and developments of micro-direct methanol fuel cells (DMFC) *Journal of Power Sources* **163** (2007) 743-54
- [15] Liu J.G., Zhao T.S., Chen R. and Wong C.W. The effect of methanol concentration on the performance of a passive DMFC *Electrochemistry Communications* **7** (2005) 288-94
- [16] Chen C.Y. and Yang P. Performance of an air-breathing direct methanol fuel cell *Journal of Power Sources* **123** (2003) 37-42
- [17] Jiang Y. Design, fabrication and testing of a silicon-based air-breathing micro direct methanol fuel cell *Journal of Micromechanics and Microengineering* **16** (2006) S233
- [18] Chu D. and Jiang R. Effect of operating conditions on energy efficiency for a small passive direct methanol fuel cell *Electrochimica Acta* **51** (2006) 5829-35
- [19] Liu J.G., Zhao T.S., Liang Z.X. and Chen R. Effect of membrane thickness on the performance and efficiency of passive direct methanol fuel cells *Journal of Power Sources* **153** (2006) 61-7
- [20] Bae B., Kho B.K., Lim T.-H., Oh I.-H., Hong S.-A. and Ha H.Y. Performance evaluation of passive DMFC single cells *Journal of Power Sources* **158** (2006) 1256-61
- [21] Middelhoek S. Silicon sensors *Measurement Science & Technology* **6** (1995) 1641
- [22] Baltés H., Paul O. and Brand O. Micromachined thermally based CMOS microsensors *Proceedings of the IEEE* **86** (1998) 1660-78

- [23] Shimizu T., Momma T., Mohamedi M., Osaka T. and Sarangapani S. Design and fabrication of pumpless small direct methanol fuel cells for portable applications *Journal of Power Sources* **137** (2004) 277-83
- [24] Kim Y.-J., Bae B., Scibioh M.A., Cho E. and Ha H.Y. Behavioral pattern of a monopolar passive direct methanol fuel cell stack *Journal of Power Sources* **157** (2006) 253-9
- [25] Lim S.W., Kim S.W., Kim H.J., Ahn J.E., Han H.S. and Shul Y.G. Effect of operation parameters on performance of micro direct methanol fuel cell fabricated on printed circuit board *Journal of Power Sources* **161** (2006) 27-33
- [26] Yang H. and Zhao T.S. Effect of anode flow field design on the performance of liquid feed direct methanol fuel cells *Electrochimica Acta* **50** (2005) 3243-52
- [27] Yang W.M., Chou S.K. and Shu C. Effect of current-collector structure on performance of passive micro direct methanol fuel cell *Journal of Power Sources* **164** (2007) 549-54
- [28] Chang J.-Y., Kuan Y.-D., Lee S.-M. and Lee S.-R. Characterization of a liquid feed direct methanol fuel cell with Sierpinski carpets fractal current collectors *Journal of Power Sources* **184** (2008) 180-90
- [29] Wong C.W., Zhao T.S., Ye Q. and Liu J.G. Experimental investigations of the anode flow field of a micro direct methanol fuel cell *Journal of Power Sources* **155** (2006) 291-6
- [30] Jung G.-B., Su A., Tu C.-H., Lin Y.-T., Weng F.-B. and Chan S.-H. Effects of cathode flow fields on direct methanol fuel cell-simulation study *Journal of Power Sources* **171** (2007) 212-7
- [31] O'hayre R., Fabian T., Litster S., Prinz F.B. and Santiago J.G. Engineering model of a passive planar air breathing fuel cell cathode *Journal of Power Sources* **167** (2007) 118-29
- [32] Guvelioglu G.H. and Stenger H.G. Main and interaction effects of PEM fuel cell design parameters *Journal of Power Sources* **156** (2006) 424-33
- [33] Ye Q., Zhao T.S. and Xu C. The role of under-rib convection in mass transport of methanol through the serpentine flow field and its neighboring porous layer in a DMFC *Electrochimica Acta* **51** (2006) 5420-9
- [34] Vera M. A single-phase model for liquid-feed DMFCs with non-Tafel kinetics *Journal of Power Sources* **171** (2007) 763-77
- [35] Chen R., Zhao T.S., Yang W.W. and Xu C. Two-dimensional two-phase thermal model for passive direct methanol fuel cells *Journal of Power Sources* **175** (2008) 276-87
- [36] Wagner S., Krumbholz S., Hahn R. and Reichl H. Influence of structure dimensions on self-breathing micro fuel cells *Journal of Power Sources* **190** (2009) 76-82
- [37] Liu X., Guo H., Ye F. and Ma C.F. Water flooding and pressure drop characteristics in flow channels of proton exchange membrane fuel cells *Electrochimica Acta* **52** (2007) 3607-14
- [38] Schmitz A., Tranitz M., Eccarius S., Weil A. and Hebling C. Influence of cathode opening size and wetting properties of diffusion layers on the performance of air-breathing PEMFCs *Journal of Power Sources* **154** (2006) 437-47
- [39] Schmittinger W. and Vahidi A. A review of the main parameters influencing long-term performance and durability of PEM fuel cells *Journal of Power Sources* **180** (2008) 1-14
- [40] Li H., Tang Y., Wang Z., Shi Z., Wu S., Song D., Zhang J., Fatih K., Zhang J., Wang H., Liu Z., Abouatallah R. and Mazza A. A review of water flooding issues in the proton exchange membrane fuel cell *Journal of Power Sources* **178** (2008) 103-17
- [41] Yousfi-Steiner N., Moçotéguy P., Candusso D., Hissel D., Hernandez A. and Aslanides A. A review on PEM voltage degradation associated with water management: Impacts, influent factors and characterization *Journal of Power Sources* **183** (2008) 260-74
- [42] Jiang R., Rong C. and Chu D. Determination of energy efficiency for a direct methanol fuel cell stack by a fuel circulation method *Journal of Power Sources* **126** (2004) 119-24

- [43] Chan Y.H., Zhao T.S., Chen R. and Xu C. A self-regulated passive fuel-feed system for passive direct methanol fuel cells *Journal of Power Sources* **176** (2008) 183-90
- [44] Chen R. and Zhao T.S. Mathematical modeling of a passive-feed DMFC with heat transfer effect *Journal of Power Sources* **152** (2005) 122-30
- [45] Yan T.Z. and Jen T.-C. Two-phase flow modeling of liquid-feed direct methanol fuel cell *International Journal of Heat and Mass Transfer* **51** (2008) 1192-204
- [46] Ge J. and Liu H. A three-dimensional two-phase flow model for a liquid-fed direct methanol fuel cell *Journal of Power Sources* **163** (2007) 907-15
- [47] Wang Z.H. and Wang C.Y. Mathematical Modeling of Liquid-Feed Direct Methanol Fuel Cells *Journal of The Electrochemical Society* **150** (2003) A508-A19
- [48] Scott K., Taama W. and Cruickshank J. Performance and modelling of a direct methanol solid polymer electrolyte fuel cell *Journal of Power Sources* **65** (1997) 159-71
- [49] Yang W.W., Zhao T.S. and Xu C. Three-dimensional two-phase mass transport model for direct methanol fuel cells *Electrochimica Acta* **53** (2007) 853-62
- [50] Yang W.W. and Zhao T.S. A two-dimensional, two-phase mass transport model for liquid-feed DMFCs *Electrochimica Acta* **52** (2007) 6125-40
- [51] Scott K., Argyropoulos P. and Sundmacher K. A model for the liquid feed direct methanol fuel cell *Journal of Electroanalytical Chemistry* **477** (1999) 97-110
- [52] Meyers J.P. and Newman J. Simulation of the Direct Methanol Fuel Cell *Journal of The Electrochemical Society* **149** (2002) A718-A28
- [53] Liu W. and Wang C.-Y. Three-Dimensional Simulations of Liquid Feed Direct Methanol Fuel Cells *Journal of The Electrochemical Society* **154** (2007) B352-B61
- [54] Rice J. and Faghri A. A transient, multi-phase and multi-component model of a new passive DMFC *International Journal of Heat and Mass Transfer* **49** (2006) 4804-20
- [55] Xiao B. and Faghri A. Transient modeling and analysis of a passive liquid-feed DMFC *International Journal of Heat and Mass Transfer* **51** (2008) 3127-43
- [56] Curtiss C.F. and Bird R.B. Multicomponent Diffusion *Industrial & Engineering Chemistry Research* **38** (1999) 2515-22

SECTION II

TECHNOLOGY INNOVATIONS ON FUEL CELL COMPONENTS TOWARDS A COMPACT DEVICE



3. Silicon-PDMS Micro Fuel Cell

The latest research works in micro fuel cells field have been mainly focused on the downscaling and improvement of the different elements in the device, which generally results on efficiency and power enhancement [1-6]. Although several novel architectures and packaging solutions for the miniaturization of the fuel cell components have been proposed, their monolithic integration still represents a technological challenge mainly because of the incompatibility of polymeric electrolytes (e.g. Nafion[®], Aciplex[®], Flemion[®], Fumasep[®]) with the materials typically used in microsystems technology (i.e. silicon, glass). This incompatibility is based on two main issues, the fact that polymeric membranes are unable to bond directly with the materials in which current collectors are fabricated and the volumetric changes experienced by the membranes due to variations in its water content during and after operation. This volume expansion is particularly critical as it can produce fractures in the rigid structures of the current collectors and cause the system failure. For this reason, in most of the reported works, a dedicated packaging is needed to press together all of the fuel cell components, generally using extra plates with screws or rivets such as the system presented in the previous chapter and others found in the literature [7-14]. These auxiliary elements result in bulky devices that limit miniaturization and integration. Further approaches based on the use of adhesives have been successfully explored towards the development of a planar device [15]. However, these kind of adhesive materials are not fully compatible with MEMS technology.

The work presented in this chapter describes a micro fuel cell approach compatible with MEMS technology that can overcome the major challenges encountered in silicon micro fuel cells integration. The approach consists, on one side, of the incorporation of a fine grid containing the noble metal catalysts by electrodeposition on the silicon current collectors; and on the other, of a hybrid polymeric electrolyte membrane composed of a PDMS matrix filled with the proton conducting polymer. The advantage of this approach is based on the capability of PDMS to bond to silicon by plasma oxidation, which allows the assembly of all components into a highly compact device.

The favorable outcome of this approach represents an initial step towards the miniaturization and integration of micro fuel cells as compact energy sources for autonomous systems. The integration level achieved with this approach would result in the development of further configurations such as fuel cell stacks and large-area planar fuel cells. This chapter describes the concept design, fabrication of components and device characterization. Particularly, a section is dedicated to the preparation and electrochemical characterization of the electrodeposited noble metal catalysts, as this method was developed specifically for the fuel cell electrodes.

3.1 DEVICE DESIGN

The compact direct methanol fuel cell proposed in this work was conceived as a 3-layer assembly: a PDMS-Nafion[®] polymeric electrolyte membrane sandwiched between two silicon electrode-current collector structures.

In this fuel cell approach, instead of using a pre-assembled commercial membrane electrode assembly where the catalysts are supported in a carbon-based electrode, the electrodes have been directly incorporated to the current collectors by the electrodeposition of a porous metallic layer. For this purpose, the silicon current collector plates were provided on one side of the chip by an array of through-holes for reactants supply and on the other, by a fine mesh that after being metalized, incorporate the electrodeposited catalysts.

The polymer electrolyte membrane consists in the combination of a polymeric grid of polydimethylsiloxane (PDMS) with a proton conducting polymer (liquid Nafion[®]). In this configuration, the PDMS frame acts as a mechanical support of the proton conducting polymer. Moreover, due to the flexible nature of PDMS, the polymer grid is able to adapt to the volumetric expansion of the proton conducting polymer when hydrated. PDMS is capable of directly bond to silicon, glass or other polymer after oxidizing its surface by an oxygen plasma treatment. This bonding technique has been extensively proved in microfluidic applications [16]. In this way, the silicon current collectors and the polymer electrolyte could be bonded together by oxidizing the PDMS frame. This allowed a fuel cell assembly without the need of any external casing, which results in a significant reduction of the device dimensions. Figure 3.1 shows a schematic view of the device and its features. In the following sections, the fabrication process of both of these components is described in detail.

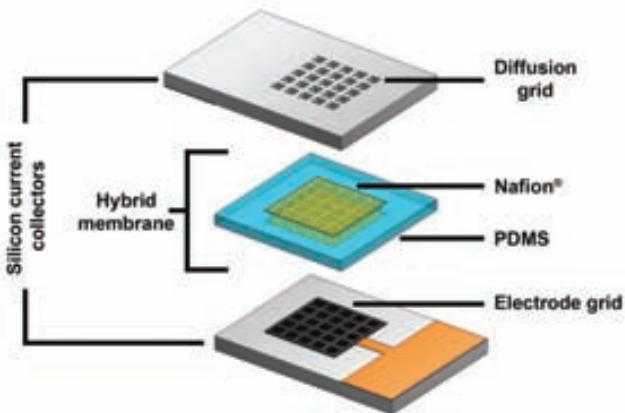


Figure 3.1 Exploded view of the compact micro direct methanol fuel cell indicating its main features.

3.2 SILICON CURRENT COLLECTORS DESIGN AND FABRICATION

In addition to the distribution of reactants and conduction of electrons produced by the fuel cell operation, these silicon current collectors also perform the electrode functions, comprising the catalysts charge required for the fuel cell reaction. In order to achieve these functionalities, the current collectors were fabricated on Silicon-on-Insulator (SOI) wafers. This kind of wafers is composed of two layers of silicon (device and handle layers) separated by a thin layer of silicon oxide. Typical thicknesses of these layers could be in the order of 2-200 μm for device layer, 0.1-10 μm for the oxide layer and 300 and up for the handle wafer [17].

In this application, the handle layer of the wafer was used to define an array of perforations that covered an area of 5 mm x 5 mm in each current collector chip. This array was named *diffusion grid*, as it is responsible of delivering the reactants to the membrane. On the other side of the wafer, the device layer was etched to define a finer mesh, matching the area under the diffusion grid. This second mesh was called *electrode grid* as it supports the platinum-based catalysts and collects the electrons generated in the electrochemical reaction.

In order to ensure the mechanical stability of the structure, the perforations in the diffusion grid were round-shaped, while the electrode grids inside these perforations were given a web shape. In this way, two types of current collectors were fabricated, which differentiate by the size of the diffusion grid perforation. This resulted in collectors with two different open ratios, which were used in anode and cathode sides respectively as, according to the observations from section 2.2.2, ensures performance stability at high power densities. Figure 3.2 shows complete views of the diffusion grids and a magnified view of the electrode grids for the two current collector types. In the figure, the silicon handle layer is depicted in blue, while the device layer is represented in red. The size of the perforations in the diffusion grid was changed in each collector while the separation between holes was kept the same. As for the electrode grid, the same combination of line width and average opening size were maintained in both designs. Table 3.1 presents the specific geometric characteristics of each current collector design.

Table 3.1 Geometrical characteristics of the current collectors.

Collector Name	Diffusion Grid			Electrode Grid	
	Circle size (μm)	Separation (μm)	Open Ratio (%)	Medium hole size (μm)	Line width (μm)
C1	100	20	75	10	5
C2	150	20	80	10	5

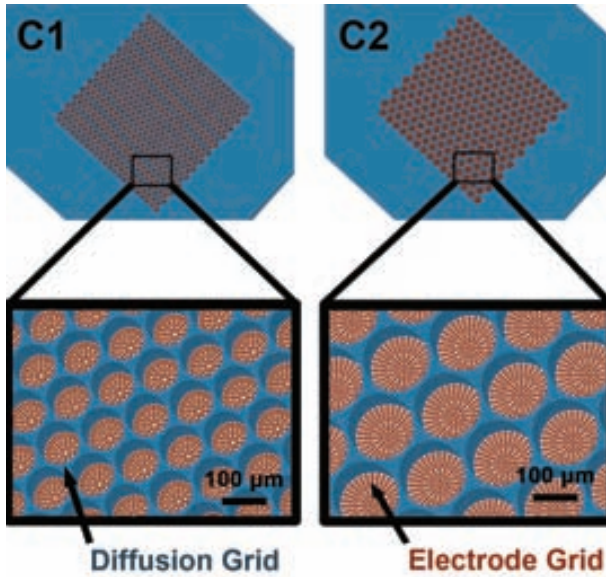


Figure 3.2 Design of current collectors fabricated in this approach.

3.2.1 Silicon microfabrication process

The main steps of the fabrication process of the current collectors are schematically summarized in Table 3.2.

Table 3.2 Main steps of the fabrication process of electrode-current collector structure.

Step	Figure	Description
a		SOI Wafer
b		Si etching (Device layer)
c		Si etching (Handle layer)
d		SiO ₂ etching
e		Ti-Ni sputtering Ni-Au electroplating
f		Pt or Pt-Ru electroplating

The process starts with a Silicon-on-Insulator wafer that had a 5 μm -thick device layer, a 2 μm -thick buried oxide and 300 μm -thick handle layer (Table 3.2 step a). The electrode grid was first defined on the topside (device layer) of the wafer by silicon DRIE process (step b). After this, a second DRIE process was performed on the wafer backside (handle layer) in order to define the diffusion grid of microchannels for fuel delivery (step c). In both processes the full thickness of the silicon layers was etched, until the buried SiO_2 was reached. After this step, the silicon wafer was cut in individual chips of 10 mm x 14 mm. At this stage, the current collectors had the grids perforating the wafer completely but a thin membrane of the buried silicon oxide layer was still blocking the openings. Thus, the buried SiO_2 was removed by dipping the chips in diluted HF (step d). Figure 3.3 shows a view of the electrode grid before and after the silicon oxide etching.

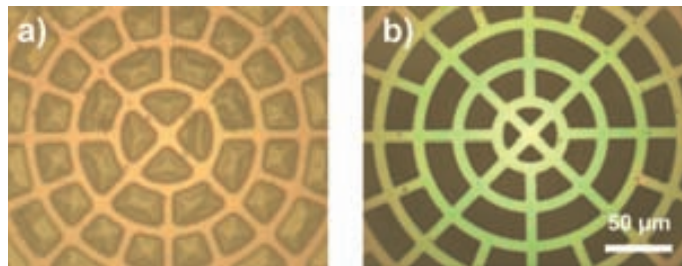


Figure 3.3 Detail of the grid inside the channel (a) before and (b) after SiO_2 removal.

The electrical conductivity was provided to the chips by metalizing the electrode grid of the device layer. To define the desired area, a PDMS frame was placed on the surface of the silicon chips, acting as a shadow mask during metallization. This allowed keeping the surface around the grid free of metal for a posterior bonding between silicon and the PDMS membrane. The metallization consisted in sputtering a Ti-Ni layer (50 and 100 nm thick) that was used as a seed layer for electroplating a 2 μm thick Ni-Au layer required for the current collection of the cell (step e). Finally, the metalized grid was electroplated with the platinum-based catalysts in order to provide the catalytic activity to the electrode grid (step f). This step is presented in greater detail in the next section. Figure 3.4 shows SEM images of the two different designs of current collectors.

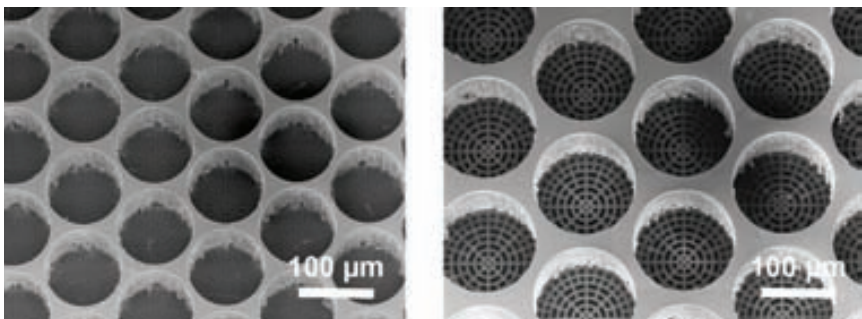


Figure 3.4 SEM images of the backside of the microfabricated current collectors.

3.2.2 Catalyst electrodeposition

The process of electrodeposition, also known as electroplating, consist on the formation of a metallic coating onto a surface by the application of an electric current. This is achieved by immersing the sample to be coated in a solution that contains a metal salt. The sample is then negatively polarized attracting in this way the positive metallic ions of the solution. When the ions reach the negatively charged electrode, it provides electrons to reduce the positively charged ions to metallic form. This technique has been proved to be extremely important in industrial applications mainly for coating surfaces to prevent oxidation and corrosion [18].

In microelectronics and microsystems technologies, this method has been used for many applications, such as electric connections, flip-chip soldering, 3D electrical interconnects, construction of mechanical parts by LIGA-process, etc. Electrodeposition is often preferred over other metallization techniques like evaporation or sputtering because it allows the formation of thicker layers [19]. Additionally, the electrodeposition of noble metals has been reported as electrochemical catalysts for fuel cells [20, 21].

The electrodeposition of Pt and Pt-Ru layers was developed in this work to incorporate them in the electrode grid of the silicon current collectors as the cathode and anode catalysts respectively. For this application, the electrodeposition conditions were adjusted to obtain metal layers with thin but rough surfaces with a large number of exposed active sites and an effective catalytic activity. The electrode layer used for the anode reaction contained ruthenium to increase the tolerance to methanol oxidation. The process used here was adapted from already reported works [22-24]. First, a characterization on plain silicon chips with a sputtered layer was performed to validate the setup and plating conditions. Then, the best conditions were used to deposit the catalysts on the microfabricated current collectors.

The setup consisted of a three electrode cell using a Ag/AgCl reference electrode (Metrohm) filled with 3M KCl and a 2 cm x 5 cm platinum mesh as counter electrode. Working electrodes used during the characterization test consisted of 10 mm x 14 mm plain Si chips sputtered with 50 nm Ti + 150 nm Ni + 50 nm Au with an available area of 1 cm². All electroplating processes and electrochemical characterization was performed with a Potenciostat/Galvanostat Autolab Pgstat12 (Metrohm Autolab). The electroplating baths were composed of 5mM H₂PtCl₆ for the cathode electrode and a mixture of 5mM H₂PtCl₆ and 5 mM Cl₃Ru for the anode electrode (both from Sigma-Aldrich) dissolved in 0.1M H₂SO₄. The depositions were done at room temperature with agitation of the solution. Figure 3.5 shows a picture of the electrochemical setup.

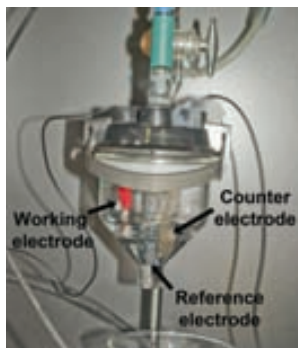


Figure 3.5 Setup used for electrochemical characterization of electrodeposited catalysts.

The electrodeposition phenomenon occurs within a range of potentials determined by the redox potential of the metal being electroplated. Polarization of the electrodes outside this potential would result in a slow deposition rate or undesirable hydrogen production. In order to find the range of potentials in which the platinum electroplating takes place, the voltage sweep was performed in the platinum bath, the obtained curve is shown in Figure 3.6.

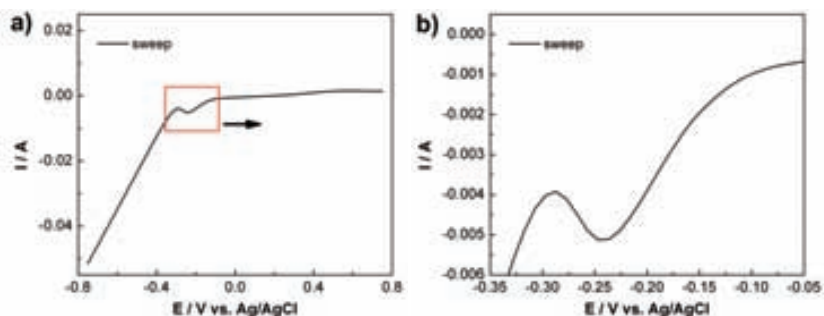


Figure 3.6 (a) Voltage sweeps to find the range of electroplating potentials. (b) Detail view of the potentials range for platinum electroplating.

From this measurement it was found that the range of potentials in which the electrodeposition can be performed lay between -0.1 and -0.25 V vs. Ag/AgCl. This is the range in which the current has a linear dependence to the potential before hydrogen production. Therefore, two potentials within this range, -0.15 and -0.20 V, were chosen to perform the plating and compare the effect of the electrodeposition potential on the deposited layer morphology and catalytic activity. The morphology was verified by SEM inspection and the catalytic activity was evaluated by cyclic voltammetry of electroplated samples.

Electrodeposition was performed by applying the potentials using a series of short pulses. This method has been previously proposed for the preparation of fuel cell electrodes showing better results than with continuous current deposition, as it permits to decrease the thickness of the catalyst layer while increasing the efficiency

of the platinum usage [20, 21, 23]. It has been also shown that this kind of electrodeposition promotes the formation of small particles, as the nucleation of deposited metal takes place in the first 10 ms [25]. The conditions of the deposition used in the characterization samples are summarized in Table 3.3.

Table 3.3 Conditions used for the characterization samples.

Sample	Material	Potential
1	Pt	-0.20 V
2	Pt	-0.15 V
3	Pt-Ru	-0.20 V
4	Pt-Ru	-0.15 V

*All tests plated with 400 pulses of 30 ms on-time and 1 s off-time.

Figure 3.7 shows SEM images of the cross section of the electroplated samples. It can be seen that layers with quite uniform thicknesses of around 200 nm were obtained. The samples showed good adhesion to the substrate and an evident roughness.

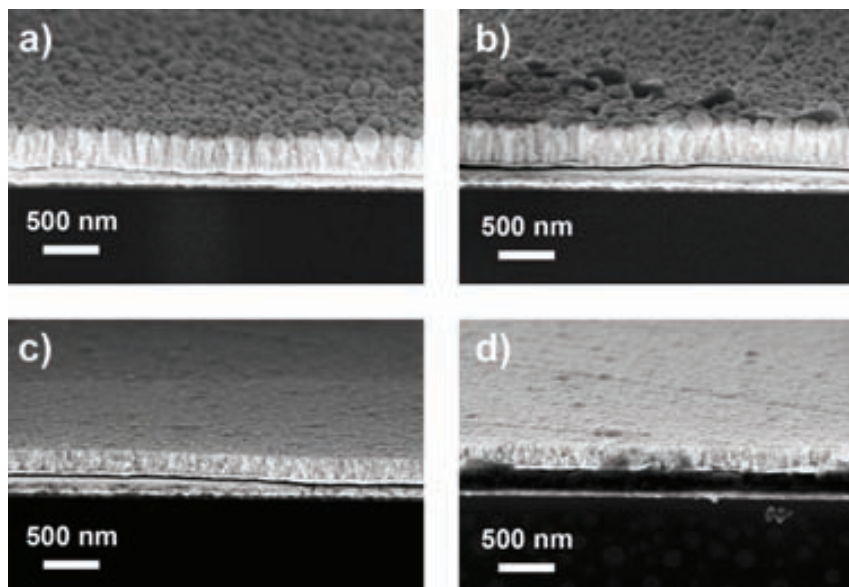


Figure 3.7 SEM images of the electroplated samples (a) Pt @ -0.20 V, (b) Pt @ -0.15 V, (c) Pt-Ru @ -0.20 V and (d) Pt-Ru @ -0.15 V.

The catalytic activity of the electrodeposited layers was evaluated by the analysis of methanol oxidation with cyclic voltammetry measurements. This technique consists of scanning the potential of the working electrode with a triangular potential waveform while measuring the resulting current. The resulting plot of current versus potential is called a cyclic voltammogram (CV) and gives time-dependent information of a large number of physical and chemical parameters [26]. In the present study, the cyclic voltammograms were used to obtain the maximum current density peaks from

the different samples. The ratio between the forward (I_f) and backward (I_b) peaks of current density determines the tolerance of the catalyst to the carbonaceous species formed during the oxidation of methanol. A low I_f/I_b ratio indicates a deficient conversion of methanol intermediates to carbon dioxide, which would lead to catalyst poisoning [27]. This relation will be used to determine the best electroplating conditions that provide high catalytic activity and methanol tolerance.

As an activation protocol before the methanol oxidation, a cyclic voltammetry was performed in 0.1M H_2SO_4 at a scan rate of 50 mV/s in the potential range from -0.29 V to 1.0 V. The CV of this activation procedure gives the information of the hydrogen adsorption of the sample, which can be related to the active area of the electroplated layer. After this activation, the cyclic voltammetry was carried out in 1M CH_3OH + 0.1M H_2SO_4 at the same scan rate and potential range.

The results of the electro-catalytic activity characterization of the electroplated Pt and Pt-Ru samples are shown in Figure 3.8. The insets in the figures show the result of the cyclic voltammetry performed in 0.1M H_2SO_4 as an activation protocol before the methanol oxidation. Table 3.4 presents the current peaks and ratios of the measured samples.

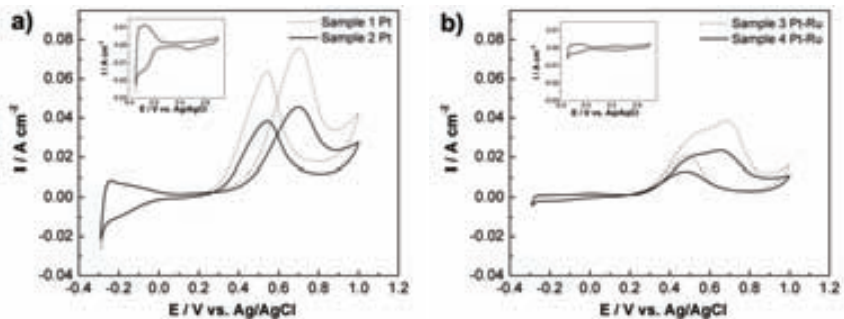


Figure 3.8 Cyclic voltammograms from the electroplated samples of (a) Pt and (b) Pt-Ru after activation and 10 measurement cycles. The insets in the figures show the hydrogen adsorption of the samples as part of the activation procedure.

Table 3.4 Methanol oxidation performance of the electroplated samples.

Sample	Material	Oxidation peak (A/cm^2)	I_f/I_b
1	Pt	0.07	1.15
2	Pt	0.045	1.18
3	Pt-Ru	0.038	1.9
4	Pt-Ru	0.022	1.9

It can be seen from the insets in the figures, that platinum samples result in higher current values than with the Pt-Ru samples. This difference indicates that the active area of the sample is larger, which is confirmed by the observation of the layer surface presented in the SEM images. Alternatively, it could also be observed that

although the samples electroplated at different potentials did not show an evident difference in the SEM images, the samples electroplated at a potential of -0.2 V (samples 1 and 3) showed higher catalytic activity.

The CVs of the methanol oxidation show that the onset potential occurs around 0.2 V and that the forward scan oxidation peak potential appears at 0.7 V for all the measured samples. It can be noticed that the forward peak current density is much higher for the Pt-only samples. This can be due to the combined effect of higher active area and increased reaction sites. However, these samples also present a high backward peak current density, which indicates a severe poisoning of the catalyst by the CO species. The co-deposited samples presented lower values of current peaks because ruthenium partially blocks the platinum surface, reducing the area of catalytic activity. However, the incorporation of this element resulted in a higher tolerance to methanol oxidation.

After this characterization, the catalytic activity and morphology of the electrodeposited metals were confirmed. For the cathode side, the conditions of sample 1 were chosen because of its high current density. For the anode side, the conditions used with sample 3 were chosen because they provide a higher current with the same I_p/I_b ratio. Hence, the electroplating of current collectors was performed in $5\text{mM H}_2\text{PtCl}_6 + 5\text{mM Cl}_3\text{Ru}$ for anode and $5\text{mM H}_2\text{PtCl}_6$ for cathode, both dissolved in $0.1\text{M H}_2\text{SO}_4$, with a signal of 400 pulses of 30 ms separated 1 s at -0.20 V potential. Figure 3.11 shows SEM images of the microfabricated current collectors after catalyst deposition.

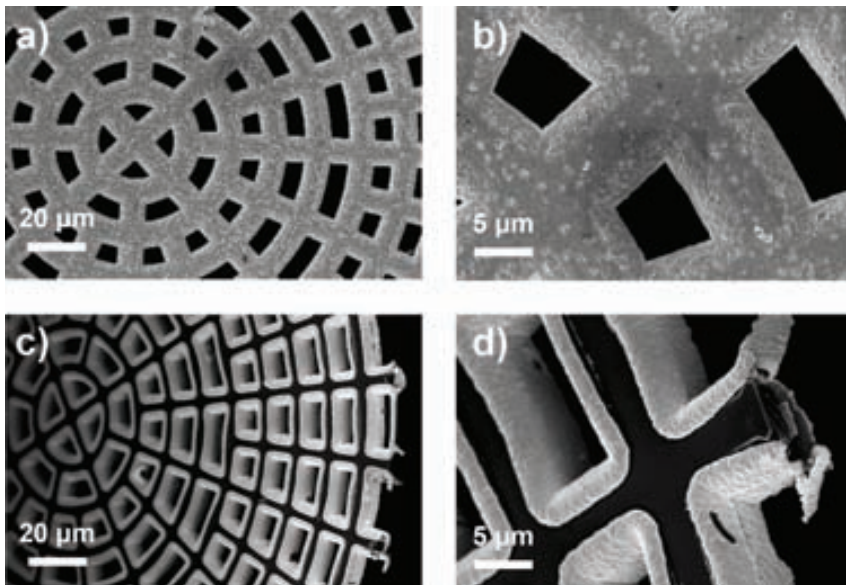


Figure 3.11 SEM images of the metalized current collectors viewed from the (a,b) front and (c,d) back of the electrode grid.

3.3 HYBRID POLYMER ELECTROLYTE MEMBRANE

Once the silicon current collectors have been fabricated and provided with the electrode layer, the fabrication and characterization of the electrolyte membrane is addressed. The hybrid polymer electrolyte membrane consists of a PDMS thin film provided with an array of through-holes that are filled with a solution of polymer electrolyte. The main fabrication steps of this hybrid membrane – schematically summarized in Figure 3.12 – are described in the present section.

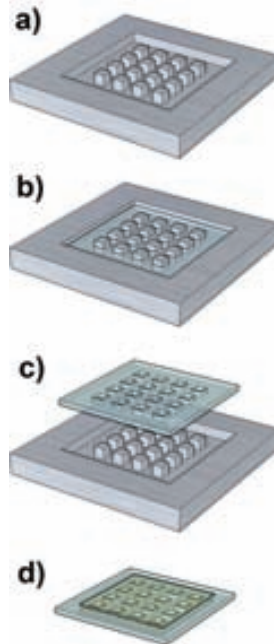


Figure 3.12. Fabrication process of hybrid membrane. a) Master microfabrication, b) PDMS pouring into master, c) PDMS extraction and d) filling of PDMS membrane with Nafion®.

3.3.1 Membrane fabrication process

The PDMS film was obtained with a standard soft-lithography technique. First, a master was microfabricated using a 100 mm SOI wafer (200 μm device layer/ 2 μm oxide layer/ 400 μm handle layer). The handle side of the wafer was used for master patterning, which was performed by DRIE process. Buried oxide was used as an etch-stop layer. Each membrane mould consisted of a 10 mm x 10 mm cavity with an array of squared microcolumns covering an area of 5 mm x 5 mm placed in the center of the cavity. In order to explore the influence of the Nafion® content in the resulting hybrid proton conducting membranes, the microcolumns of the mould have been arranged to give rise to four different array designs. Microcolumn base dimensions have been set to 250 and 500 μm and the separation between microcolumns 250 μm and 500 μm . Figure 3.13 shows a photograph of the wafer with the silicon microfabricated moulds and a SEM image of one of the silicon fabricated microcolumns arrays.

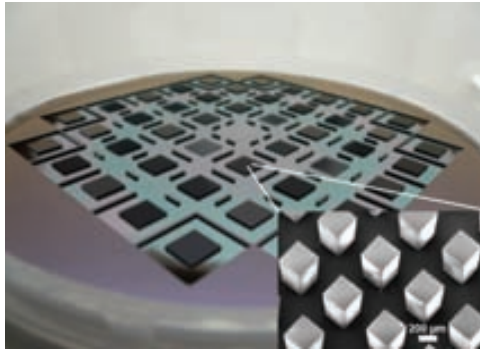


Figure 3.13 Microfabricated silicon master for PDMS membrane molding.

A volume of 30 μl of PDMS (Sylgard 184, Dow Corning Inc.) prepolymer mixture was poured onto each mould type. The polymer was carefully dropped in the corners of the mould to avoid covering the top of the microcolumns. The space between the pillars was covered by letting the polymer flow driven by capillarity forces. After this, the polymer was cured according to manufacturer specifications and extracted from the master. This procedure allowed obtaining 10 mm x 10 mm and 300 μm -thick films with the four different arrays of microperforations in its central 5 mm x 5 mm area according to Table 3.5. From the table it can be seen the value of open ratio of each membrane configuration, which indicates the amount of electrolyte that the PDMS array can contain. Figure 3.14 shows an image of one of the obtained PDMS films.

Table 3.5 Geometrical characteristics of the fabricated PDMS membranes.

Perforation size (μm)	Separation between perforations (μm)	Perforations per membrane	Open ratio %
250	250	100	25
250	500	49	12
500	250	49	49
500	500	25	25

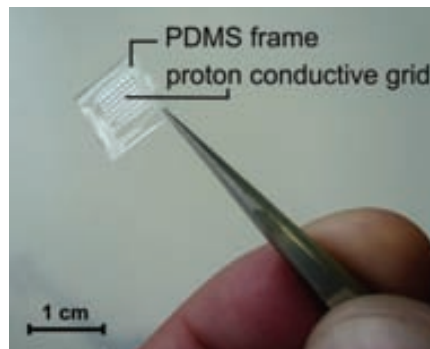


Figure 3.14 Picture of one of the microfabricated PDMS membranes.

A well-defined pattern of microcavities on all the PDMS membranes was observed, indicating an optimum transfer process from the silicon master. Once the PDMS films were released from the mould, their microperforations had to be filled with liquid Nafion[®] in order to provide the required proton conductivity to the membranes. The Nafion[®] film formation is based on a widespread procedure consisting in casting a Nafion[®] commercial ionomer dispersed in a liquid solvent (in this case, Nafion[®] 5% in aliphatic alcohols). The filling of a porous matrix with a Nafion[®] dispersion by evaporation of solvents has been carried out successfully in other materials such as porous glass and silicon [28]. In order to achieve a correct filling of the PDMS cavities with the electrolyte, the membranes were fixed in a support that stretched them and kept them tensile during the evaporation of the solvents in the Nafion[®] solution. Additionally, the central area of the membrane had to be treated with a short plasma oxidation to make its surface hydrophilic. This treatment facilitate the filling of the cavities by the Nafion[®] solution, which otherwise would be unfeasible due to the chemical composition of both materials. Figure 3.15 shows a PDMS membrane inside the support used to keep it tensile during Nafion[®] casting.

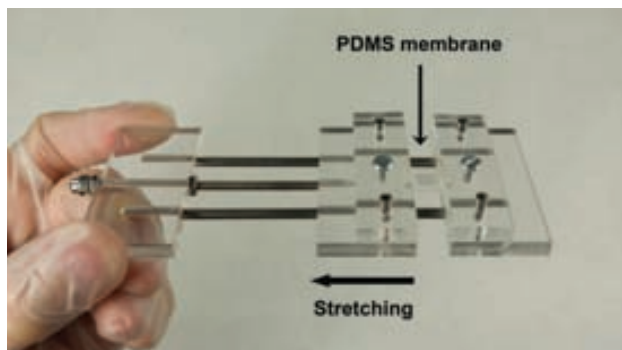


Figure 3.15 Support of PDMS membranes for filling of the cavities with electrolyte.

The volume of Nafion[®] solution used to fill the PDMS membrane was estimated according to the volume of the cavities. In order to fill the 300 μm -thick micropores, this operation had to be done several times. After solvent evaporation, cavity filling was confirmed by optical inspection. The results showed that membranes with a separation of 250 μm between perforations were incapable of withstanding the evaporation of the Nafion[®] solution without deforming. The PDMS grids in these cases were not rigid enough, which resulted in a partial Nafion[®] filling of the cavities. Examples of the Nafion[®] filling of these PDMS membranes are shown in Figure 3.16.

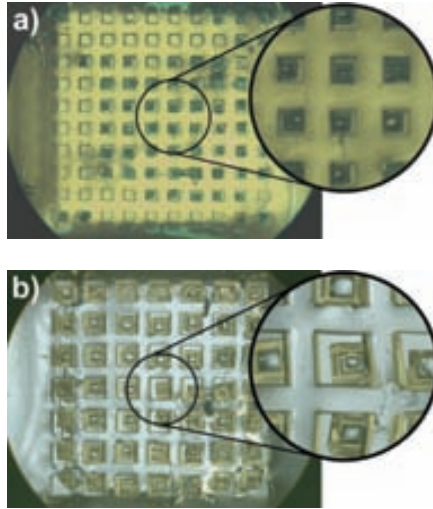


Figure 3.16 Examples of the resulting Nafion[®] filling of PDMS membranes with 250 μm separation between perforations, perforation size (a) 250 μm and (b) 500 μm .

Alternatively, the membranes with pore separation of 500 μm had the sufficient rigidity to prevent from deformation during the Nafion[®] casting process. A top-view detail of the hybrid polymer electrolyte membranes with 500 μm separation between perforations is shown in Figure 3.17. In these cases, a satisfactory filling of PDMS microcavities with Nafion[®] was achieved, validating the proton conducting electrolyte impregnation process. In addition, the fabricated membranes showed good mechanical stability after hydration without neither any fracture nor any significant buckling, proving that the PDMS matrix was capable of supporting the Nafion[®] volume expansion without affecting its structure. The resulting thickness had a variability of ± 25 microns from the PDMS membrane thickness; this dispersion in the obtained values of Nafion[®] film thickness in the cavities has been taken into account in the calculation of proton conductivity values.

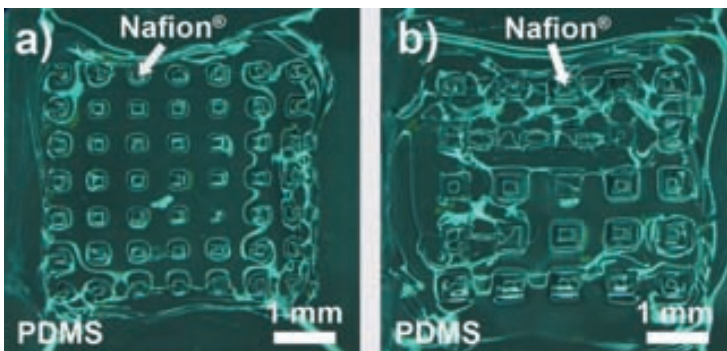


Figure 3.17 Detailed top-view of hybrid PDMS-Nafion[®] membranes with 500 μm separation between pores, perforation size (a) 250 μm and (b) 500 μm .

3.3.2 Proton conductivity characterization

In order to assess the functionality of the hybrid membranes as proton conducting electrolyte, the samples were evaluated by electrochemical impedance spectroscopy (EIS). For that purpose, membranes with 500 μm micropore separation, pore size 250 μm and 500 μm (labeled as PDMS_250 and PDMS_500, respectively) were measured. Symmetrical electrochemical cells consisting of the fabricated hybrid membranes working as electrolyte and two Au thin plates attached to the both sides of the electrolyte acting as electrodes were used. EIS measurements were performed using an Impedance/Gain-Phase Analyzer (SI 1260, Solartron Analytical) with an Electrochemical Interface (SI 1287, Solartron Analytical) in the frequency range from 0.1 Hz to 1 MHz and small ac voltage amplitude in the range between 25-100mV. Impedance spectra were acquired and analyzed with ZPlot and ZView software [29].

Proton conductivity values of the hybrid membrane were obtained by deconvolution of the different contributions using equivalent circuits as described below. Before measuring the membrane conductivity, the electrodes of the cell were short-circuited (with a known resistance instead of the membrane) in order to determine the parasitic resistance associated to the measurement setup. This series resistance was considered as an offset for the cell measurements. All measurements were carried out at room temperature in water saturated ambient air (R.H.=100%). For comparison purposes, a commercial Nafion[®] 117 film was also measured as a validation of our measurement setup and working conditions.

Prior to the measurement, the membranes had to be hydrated. As the Nafion[®] inside the PDMS membranes was already in its H⁺ form, the membranes were only soaked in deionized water at 80 °C for 3 h to completely hydrate the Nafion[®]. The Nafion[®] 117 membrane was activated and hydrated by a standard procedure [30, 31]. In this procedure, the membrane was boiled in a 3% H₂O₂ solution for 1 h and then rinsed in boiling deionized water for another hour to remove organic compounds. Then, it was boiled in 0.5 M H₂SO₄ for 1 h to remove metal compounds and replace Na⁺ with H⁺ in the Nafion[®]. Finally, it was rinsed in boiling deionized water for 1 h.

Figures 3.18a and 3.18b show the EIS spectra obtained for the two fabricated PDMS/Nafion hybrid membranes (PDMS_250, PDMS_500) and the commercial Nafion[®] 117 film. Different contributions to the total impedance corresponding to processes involving different relaxation times are expected in this electrode/electrolyte/electrode configuration. Proton/ionic conduction in the electrolyte with short relaxation times is associated to high frequencies, while long relaxation times related to charge transfer processes occurring at the electrode-electrolyte interfaces contribute at lower frequencies. A general equivalent circuit for considering these different contributions has been sketched as an inset in Figure 3.18a. The series resistance (R_s) accounts for the electrolyte resistance while the parallel R-Q (where Q is a constant phase element) refers to the electrode/electrolyte polarization (R_{el} , Q_{el}). For our particular case, two different arcs were required for fully characterize electrode/electrolyte PDMS-samples (R_{el1} - Q_{el1} and R_{el2} - Q_{el2}) probably due to some asymmetries. Values obtained after fitting EIS spectra have been listed in Table 3.6.

Values of capacitance and relaxation times listed in the table make clear that these low frequency arcs correspond to electrode processes since they compare with typical values reported for Au/Nafion interfaces, i.e. $C \sim 10^{-6} \text{ F cm}^{-2}$ and $\tau \sim 0.1\text{-}1\text{ s}$ [32]. Therefore, the series resistance obtained at high frequencies can be associated to ionic conductivity. After subtraction of the parasitic resistance associated to the measurement setup, these series resistances were used for calculating the proton conductivity of the polymeric membranes. Notice here that pure PDMS membranes do not contribute to the conductivity; EIS spectra performed (not presented here) showed for them a pure capacitive behaviour.

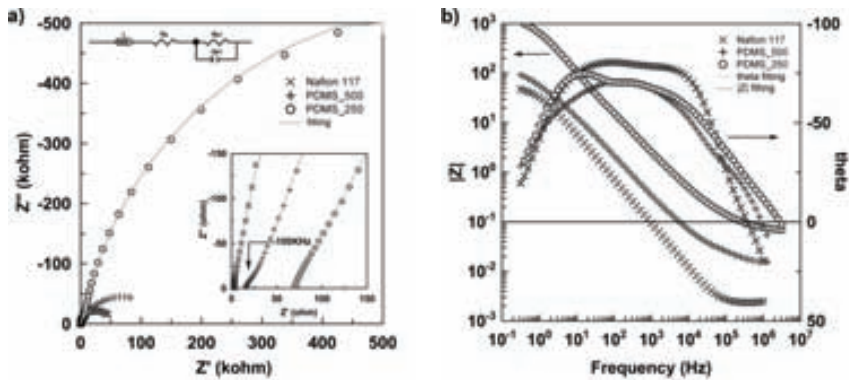


Figure 3.18 (a) Nyquist plot of the EIS measurements for different Au/electrolyte/Au cells at room temperature in water saturated air. The inserts show both a detail of the high-frequency range of impedance and the equivalent circuit used for deconvolution of the spectra. The arrow highlights the presence of a small extra arc at high frequencies for PDMS_500 which resistance was added to the R_s contribution in Table 3.6. (b) Magnitude and phase of the impedance. The gray lines correspond to equivalent circuit fittings.

Table 3.7 summarizes the values of the proton conductivity found for the different measured samples. It can be seen that a proton conductivity of $24 \pm 2 \text{ mS/cm}$ was obtained for the Nafion[®] 117 commercial film, a value within the range of conductivity values reported at current working conditions and similar setups [33-35]. The obtained conductivity of the hybrid membranes σ_{total} was 2.5 ± 0.5 and $5.8 \pm 0.5 \text{ mS/cm}$ for designs PDMS_250 and PDMS_500 respectively. These values were obtained by considering an effective membrane area of $5 \text{ mm} \times 5 \text{ mm}$ that is, including the contribution of the non-active PDMS part of the membrane. However, in the present designs, the actual area provided with proton conducting capabilities (active area A_{active}) corresponded to a 25% and 12% of the total hybrid membrane area A_{total} . Taking into account only the area filled by Nafion[®] polymer, values of conductivity associated to the electrolyte σ_{active} resulted to be $23 \pm 3 \text{ mS/cm}$ for membrane PDMS_500 and $18 \pm 2 \text{ mS/cm}$ for membrane PDMS_250.

The results confirmed the correct operation of the proton conductive polymer once embedded in the PDMS matrix and proved the viability of using the PDMS-Nafion hybrid membrane as a polymer exchange membrane. However, some variability was found in the value of conductivity for the different supporting matrices. This is probably due to the presence of air bubbles or solvent left as a consequence of the Nafion® casting process. This indicates that the drying process plays a key role in the proton conductivity of the membrane and must be taken into account in further developments.

Table 3.6 Values of the equivalent circuit elements obtained after fitting experimental impedance spectra. The table includes relaxation times for each parallel R-C circuit ($\tau = RC$). The parasitic resistance obtained after short circuiting the cell ($R_p = 1.57(2) \Omega$) was subtracted to R_s to calculate proton conductivities. The constant phase elements of the fitting process were here substituted by their equivalent capacitance.

Membrane	L (μH)	R_s (Ω)	R_{el1} ($\text{k}\Omega$)	C_{el1} (μF)	τ_{el1} (s)	R_{el2} ($\text{k}\Omega$)	C_{el2} (μF)	τ_{el2} (s)
PDMS_250	0.6(1)	64.9(7)	990(10)	0.2(1)	0.24(2)	350(10)	2.9(1)	1.0(1)
PDMS_500	0.5(1)	24.0(2)	37(4)	2.2(3)	0.09(1)	79(1)	4.6(2)	0.36(2)
Nafion 117	0.2(1)	2.3(1)	51(2)	3.2(2)	0.16(2)	-	-	-

Table 3.7 Summary of membrane parameters and measured proton conductivities.

Membrane	thickness (μm)	A_{active} (cm^2)	$A_{\text{active}}/A_{\text{total}}$	σ_{active} (10^{-3} S/cm)	σ_{total} (10^{-3} S/cm)
PDMS_250	325 ± 25	0.0306	0.122	18 ± 2	2.5 ± 0.5
PDMS_500	325 ± 25	0.0625	0.25	23 ± 3	5.8 ± 0.5
Nafion 117	170 ± 10	1.0	1.0	24 ± 2	24 ± 2

Moreover, results show that as expected, higher content of proton conductive polymer increases the overall proton conductivity of the hybrid membranes. Thus, once the proper operation of the proton conductive polymer embedded in the PDMS matrix is fully ensured, the resulting conductivity of the hybrid membrane will be strongly related to the shape, width and distribution of the microperforations. Although in the present cases the percentage of Nafion® content was kept low to ensure the mechanical stability of the membrane, the simplicity of the technology required to fabricate the membrane allows envisaging future designs with an optimal relation between both polymers, resulting in a higher overall proton conductivity of the hybrid membrane.

3.4 FUEL CELL ASSEMBLY AND CHARACTERIZATION

The characterization of the fabricated components as a complete fuel cell system was performed in three steps. First, the performance of the electroplated current collectors was evaluated by the characterization of a fuel cell with two current collectors and a Nafion® 117 membrane using a methacrylate casing joined by screws to press all components together. After this, the same micro fuel cell

assembly was tested with a hybrid membrane of design PDMS_500 as the electrolyte. Finally, these components were bonded by an oxygen plasma treatment to obtain a compact fuel cell. In all configurations, the current collectors of designs C1 and C2 were used as anode and cathode respectively. The polarization curves of the micro fuel cells were measured with 2M methanol concentration at room temperature.

The Nafion[®] 117 membrane was activated following the procedure described in the previous section, then it was assembled between the collectors and the polarization curves were measured. After this, the PDMS-Nafion[®] membrane was hydrated in deionized water at 80° for 3 hours, assembled in the micro fuel cell and equally characterized. In both cases, the open circuit voltage of the fuel cell was monitored after methanol filling until it reached a stable value. The polarization curves were measured after this condition was achieved. Figure 3.19 shows the polarization curves of the micro fuel cells pressed with the methacrylate casing using a Nafion[®] 117 membrane and a PDMS-Nafion hybrid membrane.

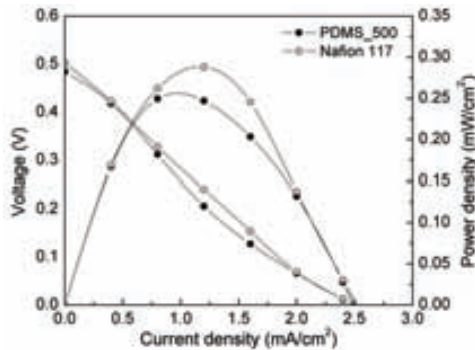


Figure 3.19 Polarization curves of the micro fuel cell pressed by an external casing using a hybrid PDMS-electrolyte membrane and a Nafion[®] 117 film.

As it can be seen from the figure, the measured open circuit voltage reached 500 mV in both experiments. Both curves present strong ohmic limitations that could be attributed to a restricted diffusion of methanol to the catalysts. Maximum power densities of 0.28 and 0.25 mW/cm² were obtained by the fuel cell with Nafion[®] membrane and PDMS_500 membrane respectively, while the maximum current in both cases was 2.5 mA/cm². Even though the active area in the hybrid membrane is 75% less than the total area of electrolyte, the difference between the maximum power densities was only 10%. This demonstrates that the use of the PDMS hybrid membrane was not the limitation of the system.

After these tests, the current collectors and the hybrid PDMS membrane were bonded to characterize the performance of the device without the external casing. The bonding of the fuel cell components was performed by oxygen plasma treatment on the surface of the PDMS using a BD-20AC Hand-Held Laboratory Corona Treater (Electro-Technic Products, Inc.). The procedure – depicted in Figure 3.20 – consisted of 30 s plasma treatment at STP conditions, first on one side of the membrane, which

was immediately put in contact with one current collector (Fig. 3.20a), then on the other side of the membrane (Fig. 3.20b), placing the second collector on top (Fig. 3.20c). To prevent Nafion® from any damage caused by the plasma treatment [36], the central area of the membrane was covered by a squared Teflon piece during this process. The entire assembly was then pressed between two glass slides and heated for 30 min at 120 °C. After this, the device was cooled down to room temperature by natural convection and removed from the glass slides. Figure 3.21 shows the micro fuel cell bonded together by the polymer membrane without any additional casing.

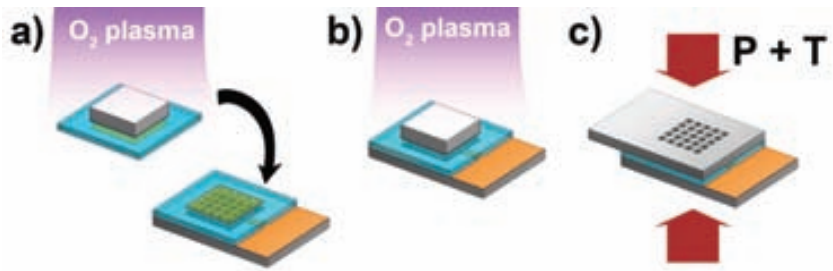


Figure 3.20 The bonding process of the micro fuel cell components. First, oxygen plasma treatment on one side of the PDMS membrane (covering the proton conducting polymer with a piece of Teflon) and placing over a current collector (a). Then a plasma oxidation on the other side of the membrane after which the second current collector was placed on top (b). Finally, a thermal treatment pressing the 3 components together (c).

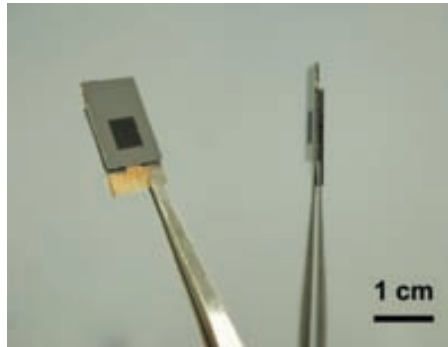


Figure 3.21 Pictures of the complete micro fuel cell after bonding.

Before characterizing the micro fuel cell performance, the complete device was soaked in deionized water at 80 °C for 3 hours in order to re-hydrate the solidified Nafion® inside the PDMS membrane. An optical inspection under the microscope after each of the fabrication steps revealed that both silicon grids were capable of withstanding all the steps in the process. The structures showed strong mechanical properties even after the volume expansion of Nafion® when hydrated. Figure 3.22 shows images of the silicon grids after the hydration process.

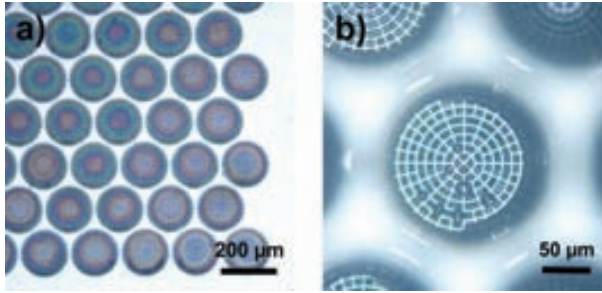


Figure 3.22 Microscope images of the device after bonding and hydration.

The polarization curves of the bonded micro fuel cell were measured with methanol concentration of 2M at room temperature. Figure 3.23 shows the obtained polarization curve, which is compared to the one obtained with the same components but pressed with the external casing.

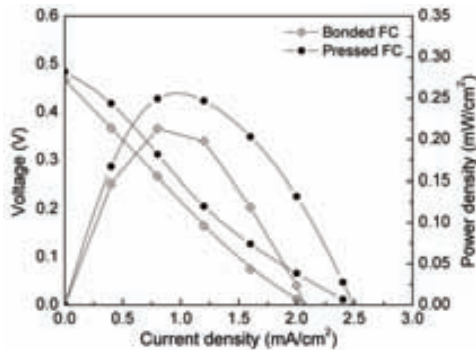


Figure 3.23 Polarization curves of the micro fuel cell after bonding.

As it can be seen, the micro fuel cell reached a similar open circuit voltage as the previous measurements. The ohmic restrictions and reduced reaction sites were again the main limitation in the system, showing only a slight decrease in the power density measured after the device was bonded, which reached a maximum value of 0.21 mW/cm².

3.5 DISCUSSION AND SUMMARY

This chapter reported a novel and simple approach to the development of a compact micro direct methanol fuel cell. The device consists of a hybrid polymer membrane as a straightforward integrable electrolyte for silicon current collectors. These current collectors consist in microfabricated silicon chips that incorporate a fine electrode grid. The membrane combines two polymers with different functionalities, Nafion[®] as a proton conducting material and PDMS as a flexible mechanical support. The compatibility of this membrane with MEMS fabrication processes lies in the acknowledged bonding capabilities of PDMS polymer to materials typically used in microsystems technologies – such as silicon, silicon dioxide and glass – as well as its ability to withstand variations of the Nafion[®] volume.

The developed components have proved their operation after being individually characterized, which validates this approach as a proof-of-concept towards a compact micro fuel cell device. However, the magnitude of the power obtained from the micro fuel cell is rather low mainly due to the existence of severe ohmic losses that can be attributed to the limited performance of the integrated electrodes. Nevertheless, the obtained results are encouraging and there are many variables involved in the system that are suitable for optimization, which would lead to performance improvement.

Silicon current collectors should be enhanced by the optimization of the structures on both sides. Part of the work would be directed to improving the distribution of reactants, by increasing the open ratio of the diffusion grid while ensuring the mechanic stability of the structure. In particular, the electrode grid should be refined, either by the reduction of the features in the structure design or by the inclusion of a porous gas diffusion layer. This porous element could be microfabricated in the same device or included afterwards as an additional component. Its purpose would be to increase the number of available reaction sites. On the other hand, there is still a long way for optimizing the catalysts electroplating. In this sense, some more work still has to be done to find better conditions that maximize the methanol oxidation keeping metal content low.

References in Chapter 3.

- [1] Liu J.G., Zhao T.S., Chen R. and Wong C.W. The effect of methanol concentration on the performance of a passive DMFC *Electrochemistry Communications* **7** (2005) 288-94
- [2] Chang C.-L., Chang T.-C., Ho W.-Y., Hwang J.J. and Wang D.-Y. Electrochemical performance of PEM fuel cell with Pt-Ru electro-catalyst layers deposited by sputtering *Surface and Coatings Technology* **201** (2006) 4442-6
- [3] Wong C.W., Zhao T.S., Ye Q. and Liu J.G. Experimental investigations of the anode flow field of a micro direct methanol fuel cell *Journal of Power Sources* **155** (2006) 291-6
- [4] Antolini E., Lopes T. and Gonzalez E.R. An overview of platinum-based catalysts as methanol-resistant oxygen reduction materials for direct methanol fuel cells *Journal of Alloys and Compounds* **461** (2008) 253-62
- [5] Kamarudin S.K., Daud W.R.W., Ho S.L. and Hasran U.A. Overview on the challenges and developments of micro-direct methanol fuel cells (DMFC) *Journal of Power Sources* **163** (2007) 743-54
- [6] Jeng K.-T., Chien C.-C., Hsu N.-Y., Yen S.-C., Chiou S.-D., Lin S.-H. and Huang W.-M. Performance of direct methanol fuel cell using carbon nanotube-supported Pt-Ru anode catalyst with controlled composition *Journal of Power Sources* **160** (2006) 97-104
- [7] Shimizu T., Momma T., Mohamedi M., Osaka T. and Sarangapani S. Design and fabrication of pumpless small direct methanol fuel cells for portable applications *Journal of Power Sources* **137** (2004) 277-83
- [8] Lu G.Q., Wang C.Y., Yen T.J. and Zhang X. Development and characterization of a silicon-based micro direct methanol fuel cell *Electrochimica Acta* **49** (2004) 821-8
- [9] Chan S.H., Nguyen N.T., Xia Z.T. and Wu Z.G. Development of a polymeric micro fuel cell containing laser-micromachined flow channels *Journal of Micromechanics and Microengineering* **15** (2005) 231-6
- [10] Lim S.W., Kim S.W., Kim H.J., Ahn J.E., Han H.S. and Shul Y.G. Effect of operation parameters on performance of micro direct methanol fuel cell fabricated on printed circuit board *Journal of Power Sources* **161** (2006) 27-33
- [11] Esquivel J., Sabaté N., Santander J., Torres N. and Cané C. Fabrication and characterization of a passive silicon-based direct methanol fuel cell *Microsystem Technologies* **14** (2008) 535-41
- [12] Motokawa S., Mohamedi M., Momma T., Shoji S. and Osaka T. MEMS-based design and fabrication of a new concept micro direct methanol fuel cell (μ -DMFC) *Electrochemistry Communications* **6** (2004) 562-5
- [13] Yeom J., Mozsgai G.Z., Flachsbarth B.R., Chohan E.R., Asthana A., Shannon M.A. and Kenis P.J.A. Microfabrication and characterization of a silicon-based millimeter scale, PEM fuel cell operating with hydrogen, methanol, or formic acid *Sensors and Actuators B: Chemical* **107** (2005) 882-91
- [14] Aravamudhan S., Rahman A.R.A. and Bhansali S. Porous silicon based orientation independent, self-priming micro direct ethanol fuel cell *Sensors and Actuators A: Physical* **123-124** (2005) 497-504
- [15] Schmitz A., Tranitz M., Wagner S., Hahn R. and Hebling C. Planar self-breathing fuel cells *Journal of Power Sources* **118** (2003) 162-71
- [16] Nguyen N.T. and Wereley S.T. *Fundamentals and Applications of Microfluidics* 2002: Norwood: Artech House)
- [17] Ultrasil SOI Wafer Technology <http://www.ultrasil.com/>
- [18] Kanani N. *Electroplating: basic principles, processes and practice* 2004 (Oxford, UK: Elsevier, Ltd.)
- [19] Schwarzscher W. Electrodeposition: A Technology for the Future *Electrochemical Society Interface* (2006) 32-5
- [20] Evans S.A.G., Terry J.G., Plank N.O.V., Walton A.J., Keane L.M., Campbell C.J., Ghazal P., Beattie J.S., Su T.-J., Crain J. and Mount A.R. Electrodeposition of platinum metal on TiN thin films *Electrochemistry Communications* **7** (2005) 125-9

- [21] Kim H., Subramanian N.P. and Popov B.N. Preparation of PEM fuel cell electrodes using pulse electrodeposition *Journal of Power Sources* **138** (2004) 14-24
- [22] Tripkovic A.V. Methanol oxidation at platinum electrodes in acid solutions: comparison between model and real catalysts *Journal of the Serbian Chemical Society* **71** (2006) 1333-43
- [23] Wei Z.D., Chan S.H., Li L.L., Cai H.F., Xia Z.T. and Sun C.X. Electrodepositing Pt on a Nafion-bonded carbon electrode as a catalyzed electrode for oxygen reduction reaction *Electrochimica Acta* **50** (2005) 2279-87
- [24] Liu H., Favier F., Ng K., Zach M.P. and Penner R.M. Size-selective electrodeposition of meso-scale metal particles: a general method *Electrochimica Acta* **47** (2001) 671-7
- [25] Penner R.M. ChemInform Abstract: Mesoscopic Metal Particles and Wires by Electrodeposition *ChemInform* **33** (2002) no-no
- [26] Wang J. *Analytical Electrochemistry, Second Edition* 2000 (New York, NY: Wiley-VCH)
- [27] Jingjie W., Haolin T., Mu P., Zhaohui W. and Wentao M. Novel methanol electro-oxidation catalyst assisting with functional phthalocyanine supports *Electrochimica Acta* **54** (2009) 1473-7
- [28] Nam-Trung N. and Siew Hwa C. Micromachined polymer electrolyte membrane and direct methanol fuel cells—a review *Journal of Micromechanics and Microengineering* **16** (2006) R1
- [29] Johnson D. *ZView and ZPlot: a Software Program for IES Analysis, Version 2.8* 2002 (Southern Pines, NC: Scribner Associates, Inc.)
- [30] Davila D., Esquivel J.P., Vignes N., Sanchez O., Garrido L., Tomas N., Sabate N., Del Campo F.J., Munoz F.J. and Mas J. Development and optimization of microbial fuel cells *Journal of New Materials for Electrochemical Systems* **11** (2008) 99-103
- [31] Sim W.Y., Kim G.Y. and Yang S.S. Fabrication of micro power source (MPS) using a micro direct methanol fuel cell (mu DMFC) for the medical application *14th IEEE International Conference on Micro Electro Mechanical Systems, Technical Digest* (2001) 341-4
- [32] Ma S., Kruse A., Siroma Z. and Yauda K. ESPEC Technology Report No 20 *Report* **2** (2005) 12
- [33] Neburchilov V., Martin J., Wang H. and Zhang J. A review of polymer electrolyte membranes for direct methanol fuel cells *Journal of Power Sources* **169** (2007) 221-38
- [34] Smitha B., Sridhar S. and Khan A.A. Solid polymer electrolyte membranes for fuel cell applications—a review *J. Membrane Science* **259** (2005) 16
- [35] Jiang R., Kunz H.R. and Fenton J.M. Composite silica/Nafion membranes prepared by tetraethylorthosilicate sol-gel reaction and solution casting for direct methanol fuel cells *J. Membrane Science* **272** (2006) 8
- [36] Ramdutt D., Charles C., Hudspeth J., Ladewig B., Gengenbach T., Boswell R., Dicks A. and Brault P. Low energy plasma treatment of Nafion membranes for PEM fuel cells *Journal of Power Sources* **165** (2007) 41-8

4. SU-8 Micro Fuel Cell

In the search for a completely integrated and low cost device, polymeric materials have recently been proposed to produce micro fuel cell components. Due to their fast and versatile microfabrication methods, polymers have already proven to be suitable for an assortment of on-chip functions and applications [1]. Interesting approaches have been reported in the last few years concerning micro fuel cell developments, e.g. Shah et al. [2] used different microfabrication techniques to develop a micro fuel cell where polydimethylsiloxane (PDMS) was used as cell support and housing and Chan et al. [3] micromachined Gaussian-shaped microchannels in polymethylmethacrylate (PMMA) using a CO₂-laser obtaining a high power hydrogen-fed micro fuel cell. Moreover, UV-sensitive resists such as SU-8 have proved to be excellent candidates to obtain small and very precise microstructured polymeric components [4], e.g. Hsieh et al. [5] reported the use of metalized UV-sensitive resist to obtain flow field plates and Cha et al. [6] used the same material to fabricate current collectors in one of the first reported attempts of obtaining an all-polymer microDMFC. Recently, Weinmueller et al. [7] reported a microDMFC based on the microstructuring of a metalized thin photosensitive polymer film, in which the flexible capabilities of SU-8 resist were emphasized.

In the following chapter, a compact micro DMFC where all components are fabricated with SU-8 resists is presented. Furthermore, the present development takes advantage not only of the above-mentioned structural and mechanical properties of these resists but also exploits the capability of SU-8 components to bond to each other by a hot-pressing process to obtain a compact micro direct methanol fuel cell. In addition, issues such as the reduction of device complexity and final cost have determined the device design, conceived to work under passive operation (fuel transport by diffusion) with a minimum amount of Pt catalyst. As will be shown, all fuel cell components are first independently characterized and validated. Then, assembly is carried out to evaluate the fuel cell performance under different methanol concentrations and temperatures.

4.1 DESCRIPTION OF DEVICE DESIGN

The aim of the present development was obtaining a simple and compact design of a micro fuel cell. For this reason, the system is based on a diffusion-driven feeding of methanol and air, which reduces complexity and allows elimination of all ancillary devices. The proposed micro fuel cell consists of an assembly of three components made of SU-8 photoresist: a membrane electrode assembly (MEA) sandwiched between two current collectors. Figure 4.1 depicts an exploded view of the proposed fuel cell showing the basic structure of both MEA and current collectors.

The MEA consists of a 10 mm x 10 mm wide SU-8 membrane with a central area of 5 mm x 5 mm provided with an ordered array of square micropores. These micropores are filled with a proton exchange polymer and are responsible of the proton conductivity of the SU-8 membrane. In this configuration, the SU-8 structure acts as a mechanical support of the proton conducting polymer and at the same time offers the possibility of being bonded directly to other SU-8 fuel cell components. Total thickness of the SU-8 membrane was set at 170 μm , as this is the nominal thickness of a Nafion[®] 117 film. The rigidity of SU-8 allowed obtaining membranes with a higher open ratio than those obtained with PDMS, as the ones described in the previous chapter. For this reason, membranes with three different array designs were fabricated; the micropores side-length was fixed at 250 μm and increasing membrane open-ratios were defined by setting pore separations at 250 μm , 100 μm and 50 μm in order to maximize proton conductive area without compromising the mechanical stability of the SU-8 structure. After that, the active area was coated with thin layers of carbon-based electrodes. The SU-8 frame around the active area was left uncovered for subsequent bonding to the current collectors.

The SU-8 current collectors have a dimension of 10 mm x 14 mm and a thickness of 250 μm . The structures are also provided with a grid of through-holes over a 5 mm x 5 mm area that is coincident with the active area of the MEA. In this way, the SU-8 structures act as current collectors, and at the same time deliver the reactants to both sides of the MEA by diffusion. In this case, two different designs of current collector were fabricated for anode and cathode sides; both designs are provided with squared through-holes of 100 μm side-length but separations between holes are set at 50 μm at the anode and 100 μm at the cathode. It has been demonstrated that in passive microDMFC the unbalancing of cathode and anode open ratios (e.g. area exposed to reactants versus total area) prevents cathode flooding and minimizes methanol crossover [8]. Electrical conductivity of the structures was provided by partially metalizing their surface. A surrounding frame was left uncovered to allow bonding to the MEA, as is indicated in Figure 4.1.

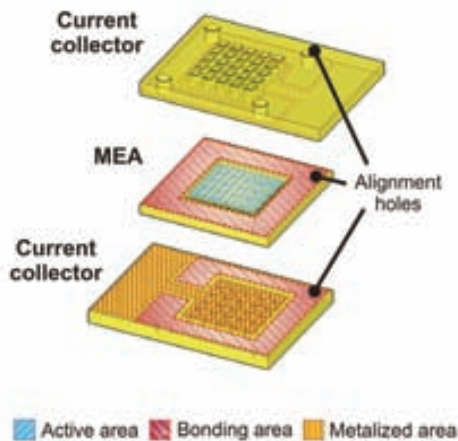


Figure 4.1 Exploded view of SU-8 micro fuel cell components and its main parts.

4.2 FABRICATION AND CHARACTERIZATION OF SU-8 FUEL CELL COMPONENTS

The photolithography process was optimized for obtaining suitable released SU-8 structures that were able to bond to each other by a subsequent hot-pressing process. Lithography parameters such as baking times and exposure dose have to be adjusted to find a trade-off between a full exposure and a photoresist polymerization level suitable for thermal bonding [9].

The lithography of the SU-8 components was performed on 500 μm thick, single side polished, 100 mm Si wafers. The first step consisted of the deposition of a sacrificial layer that will be removed at the end of the process to release the SU-8 structures. For this, a layer of Omnicoat™ (Microchem Corp., Newton, MA, USA) was spin coated onto the substrate (speed: 2000 rpm, time: 35 s) followed by a baking step of 1 min at 200 °C to vaporize the solvent. From this point different processes were used for the fabrication of the current collectors and the membrane electrode assemblies. Current collectors were fabricated using a single layer of SU-8 100, while membranes needed a multilayer process of SU-8 50 (both from Microchem Corp.). Figure 4.2 shows a silicon wafer after SU-8 development.

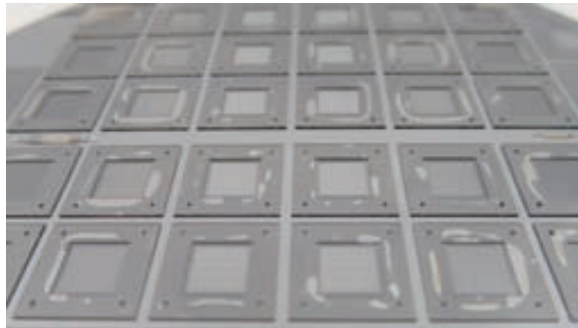


Figure 4.2 Silicon wafer after SU-8 photoresist development.

4.2.1 Fabrication of the Membrane Electrode Assembly

The fabrication of the SU-8 membrane electrode assembly consists of a series of steps that can be grouped in three main stages: 1) obtaining of the photoresist structures by the UV lithography process; 2) functionalization of the membranes by filling the cavities in the membranes with a proton exchange polymer and 3) carbon-based electrode deposition by air spray. Each of these steps is described in detail in the following sections and can be followed in Figure 4.3.

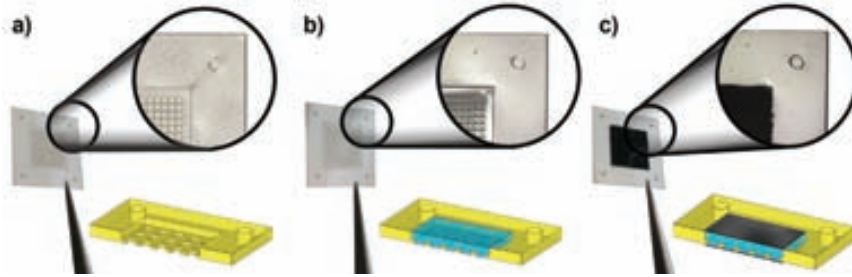


Figure 4.3 Pictures and cross-sectional views of the different stages in the Membrane Electrode Assembly fabrication: (a) SU-8 porous membrane released from substrate, (b) filling of micropores with Nafion[®] and (c) carbon-based electrodes deposition. The magnifications show a circular area of 5 mm diameter.

4.2.1.1 SU-8 porous structure

The SU-8 membrane is composed by two SU-8 layers. The first layer defines an ordered array of square micropores over an area of 5 mm x 5 mm centered in the membrane. The second layer defines a 2.5 mm wide frame around the micropore array. For its fabrication, the first layer of SU-8 50 was spin-coated at 2000 rpm for 35 s to give a thickness of 50 μm . The soft-bake of this layer consisted of a 60 min at 25 $^{\circ}\text{C}$, 6 min at 65 $^{\circ}\text{C}$, 30 min at 95 $^{\circ}\text{C}$ and 10 hours cool-down to 25 $^{\circ}\text{C}$ on a hot-plate using linear ramps between temperatures. The UV-exposure was performed with a MA6/BA6 mask aligner (Karl Süss MicroTec GmbH, Garching, Germany) with a dose of 190 mJ/cm^2 using a printed transparent foil as mask that defined the membrane with the array of micropores. Post-exposure bake consisted of 1 min at 65 $^{\circ}\text{C}$ on a hot-plate followed by 5 min at 95 $^{\circ}\text{C}$ in a convection oven. Then the second SU-8 50 layer was spin-coated at 1000 rpm for 35 s to obtain a layer of 120 μm thickness. The soft-bake of this second layer consisted of 60 min at 25 $^{\circ}\text{C}$, 6 min at 65 $^{\circ}\text{C}$, 60 min at 75 $^{\circ}\text{C}$ and 10 hours cool-down to 25 $^{\circ}\text{C}$ on a hot-plate. The exposure of this layer was performed with a dose of 270 mJ/cm^2 using a mask that defined the frame around the array of micropores in the membrane. Post-exposure bake consisted of 1 min at 65 $^{\circ}\text{C}$ in a hot-plate followed by 12 min at 95 $^{\circ}\text{C}$ in a convection oven. Finally, both layers were simultaneously developed in mr-600 Dev (Micro Resist Technologies GmbH, Berlin, Germany) for 30 min with agitation, then rinsed in 2-propanol and deionized water. To release the developed SU-8 structures from the substrate, the Omnicoat[™] layer was removed by soaking the wafers in developer ma-D 332/S (Micro Resist Technologies GmbH) with agitation. The duration of this step varied from few minutes to several hours depending on the geometrical design of SU-8 structure. Figure 4.3a shows a picture and cross-sectional view of the fabricated SU-8 porous membrane.

4.2.1.2 Nafion[®]-filled SU-8 membranes

In order to provide the SU-8 membranes with the required proton conductivity, their microperforations were filled with a liquid solution of proton exchange polymer (in this case, Nafion[®] perfluorinated resin solution 20 wt. % in lower aliphatic alcohols and water from Sigma-Aldrich, St. Louis, USA) that solidified after solvent evaporation. Figure 4.3b shows a picture and cross-sectional view of the Nafion[®]-filled SU-8 porous membrane. The empty cavities of both SU-8 layers (50 μm -thick grid and 120 μm -thick frame) were filled using a micropipette with solution volumes of 20-25 μl depending on the membrane design. The squared frame defined by the second lithography level served as a reservoir of Nafion[®] solution during filling and the subsequent solvent evaporation. In this way the Nafion[®] could be limited to the desired area, avoiding any dripping or spoiling, and the content in each membrane was accurately controlled. Figure 4.4 shows optical microscope images of the three SU-8 membranes filled with Nafion[®], where labels A, B and C correspond to the pore separations of 250 μm , 100 μm and 50 μm , respectively.

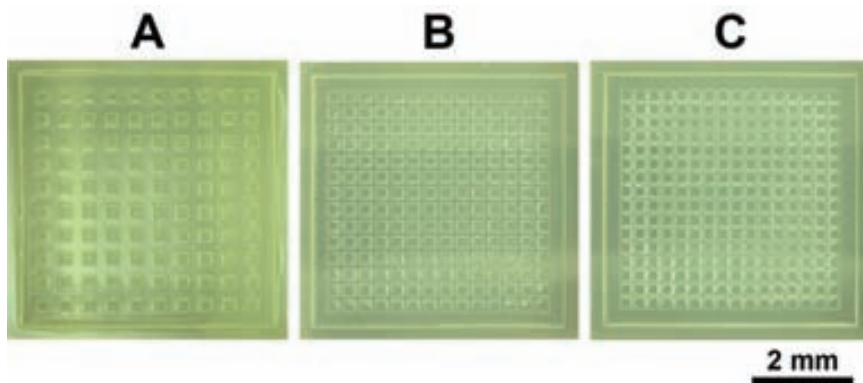


Figure 4.4 Optical microscope images of the three Nafion[®]-filled SU-8 membrane designs.

The proton-conductive capabilities of the Nafion[®]-filled SU-8 membranes were evaluated by electrochemical impedance spectroscopy (EIS). As the Nafion[®] resin solution used to fill the membranes was supplied in H⁺ form, it was not necessary to activate the membranes prior to the measurement. Therefore the membranes were only hydrated soaking them in deionized water at 80 °C for 3 h inside a custom made support that prevented the SU-8 structure of being deformed by the temperature. The setup used to obtain the measurements consisted of a symmetrical electrochemical cell where the membranes were placed between two Pt thin plates. EIS measurements were performed using an Impedance/Gain-Phase Analyzer (SI 1260, Solartron Analytical, Farnborough, UK) in the frequency range from 0.1 Hz to 1 MHz and small ac voltage amplitude in the range between 25-100 mV at room temperature in water saturated ambient air (R.H.=100%). Impedance spectra were acquired and analyzed with ZPlot and ZView software (Scribner Associates Inc., Southern Pines, USA). Before measuring the membrane conductivity, the electrodes of the cell were short-circuited in order to determine the contact resistance. This

series resistance was considered as an offset for the cell measurements. Figure 4.5 shows the Nyquist plot of the EIS measurements obtained from the different types of membrane. The insert shows a detail of the high-frequency range of impedance. Proton conductivity values of the membranes were calculated following the analysis procedure described in section 3.3.2. Table 4.1 shows a summary of the main characteristics of the membranes and the calculated proton conductivity values.

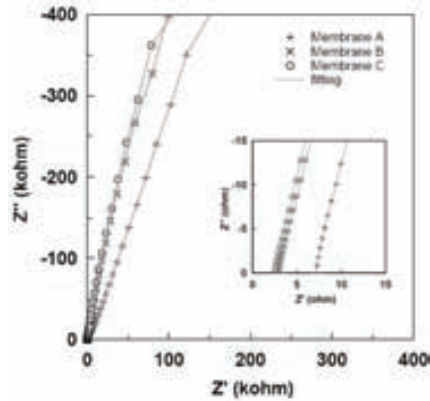


Figure 4.5 Nyquist plot of the EIS measurements for the different Nafion[®]-filled SU-8 membranes at room temperature in air. The insert shows details of high-frequency impedance values.

It can be seen that the obtained proton conductivity of the hybrid membranes (σ_{total}) was 10 ± 1 , 23 ± 1 and 28 ± 1 mS/cm for membranes A, B and C respectively. These values were obtained by considering an effective membrane area of $5 \text{ mm} \times 5 \text{ mm}$ (A_{total}), that is, including the contribution of the non-active SU-8 part of the membrane. Taking into account only the area filled by Nafion[®] polymer, the values of conductivity associated with the electrolyte (σ_{active}) resulted to be very similar between all membranes, with values around 43 ± 2 mS/cm, which is in accordance to the values reported in the literature for continuous Nafion[®] films [10]. These results confirmed the correct operation of the proton-conductive polymer once embedded in the SU-8 porous matrix. The variability found in the value of conductivity for the different supporting matrices could be attributed to slight discrepancies in the real membrane thickness from the $170 \mu\text{m}$ value used for calculations.

After measurements, all the fabricated membranes showed good mechanical stability. No fracture or significant buckling were observed, which proved that the SU-8 matrix was capable of holding the volume expansion of hydrated Nafion[®] without affecting its structure. For that reason, SU-8 membranes with the highest open ratio were used to fabricate the MEAs for the micro fuel cell.

Table 4.1 Summary of membrane parameters and measured proton conductivities.

	Pore size-separation (μm)	A_{active} (cm^2)	$A_{\text{active}}/A_{\text{total}}$	σ_{active} (10^{-3} S/cm)	σ_{total} (10^{-3} S/cm)
Membrane A	250-250	0.0625	0.25	40 ± 2	10 ± 1
Membrane B	250-100	0.1225	0.49	46 ± 2	23 ± 1
Membrane C	250-50	0.1600	0.64	43 ± 2	28 ± 1

4.2.1.3 Carbon-based electrode layers

The deposition of the catalyst was performed by spraying a catalyst ink over the selected membranes using an airbrush like the one shown in Figure 4.6a. In order to define the active area where the catalysts are deposited, four membranes were simultaneously placed between plastic foils from which 5 mm x 5 mm squares were cut out (Figure 4.6b). In this way, the foils acted as a stencil during catalyst spraying and the assembly could be manipulated following the same methodology used for catalyst deposition on a larger scale MEA (Figure 4.6c).

The preparation of the catalyst suspension was made by mixing the catalyst (30 wt.% as Pt on Cabot Vulcan XC72, atomic ratio Pt:Ru 1:1 for the anode and Pt/C 40wt.% for the cathode, Johnson Matthey, London, UK), Nafion[®] ionomer 5 wt.% solution (Aldrich), isopropanol (Merck, Darmstadt, Germany) and Milli-Q water. Nafion[®] content in the ink was 55 wt%. The amount of Nafion[®] in the ink has been optimized to avoid the flooding of the electrodes or the decrease in the performance of the single cell [11, 12]. The suspension was dispersed in an ultrasonic bath for 45 minutes. Then, the ink was sprayed on one side of the membrane and the overall process was repeated to deposit the catalyst on the other side of the membrane. In either case, metal loading was 1.0 mg/cm^2 (being the Pt loading 0.7 mg/cm^2 at the anode and 1 mg/cm^2 at the cathode). After the solvents in the ink were completely evaporated, the MEAs were extracted from the stencil, as shown in Figure 4.6d. A picture and a cross-sectional view of the SU-8 MEA thus obtained are shown in Figure 4.3c.

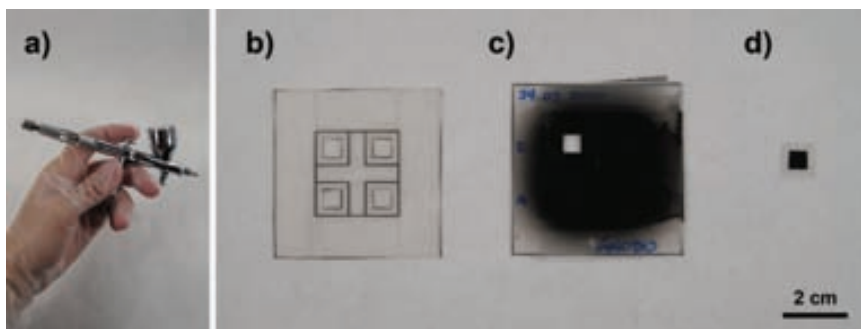


Figure 4.6 (a) Airbrush used for applying the catalyst layers. (b) SU-8 membranes inside the plastic foils used as stencil. (c) Stencil sprayed with catalyst ink and (d) SU-8 MEA extracted from the stencil.

4.2.2 Fabrication of fuel cell current collectors

For the fabrication of the SU-8 current collectors a layer of SU-8 100 was spin-coated over the wafer at 1000 rpm for 35 s to obtain a 250 μm thick layer. The soft-bake consisted of a series of temperature steps performed over a hot plate starting with a 60 min resting period at 25 $^{\circ}\text{C}$, followed by 6 min at 65 $^{\circ}\text{C}$, 90 min at 95 $^{\circ}\text{C}$ and 10 hours cool-down to 25 $^{\circ}\text{C}$. The UV-exposure was performed with a dose of 400 mJ/cm^2 . Post-exposure bake consisted of 1 min at 65 $^{\circ}\text{C}$ in a hot-plate followed by 20 min at 95 $^{\circ}\text{C}$ in a convection oven. Finally, the layer was developed with agitation for 1 hr in mr-600 Dev and then rinsed in 2-propanol and deionized water. The developed SU-8 collectors were released from the substrate removing the Omnicoat™ layer in developer ma-D 332/S with agitation.

In order to provide SU-8 current collectors with electrical conductivity, a bi-layer of 50 nm Ti and 50 nm Ni was deposited on one of their sides by sputtering (MRC-903, MRC Systems, Heidelberg, Germany). A tailored piece of polydimethylsiloxane (PDMS) was placed as a shadow mask onto the current collector to restrain metal deposition to the central 5 mm x 5 mm active area. In this way, the surrounding surface of the active area keeps SU-8 exposed and available to bond directly to the SU-8 MEA by hot-pressing. After this, the PDMS mask was peeled off from the SU-8 structure, leaving the metal layer on the desired places, as shown in Figure 4.7. The sputtered layer was then used as a seed layer for an electrodeposition of 1.5 μm of Ni and a thin layer of Au to prevent oxidation.

The electrical resistivity of the SU-8 current collectors was characterized by 4-probe measurements performed on a test sample with the same metallization but with appropriate dimensions. The sheet resistance of the metal yielded a value of 46.6 $\text{m}\Omega$ per square, which was in accordance to the materials nominal resistance for the thickness deposited.

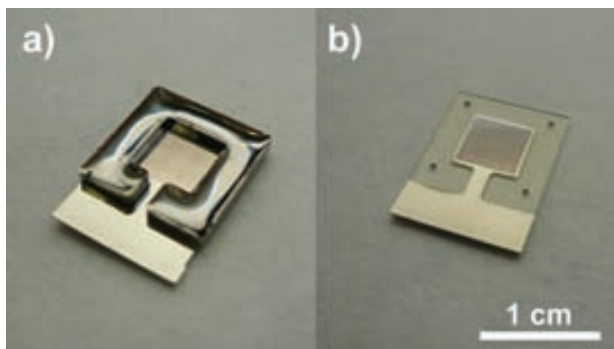


Figure 4.7 Metalized SU-8 current collector by sputtering, before (a) and after (b) removal of PDMS shadow mask.

4.3 MICRO FUEL CELL ASSEMBLY AND CHARACTERIZATION

Once all the components were obtained separately, the micro fuel cell was mounted by aligning two current collectors at both sides of the MEA. Before proceeding to the thermal bonding of all these SU-8 components, a preliminary test of the SU-8 fuel cell was performed using the same external casing that was developed for the silicon micro fuel described in Chapter 2.

The polarization curve of the micro fuel cell was obtained galvanostatically with a Keithley 2400 Sourcemeter (Keithley, Cleveland, USA) using an in-house LabVIEW (National Instruments, Austin, USA) program. Characterization was done with methanol concentrations of 2M and 4M (chosen because these values lie within the concentration range that yields optimal fuel cell performance in passive devices as shown in previous chapters), and at temperatures of 22 °C (room temperature) and 40 °C. Figure 4.8 shows the polarization curves obtained with this assembly.

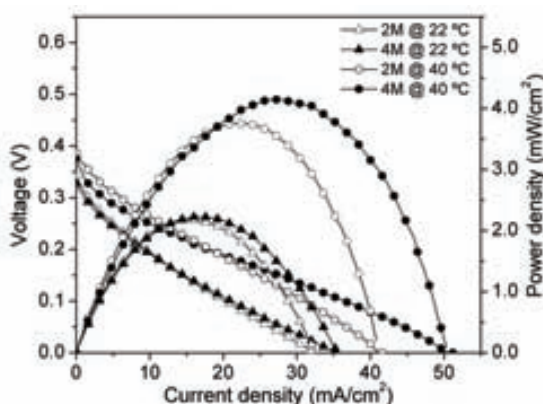


Figure 4.8 Polarization curves of SU-8 micro fuel cell with the external casing operating on 2M and 4M methanol concentrations at two temperatures.

It can be seen that at room temperature (22 °C), the micro fuel cell achieves a maximum power density of 2.20 mW/cm² regardless of the methanol concentration. No significant differences in the open circuit voltage (OCV) are observed due to methanol crossover and the I-V curves are mainly controlled by ohmic losses. When increasing cell temperature to 40°C, maximum power densities rise to 3.75 mW/cm² and 4.15 mW/cm² at fuel concentrations of 2M and 4M respectively. This is mainly due to the improvement of micro fuel cell performance in the ohmic region due to the enhancement in the Nafion[®] proton conductivity at increasing temperatures. This time, a visible improvement in the transport-limited region of the I-V curve can be observed when raising the methanol concentration from 2M to 4M.

After this test, the SU-8 structures were bonded against each other by a hot-pressing process to obtain the compact device. A dedicated support was fabricated to align and press together the current collectors and the MEA as shown in Figure 4.9a. This accessory consisted of two aluminum parts with a Teflon piece that incorporates four needles and a PDMS slab to compensate the height of the SU-8 structures. Alignment was done by inserting the needles through the small circular holes placed at the corners of SU-8 components. The assembly was then placed in a commercial hot-press (P/O/Weber, Remshalden, Germany) and heated to 85 °C for 10 min and 120 °C with a force of 2 kN for 20 min (Figure 4.9b). After this, the assembly was cooled down by natural convection and the bonded SU-8 micro fuel cell was released for testing.

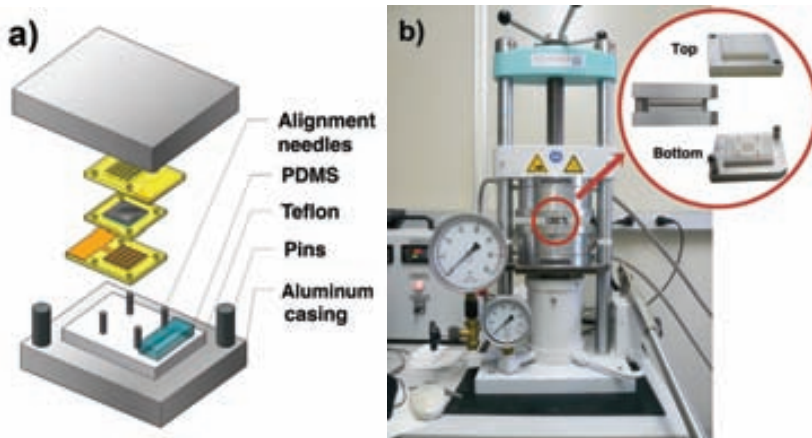


Figure 4.9 (a) Diagram of the support fabricated for bonding the SU-8 components of the fuel cell. (b) Bonding of SU-8 micro fuel cell inside the hot-press.

With this assembly, the total volume of the device is reduced more than 50 times (0.12 cm^3 respect to 6.75 cm^3). Figures 4.10a and 4.10b show photographs of the two assemblies tested, and a side view of the compact device where the significant size reduction between both approaches is clearly seen.

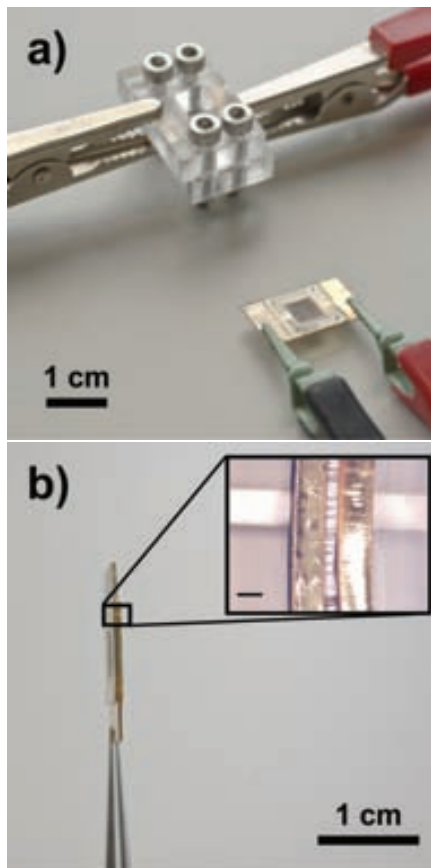


Figure 4.10 (a) Picture of the two micro fuel cell assemblies during characterization. (b) Side view of the SU-8 micro fuel cell (the scale bar in the inset corresponds to 200 μm).

Characterization was done under the same conditions as with the previous setup. Figure 4.11 shows the polarization curves obtained. After bonding, all curves present higher voltage values at open circuit conditions (500-580 mV) followed by a sudden voltage drop due to activation losses. After that, curves are mainly controlled by ohmic losses, showing no limitations in the mass transport region. In this case, the micro fuel cell yielded a very similar maximum power density at both tested methanol concentrations and working temperatures. At 2M concentration, a temperature increase from 22 $^{\circ}\text{C}$ to 40 $^{\circ}\text{C}$ raised the power density from 0.35 to 0.55 mW/cm^2 , whereas at 4M raised it from 0.40 to 0.65 mW/cm^2 .

Results show a clear difference in the power delivered by the SU-8 micro fuel cell depending on the assembly setup. When tightened with an external acrylic casing, the maximum power of 4.15 mW/cm^2 obtained at $40 \text{ }^\circ\text{C}$ and 4M methanol concentration is comparable to results reported in the literature for other microDMFC partially fabricated with SU-8 components [12, 13]. It is important to notice that unlike those used in previous works, the present approach reduces both device complexity and cost by using a diffusion-driven feeding of methanol and air and minimizing the amount of Pt catalyst to 1 mg/cm^2 . Moreover, the continuous Nafion[®] film typically used in other approaches has been substituted here by a Nafion[®]-filled porous SU-8 membrane. The use of the membrane clearly enhances the level of integration of the final device, although it reduces the available proton conductive area by a 36%.

When bonded together in a compact device, the maximum power density yielded by the SU-8 fuel cell decreases to 0.65 mW/cm^2 . This is due to an increase of voltage losses in the ohmic region of the polarization curves. It can be seen that curves from Figure 4.11 present the same slope regardless of temperature and methanol concentration, which indicates the existence of a significant contact resistance between the membrane and the current collectors. That is, even though the SU-8 components have been satisfactorily bonded and no fuel leakage has been observed, the pressure applied between them is lower than the one exerted by the external casing. Nevertheless, despite the decrease in its performance, the drastic reduction of the device dimensions achieved with this approach results in a substantial enhancement of volumetric power density from 0.15 mW/cm^3 using the external casing up to 1.35 mW/cm^3 in the compact approach.

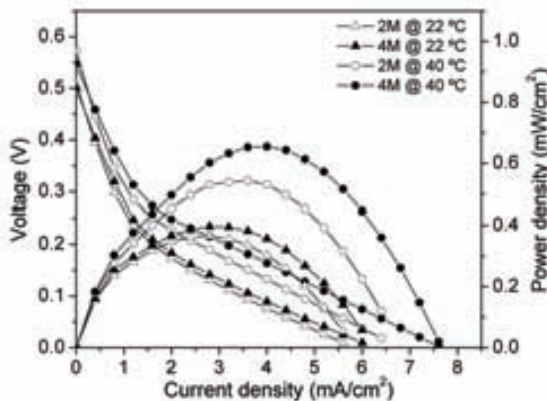


Figure 4.11 Polarization curves of the compact SU-8 micro fuel cell operating on 2M and 4M methanol concentrations at two temperatures.

4.4 DISCUSSION AND SUMMARY

In this chapter a novel approach to an all-polymer micro fuel cell based on SU-8 photoresist has been presented. All fuel cell components (current collectors and MEA) are fabricated with the same material, whose bonding capabilities are exploited to obtain a highly compact device. The integration is achieved in two steps; first, by the embedding of a polymeric electrolyte into a porous SU-8 membrane and second by bonding all SU-8 components together.

The micro fuel cell has been first characterized using an external casing to validate the functionality of its components. Despite the simplicity associated to the passive delivery of the fuel and the low catalyst content, the performance of the present micro fuel cell is comparable to the few polymeric devices reported to date. After validation, all components were bonded together by hot-pressing in order to obtain the compact device. Characterization of the assembly showed a decrease in power density due to an increase in contact resistance. However, the drastic reduction of the device dimensions when dispensing with the external frame resulted in a larger volumetric power density.

Further work will be directed to device optimization through the reduction of ohmic losses. In this sense, different strategies arise, such as modification of the SU-8 structures that allow an increase of device robustness after thermal bonding; alternative MEA fabrication by substituting the carbon-based electrodes by a thinner catalyst layers (sputtering, electrodeposition, carbon nanotube incorporation); and the development of planar architectures in which pressure between components is not a key factor.

Nevertheless, the results presented demonstrate the potential of this approach to obtain a fully-polymeric power source. They benefit from the advantages associated to SU-8 technology (e.g. high chemical and mechanical stability of structures, high resolution of patterns, low cost). Moreover, the use of this technology offers additional opportunities for integration of micro fuel cell within a wide variety of polymeric devices such as lab-on-chip and other microfluidic platforms.

References in Chapter 4

- [1] Fiorini G. S. and Chiu D. T. Disposable microfluidic devices: fabrication, function, and application *BioTechniques* **38** (2005) 18
- [2] Shah K., Shin W. C. and Besser R. S. A PDMS micro proton exchange membrane fuel cell by conventional and non-conventional microfabrication techniques *Sensors and Actuators B: Chemical* **97** (2004) 157-67
- [3] Chan S. H., Nguyen N. T., Xia Z. T. and Wu Z. G. Development of a polymeric micro fuel cell containing laser-micromachined flow channels *Journal of Micromechanics and Microengineering* **15** (2005) 231-6
- [4] Campo A. d. and Greiner C. SU-8: a photoresist for high-aspect-ratio and 3D submicron lithography *Journal of Micromechanics and Microengineering* **17** (2007) R81
- [5] Hsieh S. S., Kuo J. K., Hwang C. F. and Tsai H. H. A novel design and microfabrication for a micro PEMFC *Microsystem Technologies* **10** (2004) 121-6
- [6] Cha H.-Y., Choi H.-G., Nam J.-D., Lee Y., Cho S. M., Lee E.-S., Lee J.-K. and Chung C.-H. Fabrication of all-polymer micro-DMFCs using UV-sensitive photoresist *Electrochimica Acta* **50** (2004) 795-9
- [7] Weinmueller C., Tautschnig G., Hotz N. and Poulidakos D. A flexible direct methanol micro-fuel cell based on a metalized, photosensitive polymer film *Journal of Power Sources* **195** (2010) 3849-57
- [8] Esquivel J. P., Sabaté N., Santander J., Torres-Herrero N., Gràcia I., Ivanov P., Fonseca L. and Cané C. Influence of current collectors design on the performance of a silicon-based passive micro direct methanol fuel cell *Journal of Power Sources* **194** (2009) 391-6
- [9] Blanco F. J., Agirregabiria M., Garcia J., Berganzo J., Tijero M., Arroyo M. T., Ruano J. M., Aramburu I. and Mayora K. Novel three-dimensional embedded SU-8 microchannels fabricated using a low temperature full wafer adhesive bonding *Journal of Micromechanics and Microengineering* **14** (2004) 1047
- [10] Neburchilov V., Martin J., Wang H. and Zhang J. A review of polymer electrolyte membranes for direct methanol fuel cells *Journal of Power Sources* **169** (2007) 221-38
- [11] Ihonen J., Jaouen F., Lindbergh G., Lundblad A. and Sundholm G. Investigation of Mass-Transport Limitations in the Solid Polymer Fuel Cell Cathode *Journal of The Electrochemical Society* **149** (2002) A448-A54
- [12] Sasikumar G., Ihm J. W. and Ryu H. Optimum Nafion content in PEM fuel cell electrodes *Electrochimica Acta* **50** (2004) 601-5

5. Fuel delivery system for liquid-fed micro fuel cell

As it has been described and measured in previous chapters, the voltage of a fuel cell is limited to the electrochemical reaction and the losses associated to its assembly and operation. The magnitude of the voltage obtained from a single fuel cell during its operation (0.2-0.3 V) is usually too small to power an electronic device. For this reason, fuel cells are usually connected in series in order to produce a useful voltage. Such configuration is known as a 'stack'. One of the most implemented methods for building stacks consists in the use of bipolar plates as current collectors to interconnect the different fuel cells and deliver the reactants to the reaction sites. This method can efficiently be implemented in active fuel cells, in which the flow rates of reactants can be adjusted to control their concentration in the system and remove continuously the produced by-products. In contrast, passive fuel cells are more likely to be negatively affected by the accumulation of by-products due to its diffusion-based mass transport, e.g. when the concentration of the carbon dioxide generated in a direct methanol fuel cell exceeds a certain level, the performance of the system is deteriorated because of reaction sites blockage and mass transport difficulties [1, 2]. It is for this reason that in passive fuel cells, a suitable management of the chemical species involved is indispensable in stack configurations for ensuring the device operation.

Solutions regarding the passive delivery of liquid fuel and management of produced CO₂ in fuel cells have been proposed. Some of these works are based in the incorporation of a permeable material in contact with the anode compartment that keeps the concentration of fuel within an operative range by a capillary wicking effect [3-7]. Other approaches base their operation on the tapered design of microchannels and anode chambers that allow the recirculation of fuel and removal of CO₂ bubbles by capillary pressure [8-10]. However, the integration of these concepts for the assembly of micro fuel cell stacks has not yet been addressed.

This work proposes a complementary microfluidic system that could be attached to the anode side of the fuel cell to supply the liquid fuel and facilitate the exit of the gas by-products in a passive way. The device represents an attractive solution to the assembly of vertical fuel cell stacks with passive fuel delivery, distributing the fuel and expelling the gas by-products in a transversal plane with respect to the active area.

The device was fabricated in a polymeric material using an original fabrication method developed for this application in collaboration with the Operator Centre of Microtechnology (AZM) at the Helmholtz Zentrum Berlin. The process is based on the combination of several micropatterning techniques that permits the accurate

replication of multilevel polymeric components [11-13]. In this way, the fuel delivery component performs the fluids management by the modification of the surface topography without using any additional chemical treatment. In this case the multilevel structures were designed to restrain the liquid fuel inside the anode active area while allowing the degassing of CO_2 .

The detailed fabrication process, microfluidic operation and characterization methodology of the fuel delivery system are explained in the next sections. The operation of the device was tested using a hybrid micro direct methanol fuel cell.

5.1 DEVICE DESIGN

The fuel delivery system proposed in this work consists of a polymeric component that can be incorporated onto the direct methanol micro fuel cell to distribute the fuel and retain it in the active area while allowing the exhaustion of CO_2 produced during the fuel cell operation. Figure 5.1 presents the concept of the designed component.

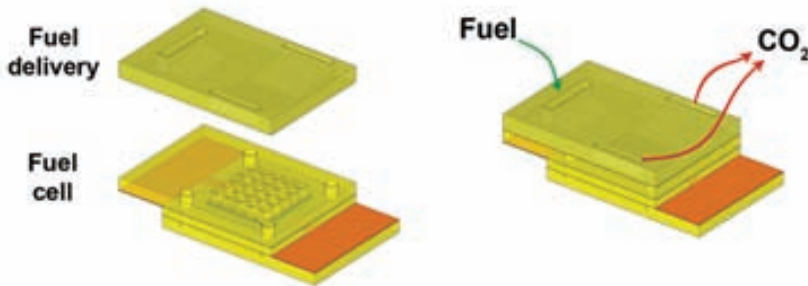


Figure 5.1 Design of passive fuel delivery system that can be integrated on a micro fuel cell.

Once the component is placed on top of a micro fuel cell, the fuel is supplied through an inlet slot that connects to a wide channel, leading the liquid to a tapered chamber positioned over the active area of the fuel cell. The inclinations of the chamber lead the produced gas towards outlet slots at the sides of the component.

The last part of the chamber surface, before the outlets, has been provided with nanostructures. This patterning creates a hydrophilic-hydrophobic junction in this part of the channel, which retains the liquid fuel and lets the gases out [22]. A diagram of the fuel delivery component indicating its different features is shown in Figure 5.2.

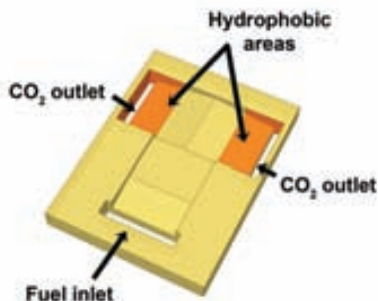


Figure 5.2 Diagram of the fuel delivery component indicating its main features. The modification of the wetting properties is achieved by patterning the device surface.

The fabrication process used in this work allows obtaining micro-nanostructured components made of a photosensitive epoxy resin that is capable of bonding to SU-8 structures by a hot-pressing process. This capability was used to fabricate the polymeric fluidic component with tailored wetting properties and incorporate it over one of the SU-8 current collectors presented in the previous chapter.

For this application a difference in the wetting properties of the device surface were obtained by selectively structuring the surface, combining hydrophobic and hydrophilic areas for a passive fluid distribution. The wetting properties of a solid surface depend on several factors, such as the material composition, the kind of liquid substance that is put in contact with and the surface morphology [14-19]. As for this last one, the size and shape of the structures in the substrate determine the interaction with a liquid. Many studies have been reported about the influence of the surface roughness and micro-nanostructure shape to achieve superhydrophobicity (Lotus effect) [17, 20, 21]. In this work, the effect of different structure dimensions in the hydrophobicity of the material was evaluated and the structures showing the highest effect were implemented in the final device design.

5.2 FABRICATION PROCESS

The fabrication process of the fuel delivery component was based on a replica molding technique. This process allowed the replication of multilevel structures with nanometer resolution in a photosensitive epoxy resin. For this purpose, a master containing the patterns to be replicated was obtained following these general steps: (1) fabrication of a machined substrate by micromilling; (2) structuring of a plastic foil with micropillars; (3) fabrication of three-dimensional master by thermoforming of the structured foil onto the substrate. A generic representation of the process steps is depicted in Figure 5.3.

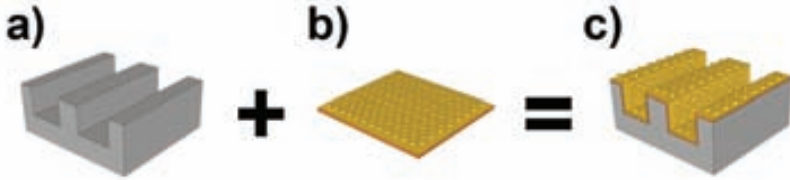


Figure 5.3 (a) Micromilled substrate and (b) structured plastic foil used for obtaining the (c) three-dimensional master by a thermoforming process.

The fabrication of the substrate was done in a PFM 24 mediMill 4-axis milling machine (PRIMACON Maschinenbau GmbH) using mills with diameters of 200 μm for all the device patterning and 1 mm for defining the frame around the device. A brass blank with a diameter of 50 mm and a thickness of 3 mm was used as a substrate. This step defined the shape and dimensions of the device (10.0 x 14.0 x 1.6 mm), the inlet and outlets and the tapered chamber. The inclination in the inlet channel was set to 17° while the chamber had an angle of 14°. This shape facilitated the entrance of the fluid and the exhaustion of gases. Figure 5.4 shows a picture of the micromilled substrate.

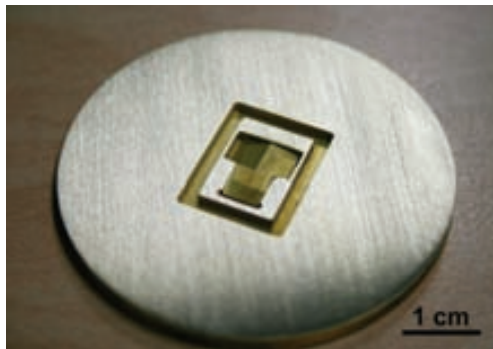


Figure 5.4 Micromilled brass substrate defining the fuel delivery shape and dimensions.

The structures used to define the hydrophobic effect in the fuel delivery structure were defined on a thermoplastic foil by UV-Nanoimprint Lithography (UV-NIL) (Figure 5.5). In order to perform this step, a stamp of PDMS (Elastosil 601 Wacker) was needed. The stamp was fabricated by casting a silicon master with arrays of micropillars defined by RIE (Figure 5.5b). This type of PDMS is especially suitable as a stamp material for UV applications because of its relatively low absorption of light at a wavelength of 365 nm.

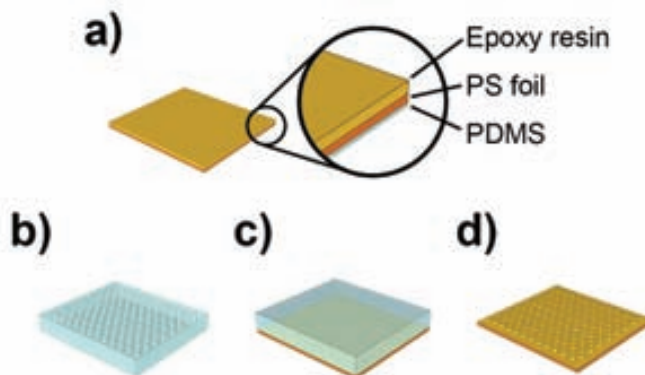


Figure 5.5 Fabrication process used for obtaining the structured polymer foil.

The thermoplastic foil (shown in Figure 5.5a) was prepared by spin coating a PDMS layer on a 50 μm -thick polystyrene (PS) foil. The PDMS was spun at 5000 rpm to obtain a thickness of 10 μm and then it was cured at 70 $^{\circ}\text{C}$ for 30 min. After this, the photosensitive epoxy was spin coated at 2000 rpm over the other side of the thermoplastic foil to obtain a thickness of 10 μm . This material was composed of a mixture of bis-cycloaliphatic epoxide (BCE), 20 wt% divinylether of triethylene glycol (DVE-TEG) and 3 wt% of triaryl sulfonium salt (TAS) as photoinitiator (Sigma-Aldrich). In this case, the addition of ether was necessary to achieve a good sticking of the epoxy layer, as it partially dissolves the foil, leading to a better stability during the thermoforming process. Otherwise, the epoxy layer would peel off from the foil when temperature and pressure are applied. The UV-NIL was done placing the PDMS stamp over the foil, filling its cavities with the liquid UV curing material, and exposing with a dose of 360 mJ/cm^2 (Figure 5.5c). After exposure of the epoxy resin, the PDMS stamp was removed; obtaining the structured foil (Figure 5.5d).

In order to determine the structure size that results in the highest hydrophobicity, contact angle measurements were performed on different structured resin substrates. The measured structures consisted of 6 μm -high pillars with diameters of 800 nm, 1.6 μm , 3.2 μm and 6.4 μm . The contact angle measurements were performed with an EASY-Drop-Standard equipment from Krüss GmbH. The measurements were realized with a 2M solution of methanol. A detailed description of the procedure followed to perform the contact angle measurement can be found in [20, 23]. The results of the contact angle measurements are summarized in Figure 5.6, where the mean values of the measured equilibrium angles are plotted. A measurement of the plain (unstructured) sample was also measured for comparison. As it can be seen, the measured values of contact angle increase significantly with the surface structuring. The contact angle value of the plain sample was 95 $^{\circ}$ and increased to 153 $^{\circ}$ with the structures of 800 nm diameter. From this point, the contact angle decreased for larger diameters, until a value of 125 $^{\circ}$ with the pillars of 6.4 μm diameter. As the application requires the maximum hydrophobicity, the structures of 800 nm pillars were chosen. The inset in the figure shows a picture of the liquid drop on the 800 nm structured substrate.

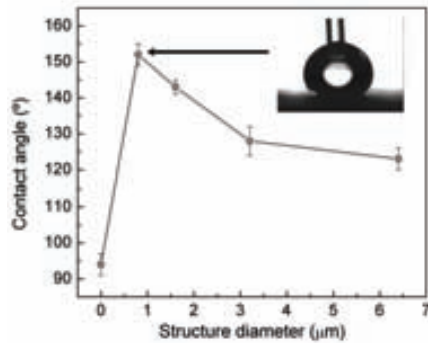


Figure 5.6 Contact angle measurement values obtained from the structured surface of replicated resin and liquid drop on a structured substrate with 800 nm pillars.

Once the micromilled substrate and the structured polymer were fabricated, the 3D master was obtained. The thermoforming of the structured foil over the machined substrate was done using an adapted tool mounted into a HEX03 Hot-Embossing Machine from Jenoptik. First, the foil was aligned against the substrate to place the microstructured areas over the desired surface. The assembly was heated up to 115 °C, a value above the glass transition temperature ($T_g = 80$ °C) of the foil. Then a force of 15 kN was applied over the foil to improve the thermal contact. During the heating cycle, a vacuum pressure was applied to the lower part of the tool to achieve a good molding quality during the thermoforming process. Once the whole assembly heated up, a pressure of 30 bar was applied in the upper part of the tool using compressed N_2 . Due to the pressure difference between lower and upper part of the tool, the structured foil covered the micromilled brass substrate, obtaining a 3D master (Figure 5.7a). After this, the assembly was cooled down and the tool was vented.

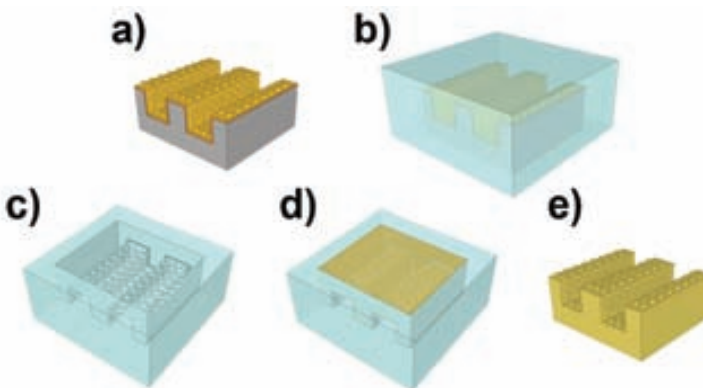


Figure 5.7 Fabrication process used for obtaining a three-dimensional epoxy resin component.

The 3D master was then transferred to PDMS by soft-lithography (Figure 5.7b). The PDMS prepolymer was mixed according to the manufacturer's specification, degassed for 5 min to avoid air bubbles. Then it was casted into the ring of the thermoforming tool. No additional treatment of the 3D master was necessary for detaching after curing. The frame was covered with a metal plate, which was kept in touch with the PDMS mixture to define a flat surface on the back of the stamp and the assembly was pressed with a force of 3 kN and heated up to 70 °C for 30 min for the curing process. After curing, the PDMS stamp was peeled off from the master (Figure 5.7c).

The PDMS stamp was then used to replicate the fuel delivery component in epoxy resin (Figure 5.7d). The epoxy resin was composed of a mixture of diglycidyl ether of bis-phenol A (DGE-BPA) and 3 wt% of triaryl sulfonium salt (TAS) as a photoinitiator. To achieve a lower viscosity, the mixture was heated up to 70 °C [13]. This mixture was casted onto the PDMS stamp, and then a thin foil of polycarbonate was placed over it to ensure a plain back surface of the replication. The exposure was realized with a dose of 1200 mJ/cm². The cured structured part could be easily peeled off the PDMS stamp and released from the polycarbonate foil (Figure 5.7e). The complete opening of the inlet and outlet slots was easily achieved during the device de-molding. A photograph of the released device is shown in Figure 5.8. SEM images from different sections of the device can be seen in Figure 5.9, showing the hydrophobic zones with the 800 nm pillars on the surface. The accuracy of the replication was satisfactory for all patterns in the device.

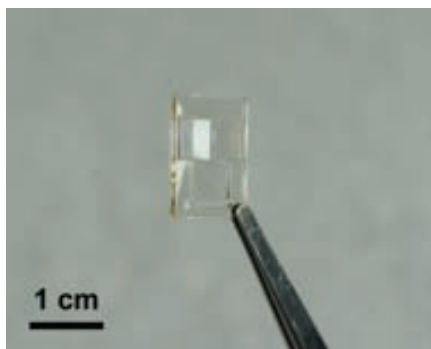


Figure 5.8 Photograph of the replicated microfluidic device.

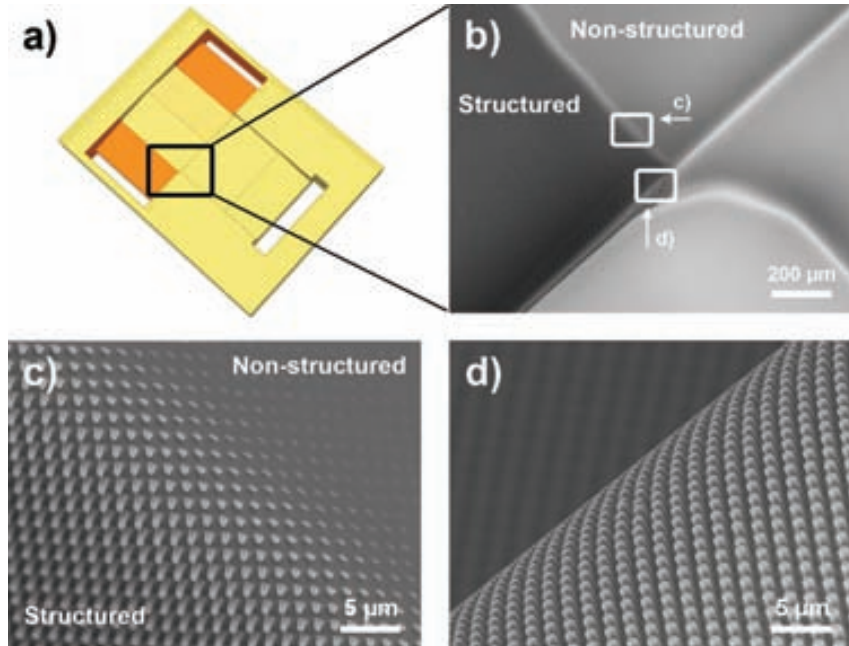


Figure 5.9 SEM images of the fuel delivery component at different magnifications showing the microstructured areas.

5.3 FLUIDIC CHARACTERIZATION

The replicated microfluidic devices were bonded to one of the SU-8 current collectors using the method described in Chapter 4. This allowed to have closed channels and chamber for the fluidic characterization of the device and also proved the compatibility of both materials for a straightforward integration onto the SU-8 micro fuel cell. The measurements were performed under a microscope using a 2M methanol solution.

The testing was performed by dispensing a drop of the liquid solution through the device inlet. It could be observed that the liquid solution flowed through the entrance to the device chamber. The solution filled the entire hydrophilic area but stopped at the border of the outlet channels where the hydrophobic structures begin. Figure 5.10 shows a sequence of photographs of the device filling with the liquid fuel. It could be seen that even though the large capillary force formed in closed cavities of these dimensions, the fluid is contained in the desired area. The fluid profile creates a sharp edge in line with the hydrophobic structures. In this case the hydrophobic effect is sufficient to withstand the advance of the fluid. This test was performed several times to evaluate the repeatability of the system, leaving the liquid in the device until it was evaporated and then filling it again.

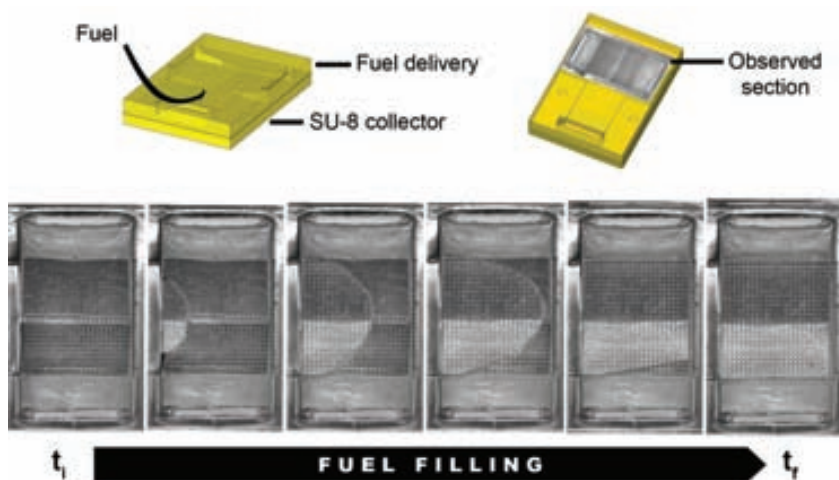


Figure 5.10 Picture sequence of the fuel delivery filling with the liquid fuel.

After these tests, the operation of the fuel delivery system was evaluated using the hybrid methanol micro fuel cell presented in Chapter 2. This system was chosen to perform the characterization because it produces the highest output current among the micro fuel cell approaches developed in this work. In this way, the response of the fuel delivery component could be evaluated at a higher fuel consumption regime. The fuel delivery component was placed over the anode current collector and the whole assembly was pressed between methacrylate pieces. Figure 5.11 shows a picture of the assembly during characterization, it could be seen that the methanol only filled the active area stopping at the hydrophobic surface of the outlets. The system was fed with 100 μL of methanol with a concentration of 2M. The fuel cell current output was fixed to 10 mA and the voltage was recorded until the methanol consumed. Figure 5.12 shows the long-term operation of the system compared to the response of the hybrid microDMFC without the fuel delivery component.

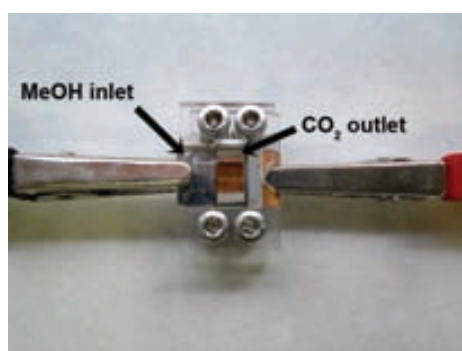


Figure 5.11 Assembly of fuel delivery component on a hybrid micro direct methanol fuel cell.

It can be seen that the performance of the fuel cell using the fuel delivery component is comparable to the obtained with the μ DMFC alone. This test corroborates that the fuel delivery system is capable of distributing the fuel to the active area of the fuel cell and evacuate the produced CO_2 during the fuel cell operation without compromising its performance.

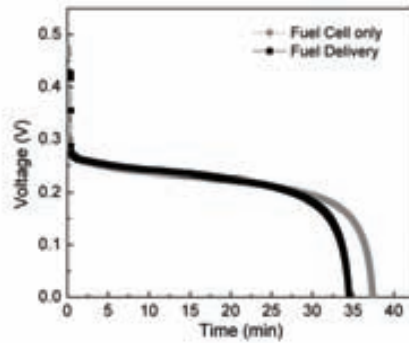


Figure 5.12 Long-term operation of a hybrid micro direct methanol fuel cell operating at 10 mA with and without a fuel delivery component.

5.4 DISCUSSION AND SUMMARY

A fuel delivery component to incorporate onto a micro fuel cell and facilitate the management of species in a passive way was fabricated. In this microfluidic component, hydrophobic areas were created by topographic modification of the surface using different polymer micropatterning techniques as a way to optimize the device dimensions and reduce materials and production cost. In this way, the presented development would allow the fabrication of fuel cell stacks with a passive fuel supply.

An SU-8 cover was bonded to the device for fluidic characterization with a methanol solution showing the possibility to integrate this component into the polymeric micro fuel cell described previously in this work. The results have shown that when the device is filled with fuel, the solution is restrained to the hydrophilic areas while the CO₂ produced in the fuel cell reaction is efficiently exhausted.

The fabrication method developed for this application can be used for structuring of foils and polymeric parts for a variety of microfluidic devices. Besides, the possibility of 3D structuring offers the realization of complete new devices in other fields.

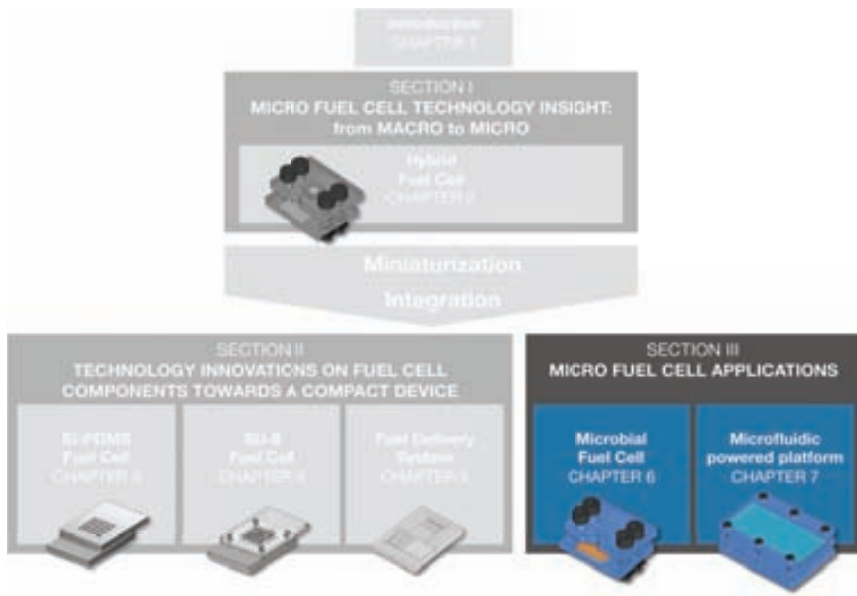
References in Chapter 5.

- [1] De Bruijn F.A., Papageorgopoulos D.C., Sitters E.F. and Janssen G.J.M. The influence of carbon dioxide on PEM fuel cell anodes *Journal of Power Sources* **110** (2002) 117-24
- [2] Yan W.-M., Chu H.-S., Lu M.-X., Weng F.-B., Jung G.-B. and Lee C.-Y. Degradation of proton exchange membrane fuel cells due to CO and CO₂ poisoning *Journal of Power Sources* **188** (2009) 141-7
- [3] Guo Z. and Faghri A. Miniature DMFCs with passive thermal-fluids management system *Journal of Power Sources* **160** (2006) 1142-55
- [4] Chen Y., Melvin Iii L.S., Weislogel M.M., Jenson R.M., Dhuey S. and Nealey P.F. Design, fabrication, and testing of microporous wicking structure *Microelectronic Engineering* **85** (2008) 1027-30
- [5] Fabian T., O'hayre R., Litster S., Prinz F.B. and Santiago J.G. Passive water management at the cathode of a planar air-breathing proton exchange membrane fuel cell *Journal of Power Sources* **195** (2010) 3201-6
- [6] Guo Z. and Cao Y. A passive fuel delivery system for portable direct methanol fuel cells *Journal of Power Sources* **132** (2004) 86-91
- [7] Kamitani A., Morishita S., Kotaki H. and Arscott S. Improved fuel use efficiency in microchannel direct methanol fuel cells using a hydrophilic macroporous layer *Journal of Power Sources* **187** (2009) 148-55
- [8] Metz T., Paust N., Müller C., Zengerle R. and Koltay P. Passive water removal in fuel cells by capillary droplet actuation *Sensors and Actuators A: Physical* **143** (2008) 49-57
- [9] Paust N., Krumbholz S., Munt S., Müller C., Koltay P., Zengerle R. and Ziegler C. Self-regulating passive fuel supply for small direct methanol fuel cells operating in all orientations *Journal of Power Sources* **192** (2009) 442-50
- [10] Litterst C. Passive Fluid Management in Micro Direct Methanol Fuel Cells. In: *Technischen Fakultät*, 2010 (Freiburg: Albert-Ludwigs Universität Freiburg im Breisgau)
- [11] Senn T., Esquivel J.P., Lörger M., Sabate N. and Löchel B. Replica molding for multilevel micro-/nanostructure replication *Journal of Micromechanics and Microengineering* **20** (2010) 115012
- [12] Senn T., Waberski C., Wolf J., Esquivel J.P., Sabaté N. and Löchel B. 3D structuring of polymer parts using thermoforming processes *Microelectronic Engineering* **88** (2011) 11-6
- [13] Senn T., Müller C. and Reinecke H. Replication of HARMST and large area nanostructured parts using UV cationic polymerization *Journal of Micromechanics and Microengineering* **20** (2010) 075002
- [14] Feng J, Huang B and Zhong M Fabrication of superhydrophobic and heat-insulating antimony doped tin oxide polyurethane films by cast replica micromolding *J. Colloid Interface Sci.* **336** (2009) 268
- [15] Kim D S, Lee B-K, Yeo J, Coi M J, Yang W and Kwon T H Fabrication of PDMS micro/nano hybrid surface for increasing hydrophobicity *Microelectron. Eng.* **86** (2009) 1375
- [16] Singh R A, Yoon E-S, Kim H J, Kim J, E J.H. and Y S.K. Replication of surfaces of natural leaves for enhanced micro scale tribological property *Mater. Sci. Eng.* **27** (2007) 875
- [17] Jeong H E, Kwak M K, I P.C. and Y S.K. Wettability of nanoengineered dual-roughness surfaces fabricated by UV-assisted force lithography *J. Colloid Interface Sci.* **339** (2009) 202
- [18] Park C I, Jeong H E, Lee S H, Cho H S and Suh H Y Wetting transition and optimal design for microstructured surfaces with hydrophobic and hydrophilic materials *J. Colloid Interface Sci.* **336** (2009) 298
- [19] Gadegaard N, Martinez E, Riehle M O, K S. and Wilkinson C D W Applications of nano-patterning to tissue engineering *Microelectron. Eng.* **83** (2006) 1577

- [20] Mertsch O, Schondelmaier D, Rudolph I, Kutz O, Walter Antje D, Schleunitz A, Kouba J, Waberski Ch and B L. Generation and characterization of super-hydrophobic micro- and nano-structured surfaces *J. Adhes. Sci. Technol.* **22** (2008) 1967
- [21] Cassie A.B.D. and Baxter S. Wettability of porous surfaces *Trans. Faraday Soc.* **40** (1944) 546
- [22] Meng D.D. and Kim C.J. An active micro-direct methanol fuel cell with self-circulation of fuel and built-in removal of CO₂ bubbles *Journal of Power Sources* **194** (2009) 445-50
- [23] Mertsch O. Nanoporöse und ultra-hydrophobe Strukturen im Negativresist SU8. 2008 (Berlin: Technische Universität Berlin)

SECTION III

MICRO FUEL CELL APPLICATIONS



6. Microfabricated Microbial Fuel Cell

A microbial fuel cell (MFC) is a device capable of converting the chemical energy from organic compounds, such as simple carbohydrates or organic waste matter, into electricity by using bacteria as biocatalysts [1-6]. This type of fuel cell has several advantages, such as a high efficiency due to the direct conversion of the fuel energy into electricity, room temperature operation, absence of toxic by-products and the ability to use a great diversity of low cost organic compounds depending on the metabolic abilities of the organisms being used [2].

Microbial fuel cells have gained much attention because their combined potential as power sources as well as their wastewater treating capacity. Furthermore, MFCs have been proposed in the past as biosensors for measuring environmental parameters such as biochemical oxygen demand and water toxicity [7-12].

Miniaturization of MFCs have been previously reported as potential portable sources and also as platforms for studying the different variables influencing their performance in a controlled and time efficient way. These works report devices built on a variety of materials, using graphite felt, reticulated vitreous carbon or metallic electrodes [13-15]. Regarding silicon-based configurations, only a few works have been reported [16].

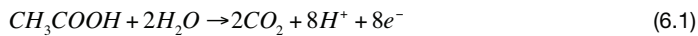
In this chapter, the development of a microfabricated microbial fuel cell is presented. The operation principle of this kind of bio fuel cell, description of the developed system, its operation performance and the impact of miniaturization are explored. For this purpose, the technology of the hybrid micro fuel cell described in Chapter 2 was adapted. The present work was developed in collaboration with the Genetics and Microbiology Department of the Autonomous University of Barcelona, which was in charge of conditioning of the microbial cultures. The microfabricated device performance was compared with a larger scale microbial fuel cell. Additionally, the device was used to evaluate its capability to work as a microfabricated biosensor measuring the decrease in the power generated by the electrochemically active microorganism when a toxic material become present in the anodic compartment.

6.1 MICROBIAL FUEL CELL OPERATION PRINCIPLE

Unlike conventional fuel cells, which employ hydrogen (or hydrogen-containing molecules such as alcohols) as fuel, biological fuel cells are capable of converting the chemical energy from more complex compounds, such as carbohydrates, directly into electric energy thanks to the action of biocatalysts.

There are two types of biological fuel cells, namely microbial fuel cells and enzymatic fuel cells. In a typical microbial fuel cell, an anodic potential is generated when microorganisms oxidize the organic compound, delivering electrons and protons to the medium. In contrast to microbial fuel cells, enzymatic fuel cells utilize redox enzymes instead of whole microorganisms as biocatalysts [17].

Similar to electrochemical fuel cells, a microbial fuel cell also consists of two electrodes, anode and cathode, placed in independent compartments divided by a proton exchange membrane. A schematic diagram of a microbial fuel cell is shown in Figure 6.1. In the anodic compartment, organic compounds (e.g., glucose, acetate) are oxidized by the microorganisms, generating electrons and protons in the process. For the case of an acetate molecule, this reaction will be given by:



Under normal aerobic microbial growth, the electrons generated in this process would be directly transferred to oxygen as part of the respiration process of the bacteria:



However, if the anode compartment is kept under the absence of oxygen, bacteria are forced to transfer electrons to the anode that acts, in this case as an external acceptor [1]. The electrons flow from the anode to the cathode powering an external circuit. At the same time, protons generated in the anode compartment cross the membrane to the cathodic compartment to recombine with electrons and oxygen molecules present in the medium to form water molecules; this reaction can be accelerated by the addition of iron (potassium ferricyanide), which acts as a catalyst:

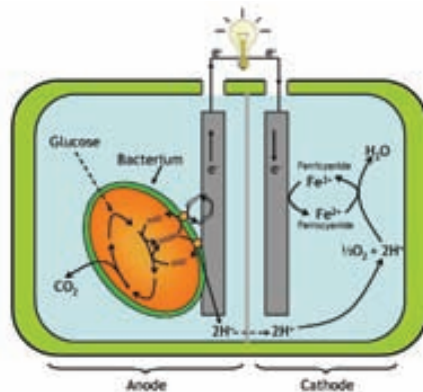
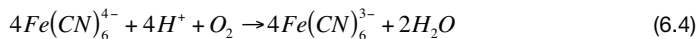
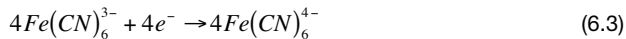


Figure 6.1 Layout of the microbial fuel cell operation.

The performance of a microbial fuel cell depends on a complex system of parameters. Apart from physical variables like anode material and fuel cell design, it is mainly the paths and mechanisms of the bioelectrochemical energy conversion that decisively determine the MFC power and energy output. The electron transfer from the microbial cell to the fuel cell anode, as a process that links microbiology and electrochemistry, represents a key factor that defines the theoretical limits of the energy conversion.

In this respect, microorganism can perform electron transfer to the anode in two different ways: mediated electron transfer (MET), in which the electron is transferred to the electrode through the mediation of dissolved redox species, and direct electron transfer (DET), in which electron transfer proceeds directly via from the bacteria membrane to the electrode (without the involvement of dissolved species) [4]. Figure 6.2 exemplifies the basic electron transfer mechanisms in microbial fuel cells.

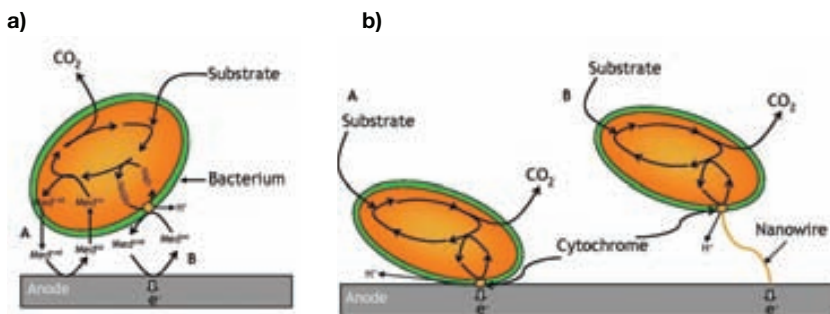


Figure 6.2 Simplified schematic illustration of electron transfer mechanisms: (a) MET via exogenous redox mediators and via bacterial metabolites, (b) DET via membrane bound cytochromes and via electronically conducting nanowires.

In the present application, *Geobacter sulfurreducens* that uses a direct electron transfer mechanism to deliver electrons to the electrode, has been used. Under favorable conditions this type of bacteria is capable of growing a biofilm on the electrode surface, being the generated energy related to the thickness and density of the biofilm. This effect shows high resemblance to the way in which catalysts cover the electrodes in electrochemical fuel cells.

6.2 DEVICE ASSEMBLY AND CHARACTERIZATION

In order to compare performance of the microfabricated microbial fuel cell, a macro scale MFC was first fabricated. This system was used to grow the cell culture, stabilize the system and act as a reference. This section starts with the preparation and characterization of the macro MFC. Subsequently, the fabrication and performance of the micro fuel cell is presented.

6.2.1 Assembly and set-up of macro MFC

The macro scale MFC system employed in this study consisted of several machined methacrylate pieces joined with screws to form a two-compartment rectangular chamber with a volume of 84 ml at each compartment (Figure 6.3). The compartments were separated by a proton exchange membrane (Nafion® 117, Dupont) with an effective area of 18 cm². Before each experiment was performed, the membranes were activated following a procedure reported in previous studies [5, 18], which consisted of boiling them in a 3% H₂O₂ solution for one hour and then rinsing in boiling deionized water for one hour to remove organic compounds. They were then boiled in 0.5 M H₂SO₄ for 1 hour to remove metal compounds and replace Na⁺ with H⁺ in the membranes and finally they were rinsed in boiling deionized water for another hour. Carbon paper (Toray carbon paper TGPH-120, no wet proofing; E-Tek Inc.) was used as the electrode material, each electrode having an area of 40 cm² and a thickness of 0.35 mm.

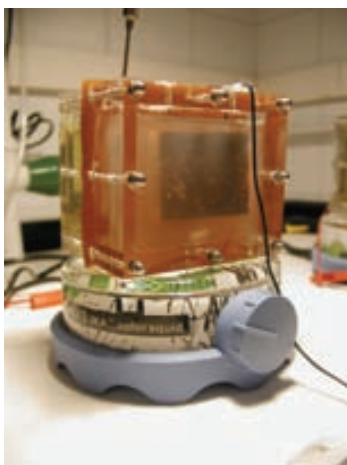


Figure 6.3 Image of the macro MFC used for comparison purposes.

A *Geobacter sulfurreducens* strain (DSM 12127) was grown in a solution containing the following (per liter): 1.5 g of NH₄Cl, 0.6 g of NaH₂PO₄, 0.1 g of KCl, 2.5 g of NaHCO₃, 0.82 g of sodium acetate, 8 g of sodium fumarate, 10 ml of vitamin mix and 10 ml of mineral mix [2, 19]. The medium was adjusted to pH 6.8. Sodium acetate served as the hydrogen-containing compound. All incubations were done at 30°C under anaerobic conditions. Culture growth time varied from 4 to 7 days.

The system was set-up by inoculating a *Geobacter sulfurreducens* culture with 10 mM acetate in the anode compartment. At the cathode compartment, an oxygenated solution containing 100 mM phosphate buffer and 50 mM potassium ferricyanide was used. The latter helps to accelerate the reduction of oxygen in water. The anode compartment was completely filled preventing formation of bubbles and sealed to avoid the entrance of oxygen thus obtaining anaerobic conditions.

During experiments, the cathodic compartment was aerated with a continuous air flux that was passed through a filter with 0.22- μM -pore-size to avoid contamination. Both compartments were stirred slowly (200 rpm) with a magnetic stir bar to keep the medium homogeneous and to avoid concentration gradients [3].

6.2.2 Characterization of macro MFC

Unlike electrochemical fuel cells, the performance of MFCs evolves with time and so does their maximum power output. Therefore, it is important to ensure that the biological component of the MFC has reached maturity before characterizing a stable MFC performance. Therefore, MFC performance evolution was characterized using a stabilization method. The procedure, consisting of periodically monitoring the I-V curves of microbial fuel cells, allows obtaining complete information about the characteristics of the cell and its efficiency as it evolves in time.

The I-V characteristic curves of the fuel cell were monitored for several days. The measurement procedure consisted on the following steps: first, the open circuit voltage (OCV) of the fuel cell was measured immediately after filling the anode compartment with the microbial medium and until signal stabilization (about an hour). After this stabilization, a series of polarization curves were recorded. The curves were done fixing the current for 3 minutes at each value, time enough for the signal to stabilize. The time required to obtain a complete I-V curve depended on the MFC performance at the moment of measurement. After each polarization curve the program returned the fuel cell to open circuit conditions and measured the voltage of the fuel cell for another stabilization period of one hour. The measurement cycle was repeated subsequently. In this way, the evolution of the maximum power given by the fuel cell could be monitored.

Stabilization measurements lasted several days because biofilm formation can take from days to weeks depending on the activity of the bacteria. In order to verify the extent of biofilm development in the DET microbial fuel cells used in this work, SEM observation was performed at after the stabilization period. Figure 6.4 shows the microbial growth observed on the carbon paper anode electrode.

The evolution of the activity of a MFC is shown in Figure 6.5a, where representative power curves obtained along a period of 7 days have been plotted. During the initial stage of the fuel cell colonization by *Geobacter*, maximum power generated was around 0.7 $\mu\text{W}/\text{cm}^2$ at a current density of 0.01 $\mu\text{A}/\text{cm}^2$. As *Geobacter* develops, the power density curves follow a trend in which maximum power is found at gradually higher current densities and the cell progressively gains the ability to support higher loads.

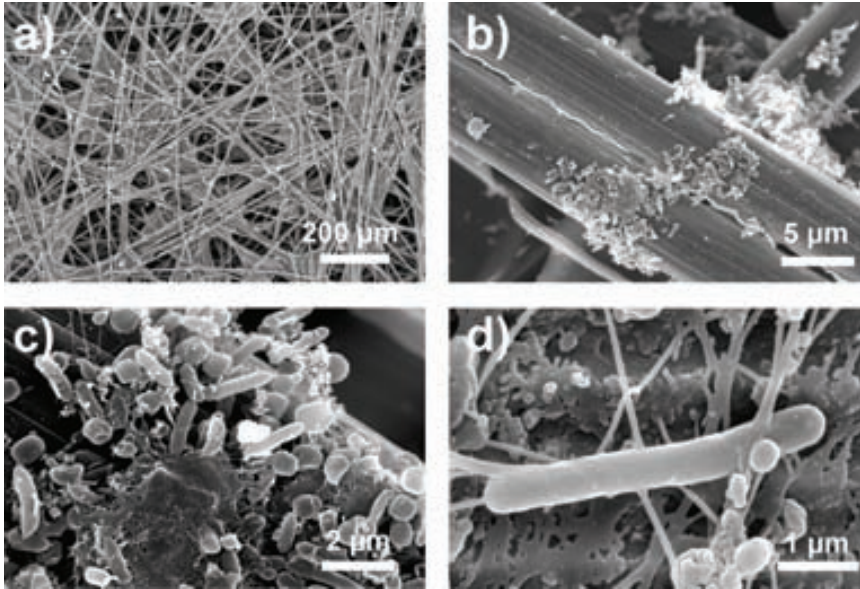


Figure 6.4 SEM images of the *Geobacter sulfurreducens* biofilm on the carbon paper electrode taken from the anode compartment of the macro MFC after the culture growth.

To visualize the evolution of maximum power output with time, the peak power of each of the curves from Figure 6.5a has been plotted in Figure 6.5b as a function of time. Data in this plot indicate how power increases significantly, after about 60 hours of operation and develops steadily, reaching a maximum stable value of $3 \mu\text{W}/\text{cm}^2$ after approximately 6 days.

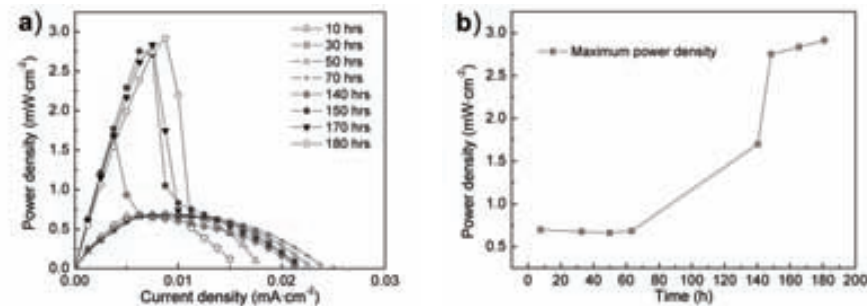


Figure 6.5 (a) Evolution of the power density curves of a direct electron transfer MFC using *Geobacter sulfurreducens* as the biocatalyst during a period of several days. (b) Evolution of the maximum power density of the same fuel cell along 7 days, the graph was obtained by plotting the maximum power density points from the curves of Figure 6.5a.

After the stabilization of the system, the catalyze solution was renewed with a fresh ferricyanide solution in order to avoid oxygen limitations; the obtained polarization curve after this change is shown in Figure 6.6.

From the figure it can be seen that the maximum power density obtained from the macro scale MFC reached $4.4 \mu\text{W}/\text{cm}^2$ at a current density of $0.03 \mu\text{A}/\text{cm}^2$.

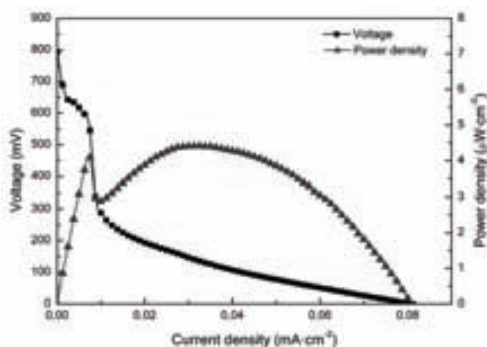


Figure 6.6 Response obtained with the macro MFC working with the same culture and conditions as the microdevice.

6.2.3 Micro MFC fabrication and assembly

The microdevice was composed of a proton exchange membrane (Nafion[®] 117, Dupont) placed between two of the microfabricated silicon current collectors metalized with a Ni-Au layer, described in section 2.1.2 of this work. The testing assembly incorporates two methacrylate pieces that comprise closed reservoirs with a working volume of $144 \mu\text{L}$ and 2 mm inlets and outlets at the sides of the compartments, which were used to establish a constant flux of the anolyte and catholyte suspensions. Since bacteria must be in physical contact with the electrode, the metalized side of the anode current collector was placed facing the culture compartment. Concordantly, the metalized side of the cathode current collector was placed facing the potassium ferricyanide solution (both silicon sides of the electrodes were facing the membrane). Figure 6.7 shows a general diagram of the microbial fuel cell using the silicon current collectors and a detail of the biofilm covering the microfabricated perforations.

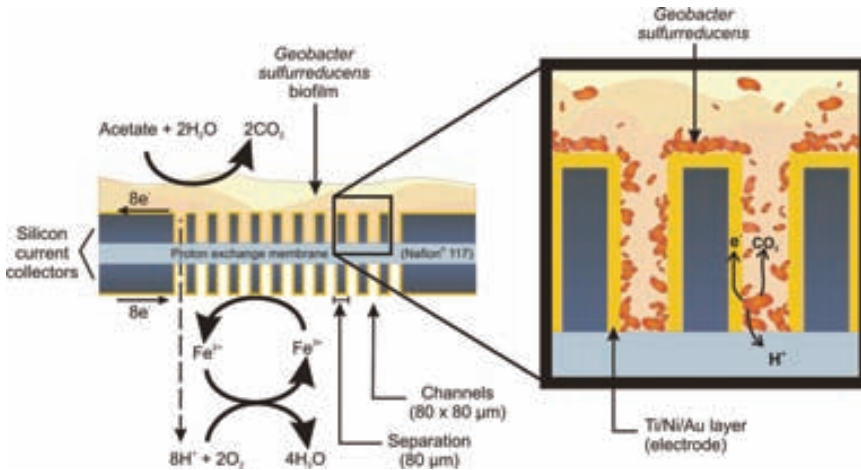


Figure 6.7 Diagram of the silicon-based microbial fuel cell using *Geobacter sulfurreducens*.

The system was set-up by passing the flow of the *Geobacter sulfurreducens* culture, first through the macro MFC, and then through the anode compartment of the microdevice until the biofilm was formed on the surface of the electrode. In the same way, the catholyte from the macro MFC was pumped through the cathode compartment. Figure 6.8 shows a schematic diagram of the microMFC and a picture of the assembled device.

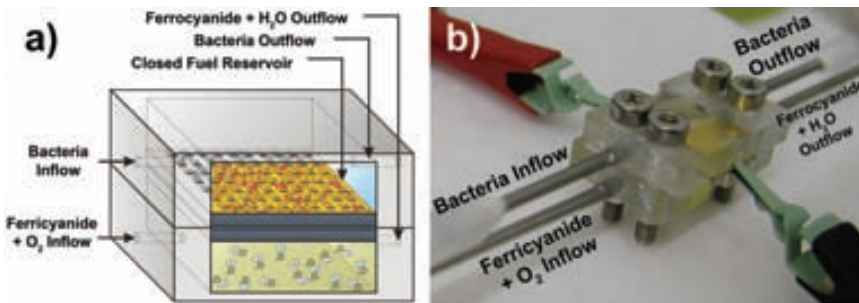


Figure 6.8 (a) Schematic of the experimental set-up of the microfabricated microbial fuel cell and (b) picture of the final testing assembly.

6.2.4 Micro MFC performance characterization

The operation of the microdevice as a MFC was characterized under the conditions and methods described previously. As both macro and micro MFCs were inoculated with the same culture, the obtained power densities could be compared.

As with the macro MFC, the performance evolution of the micro MFC was monitored by measuring the I-V polarization curves. Figure 6.9 shows polarization curves from the micro MFC obtained at the 1st, 2nd, 6th and 7th day of measurement. Despite the fact that the microdevice reached maximum current densities (0.014 mA/cm^2) about 4 times lower than those found in the macro fuel cell (0.08 mA/cm^2), maximum power densities were significantly higher in the micro fuel cell, yielding a maximum power density of $6.5 \text{ } \mu\text{W/cm}^2$, compared to $4.4 \text{ } \mu\text{W/cm}^2$ obtained previously with the macro device. The capability to sustain the voltage at higher current densities is due to the fact that in this microdevice the distances between all the elements (biofilm, anode, proton exchange membrane and anode) are minimal. As a result, the internal resistance of the cell due to mass transport limitations between the different elements and the ohmic losses were reduced. Compared to the power densities reported by others [20], the device is capable to deliver 3000 times more power density at the same current density ranges.

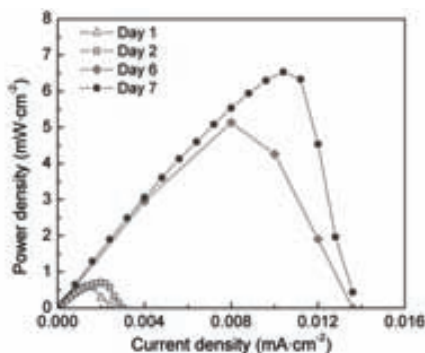


Figure 6.9 Maximum power densities obtained with the microdevice operating as a MFC at different days.

The stability and response of the micro MFC was evaluated by subjecting the device to different constant output currents while recording the voltage evolution in time, results can be seen in Figure 6.10. The micro MFC demonstrated a fast response to changes in the currents corresponding to values below its maximum power, stabilizing the voltage within 10 seconds. For currents above the maximum power of the fuel cell, the voltage did not reach a stable value. However, it has to be noticed that the device recovered rapidly its open circuit voltage after removing the current load.

Scanning electron microscopy was carried out to examine the *Geobacter sulfurreducens* biofilm growth and attachment to the electrode after the stabilization measurements. Figure 6.11a shows the SEM images of the bacteria on the micromachined current collector surface, where the extent and the geometry of the attachment to the Au electrode can be seen. In this case, the silicon microstructuring of the current collectors increased the available area for biofilm formation compared to a flat surface. Figures 6.11 (b-d) show SEM images of the biofilm found on the vertical walls of the channels. It could be seen that the roughness produced in the walls by the DRIE silicon etching process, creates a very suitable surface for the

microorganism fixing (Figure 6.11b-d). Furthermore, the Au surface coating of the silicon structure has been proved to have an effective electrochemical interaction with the bacteria [21].

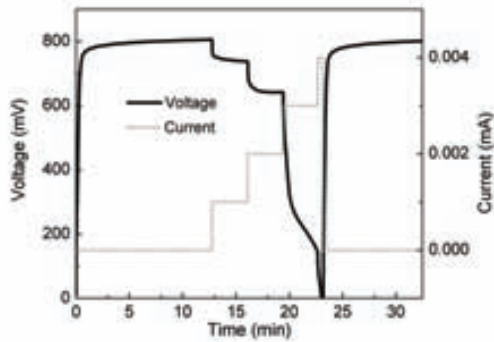


Figure 6.10 Performance of the microfabricated microbial fuel cell working at a constant output current over a long period of time.

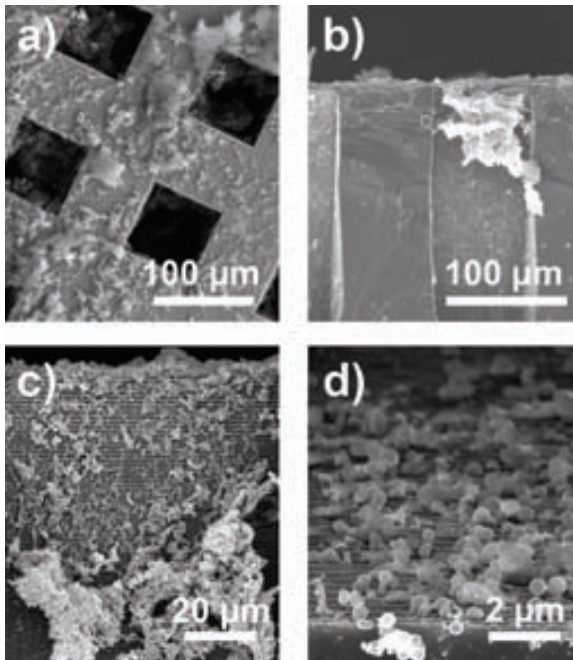


Figure 6.11 SEM images from (a) top view and (b-d) cross-section view of a silicon micromachined current collector showing the *Geobacter sulfurreducens* biofilm growth.

Even though direct electron transfer from the biofilm to the electrode is the most effective electron delivery mechanism of *Geobacter*, the bacteria suspended in the medium can also contribute to the current generation.

As the operation conditions used in the experiment allowed for growth of both, a microbial biofilm attached to the anode and free living cells suspended in the bulk of the anolyte, it was necessary to quantify the contribution of each element in the output power. Thus, after the biofilm growth, the culture was removed and replaced by fresh medium without bacteria and the MFC was characterized again. The polarization curve of the fuel cell obtained after replacing the anolyte suspension with fresh culture medium is shown in Figure 6.12. After eliminating the bacteria present in the medium, the maximum power density dropped from 6.53 to 5.17 $\mu\text{W}/\text{cm}^2$, showing that the contribution of suspended bacteria was about 20% of the power generated in the cell.

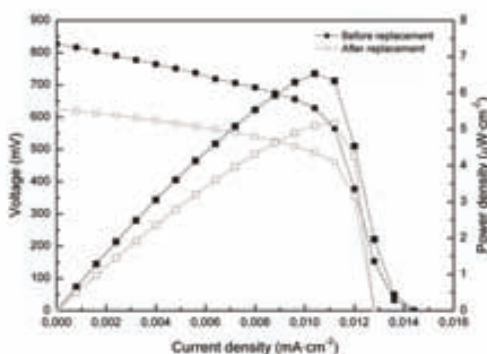


Figure 6.12 Maximum power densities obtained with the microdevice operating as a MFC before and after replacing the bacterial culture by fresh medium without bacteria.

These results have demonstrated the feasibility of a microMFC approach using *Geobacter sulfurreducens* and micromachined silicon current collectors covered with gold as the electron acceptor. Furthermore, it has been shown that the miniaturization of the system results in an enhancement of the performance of this kind of fuel cells due to the reduction of dimensions and the compatibility of the materials. After this validation, the microfabricated microbial fuel cell was used to evaluate its operation as a toxicity biosensor. The result of the study is presented in the next section.

6.3 MICROFABRICATED MFC AS TOXICITY BIOSENSOR

A microbial biosensor is an analytical device that couples a biological sensing element with a transducer to enable rapid, accurate and sensitive detection of target analytes in fields as diverse as medicine, environmental monitoring, defense, food processing and safety [10]. The transducer converts this biological signal into a measurable response such as current, potential or absorption of light through electrochemical or optical means, which can be further amplified, processed and stored for later analysis [22-24].

Biomolecules such as enzymes, antibodies, receptors, organelles and microorganisms as well as animal and plant cells or tissues have been used as biological sensing elements. Among these, microorganisms offer advantages of ability to detect a wide range of chemical substances, amenability to genetic modification, and broad operating pH and temperature range, making them ideal as biological sensing materials [25].

Microbial biosensors use the respiratory and metabolic functions of the microorganisms to detect a substance that is either a substrate or an inhibitor of these processes. Microorganisms have been integrated with a variety of transducers such as amperometric, potentiometric, calorimetric, conductimetric, colorimetric, luminescence and fluorescence to construct biosensor devices [10].

Microbial fuel cells have been studied as biochemical oxygen demand (BOD) sensors for a long time. Since a BOD sensor based on MFC was reported in 1977 [26], a variety of MFC BOD sensors with use of electron-mediator have been developed [27, 28]. Even though the addition of mediators in these biosensors can enhance the electron transfer, these biosensors have poor stability because mediators are toxic to bacteria. Recently, mediator-less microbial fuel cells have been exploited to fabricate novel BOD sensors for continuous and real-time monitoring [7, 9]. Moreover, Kim et al. [29] have already demonstrated that MFC can be also used as toxicity biosensor.

6.3.1 Biosensors for toxicity measurement

As a consequence of human activity, large amounts of toxic spills with different toxic levels are generated, which directly or indirectly could contaminate aquifers and superficial waters, preventing their later exploitation. The polluting agents susceptible to generate these problems are of very diverse nature and go from pesticides, coming from the agrarian activity, to chemical compounds from different industrial sectors that could deliberately or accidentally contaminate continental waters. The consequences of these spills are catastrophic for the environment.

Biological assays for toxicity have been implemented to detect acute toxicity as well as chronic toxicity in environmental samples as well as in different types of effluents. Average time required to perform some of these assays is about 96 h. The use of microbial fuel cells for detection of toxic compounds can minimize the time, the cost and the personnel required for measuring toxicity in water.

Although there are several proved methodologies for toxicity measurements, this is the first time that a microfabricated toxicity sensor based on microbial fuel cells has been developed.

6.3.2 Toxicity sensing application

The operation of the microfabricated microbial fuel cell as toxicity sensor involves setting the cell at a fixed current while monitoring the changes in the output voltage caused by the addition of the toxic compound. In order to ensure a stable measurement without compromising fuel cell performance due to mass transport

limitations, the current was fixed to $1 \mu\text{A}$ – which corresponded to a current density of 0.004 mA/cm^2 . Prior to the toxicity measurement, the cells were operated in a fixed current mode in order to test the stability of the output voltage in time. These tests were carried out in different cells and a variation less than 5% in the output voltage within periods of at least 24 hours was observed. These measurements were considered as control experiments in the absence of toxic. Formaldehyde was chosen as the toxic to be added to the MFC for toxicity experiments because it is a commonly used disinfectant and biocide in microbiology. The addition of this substance allowed observing the inhibition of bacterial metabolic activity.

In a first trial, once the signal of the MFC set to a fixed current stabilized, formaldehyde was added to the MFC anode compartment at a final concentration of 4%. An immediate drop in the power production was observed. Formaldehyde concentration was lowered stepwise in subsequent experiments in order to measure the minimum formaldehyde concentration detected by our device. The lowest tested concentration was 0.1% and in all cases the sensor was able to detect the presence of the toxic compound showing a steep drop in the output voltage (Figure 6.13). All tested concentrations irreversibly inactivated the biofilm (activity was not recovered when going back to a clean substrate solution).

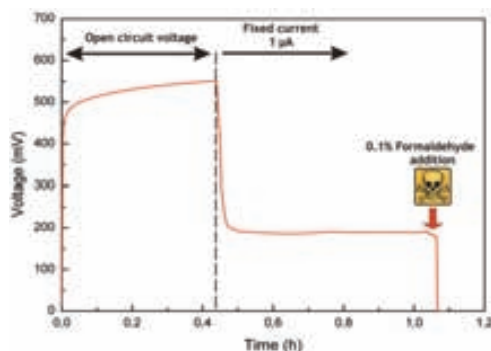


Figure 6.13 Voltage evolution of the MFC biosensor. Toxicity measurement response obtained with the microfabricated device when 0.1% Formaldehyde was added to the anodic compartment of the cell.

Performance and sensitivity of a MFC-based toxicity sensor depends to a large extent on the type of organism used in the cell. Recently reported work [30] showed that *Geobacter* is not inhibited by a range of compounds from antibiotics to heavy metals. Even though the presented implementation of the sensor requires the use of electrogenic organisms (*Geobacter* or *Shewanella*), it is currently under study the possibility of engineering the system to use organisms that, although unable of direct electron transfer to the anode, might provide enhanced sensitivity to different compounds and concentrations. Further work has to be done in order to determine the sensitivity and response of the sensor to different toxic compounds. Moreover, the development of an efficient cathode that allows the elimination of potassium ferricyanide is needed to achieve a simpler design.

6.4 DISCUSSION AND SUMMARY

The application of the silicon-based micro fuel cell system as a miniaturized microbial fuel cell has been validated. The developed microfabricated device was able to give a remarkable performance due to an efficient biofilm formation on the surface and on the channel walls of the electrodes.

The microfabricated MFC was capable of providing an electrical power in the range of 1-10 $\mu\text{W}/\text{cm}^2$, the same power magnitude delivered from a larger scale device. In fact, an increase in the maximum power was observed in the miniaturized system, which was attributed to the decrease of mass transport limitations caused by the reduction of the distance between components.

Furthermore, it was demonstrated that the device could be operated as a toxicity biosensor able to provide an instantaneous response when exposed to the presence of a toxic compound. On this respect, different ideas of using bacteria in the cathodic compartment are being considered, which opens a wide range of possibilities for biosensors. The bacteria diversity that can be employed in microbial fuel cells, the different electron transfer mechanisms and all the parameters that affect their performance give an estimation of the complexity of this type of devices. However, this diversity of parameters allows selecting and screening for microorganisms with specific activity for certain chemical compounds in order to design more complex, sensitive and highly selective devices with fast responses.

The compact design of the microdevice fabricated along this study makes it suitable for its incorporation into measurement equipment either as an individual device or as an array of sensors for high throughput processing [31].

Moreover, the combination of this microbial fuel cell approach with the innovations on polymer microfabrication technologies described in Chapters 3 to 5 would lead to the development of a new generation of low cost, biocompatible, power generating microdevices.

References in Chapter 6.

- [1] Bennetto H P 1990 Electricity generation by microorganisms *Biotechnology Education* **1** 163-8
- [2] Bond D R and Lovley D R 2003 Electricity Production by *Geobacter sulfurreducens* Attached to Electrodes *Appl. Environ. Microbiol.* **69** 1548-55
- [3] Davila D, Esquivel J P, Vignes N, Sanchez O, Garrido L, Tomas N, Sabate N, del Campo F J, Munoz F J and Mas J 2008 Development and optimization of microbial fuel cells *Journal of New Materials for Electrochemical Systems* **11** 99-103
- [4] Logan B E and Regan J M 2006 Electricity-producing bacterial communities in microbial fuel cells *Trends in Microbiology* **14** 512-8
- [5] Lovley D R 2006 Bug juice: harvesting electricity with microorganisms *Nat Rev Micro* **4** 497-508
- [6] Rabaey K, Lissens G, Siciliano S D and Verstraete W 2003 A microbial fuel cell capable of converting glucose to electricity at high rate and efficiency *Biotechnology Letters* **25** 1531-5
- [7] Chang I S, Jang J K, Gil G C, Kim M, Kim H J, Cho B W and Kim B H 2004 Continuous determination of biochemical oxygen demand using microbial fuel cell type biosensor *Biosensors and Bioelectronics* **19** 607-13
- [8] Gil G-C, Chang I-S, Kim B H, Kim M, Jang J-K, Park H S and Kim H J 2003 Operational parameters affecting the performance of a mediator-less microbial fuel cell *Biosensors and Bioelectronics* **18** 327-34
- [9] Kim B H, Chang I S, Cheol Gil G, Park H S and Kim H J 2003 Novel BOD (biological oxygen demand) sensor using mediator-less microbial fuel cell *Biotechnology Letters* **25** 541-5
- [10] Lei Y, Chen W and Mulchandani A 2006 Microbial biosensors *Analytica Chimica Acta* **568** 200-10
- [11] Tront J, Fortner J, Plötze M, Hughes J and Puzrin A 2008 Microbial fuel cell technology for measurement of microbial respiration of lactate as an example of bioremediation amendment *Biotechnology Letters* **30** 1385-90
- [12] Tront J M, Fortner J D, Pl'tze M, Hughes J B and Puzrin A M 2008 Microbial fuel cell biosensor for in situ assessment of microbial activity *Biosensors and Bioelectronics* **24** 586-90
- [13] Biffinger J C, Pietron J, Ray R, Little B and Ringeisen B R 2007 A biofilm enhanced miniature microbial fuel cell using *Shewanella oneidensis* DSP10 and oxygen reduction cathodes *Biosensors and Bioelectronics* **22** 1672-9
- [14] Ringeisen B R, Henderson E, Wu P K, Pietron J, Ray R, Little B, Biffinger J C and Jones-Meehan J M 2006 High Power Density from a Miniature Microbial Fuel Cell Using *Shewanella oneidensis* DSP10 *Environmental Science & Technology* **40** 2629-34
- [15] Ringeisen B R, Ray R and Little B 2007 A miniature microbial fuel cell operating with an aerobic anode chamber *J. Power Sources* **165** 591-7
- [16] Chiao M, Lam K B and Lin L 2003 Micromachined microbial fuel cells 383
- [17] Shukla A K, Suresh P, Berchmans S and Rajendran A 2004 Biological fuel cells and their applications *Current Science* **87** 455-68
- [18] Sim W Y, Kim G Y and Yang S S 2001 Fabrication of micro power source (MPS) using a micro direct methanol fuel cell (mu DMFC) for the medical application *14th IEEE International Conference on Micro Electro Mechanical Systems, Technical Digest* 341-4
- [19] Lovley D R and Phillips E J P 1988 Novel Mode of Microbial Energy Metabolism: Organic Carbon Oxidation Coupled to Dissimilatory Reduction of Iron or Manganese *Appl. Environ. Microbiol.* **54** 1472-80
- [20] Kim M, Hyun M S, Gadd G M and Kim H J 2007 A novel biomonitoring system using microbial fuel cells *Journal of Environmental Monitoring* **9** 1323-8
- [21] Richter H, McCarthy K, Nevin K P, Johnson J P, Rotello V M and Lovley D R 2008 Electricity Generation by *Geobacter sulfurreducens* Attached to Gold Electrodes *Langmuir* **24** 4376-9

- [22] Turner A P F, Karube I and Wilson G S 1992 *Biosensors: Fundamentals and Applications* (Moscow: Mir Publishers)
- [23] Mulchandani A and Rogers K R 1998 *Enzyme and Microbial Biosensors: Techniques and Protocols* (Totowa, NJ Humana Press)
- [24] Tran M C 1993 *Biosensors* (Paris: Chapman and Hall and Masson)
- [25] Blum L J and Coulet P R 1991 *Biosensor Principles and Applications* (New York: Marcel Dekker)
- [26] Karube I, Matsunaga T, Mitsuda S and Suzuki S 1977 Microbial electrode BOD sensors *Biotechnology and Bioengineering* **19** 1535-47
- [27] Matsunaga T, Karube I and Suzuki S 1980 A specific microbial sensor for formic acid *Eur. J. Appl. Microbiol. Biotechnol.* **10** 235-43
- [28] Stirling J L, Bennetto H P, Delaney G M, Mason J R, Roller S D, Tanaka K and Thurston C F 1983 Microbial fuel cells *Biochemical Society Transactions* **11** 451-3
- [29] Kim H J, Choi D W, Hyun M S and Nam S H 2003 Method and device for detecting toxic material in water using microbial fuel cell. ed W I P Organization
- [30] Patil S, Harnisch F and Schröder U 2010 Toxicity Response of Electroactive Microbial Biofilms—A Decisive Feature for Potential Biosensor and Power Source Applications *ChemPhysChem* **11** 2834-7
- [31] Hou H, Li L, Cho Y, de Figueiredo P and Han A 2009 Microfabricated Microbial Fuel Cell Arrays Reveal Electrochemically Active Microbes *PLoS ONE* **4** e6570

7 Fuel cell-powered microfluidic platform for Lab-on-a-Chip applications

From the early-developed microfluidic devices in the 1970's, focused on gas chromatography [1] and ink jet printer nozzles [2], the advances in this field have diversified to numerous applications [3, 4]. Since the term micro Total Analysis System (μ -TAS) was coined by A. Manz in the beginning of the 1990's [5], the attention on microfluidics for chemical and biological analysis has evolved rapidly, a fact confirmed by the increasing number of publications and patent applications up to date [6]. Lab-on-chip devices have numerous applications, which include biological and chemical analysis, point-of-care testing, clinical and forensic analysis, molecular diagnostics and medical diagnostics [7-12].

Originally, the benefits of microfluidic devices were centred in the enhancement of analytical performance attained by the system miniaturization. Further developments showed that the advantages also involved diminution of the reagents volume, higher automation and reduction of manufacturing costs [13]. Generally, most microfluidic systems require external components such as pumps, power sources and control electronics to perform the complete sample analysis [14]. These elements increase device complexity and limit portability and flexibility of the Lab-on-a-chip device. For this reason it is often mentioned that microfluidic chips are microscale devices coupled to macroscale infrastructures. Therefore, the achievement of a higher degree of integration of components – especially micropumps and power sources - is currently being pursued to obtain totally autonomous devices.

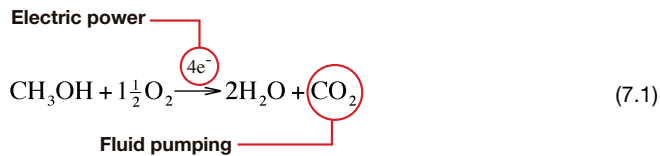
Despite the wide range of miniaturized power sources being under development [15-17], only few attempts of integrating these energy sources in microfluidic platforms have been reported. Most common strategies are based on microbatteries and RF-powered devices. Even though both approaches have interesting advantages, they still face some difficulties, e.g. operation of RF devices is limited to a distance from the power source and batteries suffer from restricted application due to their necessity for recharging and their limited power density of miniaturized scale. However, micro fuel cells – which can operate as long as fuel is supplied - have been scarcely applied to microfluidic platforms despite the numerous prototypes found in the literature [18].

On the other hand, a great part of the research has been oriented to the integration of liquid handling microfluidic structures such as microvalves and micropumps. Throughout these years, several surveys dedicated to micropumping systems have reported different classifications based on a number of features [19-21]. Among these categorizations, the most accepted is to distinguish between mechanic pumps that have moving parts (check valves, peristaltic, rotary, etc) and non-mechanic

pumps (electrokinetic, electrohydrodynamic, electrowetting, electrochemical, etc). One of the pumps in this second category are bubble-driven micropumps, which use the pressure of a gas generated by different methods such as electrolysis, thermal bubble generation, injection or chemical reaction.

This chapter shows that direct methanol micro fuel cells can be very interesting candidates to power microfluidic devices and, as it has been shown in previous chapters of this thesis, they can be fabricated within the same materials and technologies used for Lab-on-a-chip devices (e.g. silicon, PDMS and SU-8).

The development presented here proposes the integration of a μ DMFC together with a microfluidic platform showing an additional feature provided by the fuel cell operation that can be of great interest for microfluidic applications. This work has been carried out in collaboration with the Nanobioengineering Group at the Institut de bioenginyeria de Catalunya (IBEC) in Barcelona. The approach takes advantage of the CO_2 gas produced by the fuel cell reaction to pump a liquid through a microfluidic system. This can be illustrated by looking at the electrochemical reaction that takes place in a DMFC:



Power generation comes from the decomposition of methanol molecules to electrons, protons and CO_2 , in the proportion defined by the reaction. Generally, the produced CO_2 gas represents an unwanted side-product of the reaction, as its can cause the blockage of catalytic reaction sites. For this reason, solutions for an efficient exhaustion of CO_2 from the anode chamber have been proposed in the literature [22-24]. Alternatively, recent works have reported the profitable use of the pressure increase produced by the accumulation of CO_2 bubbles formed during micro fuel cell operation. In those works, the driving force was used to perform an auto-regulation of the fuel cell system [25, 26].

In the present approach, the CO_2 driving force is used to perform a pumping action in a microfluidic platform. The basic idea is schematically depicted in Figure 7.1. The proposed assembly consists of the coupling of a micro direct methanol fuel cell with a microfluidic system. In this way, the electric power produced by the fuel cell is available to enable any functionality required by the microfluidic chip, while the generated CO_2 produces a pressure capable of pumping a liquid volume through a microchannel.

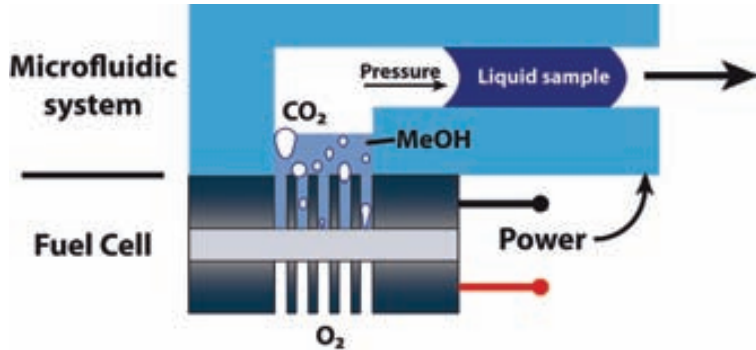


Figure 7.1 Operation principle of the fuel cell-powered microfluidic platform.

7.1 DESIGN AND FABRICATION OF THE SYSTEM

The system used to validate this approach comprises a hybrid micro DMFC (prototype presented in Chapter 2) and a PDMS microfluidic component responsible of the micropumping. A diagram of the developed setup is shown in Figure 7.2.

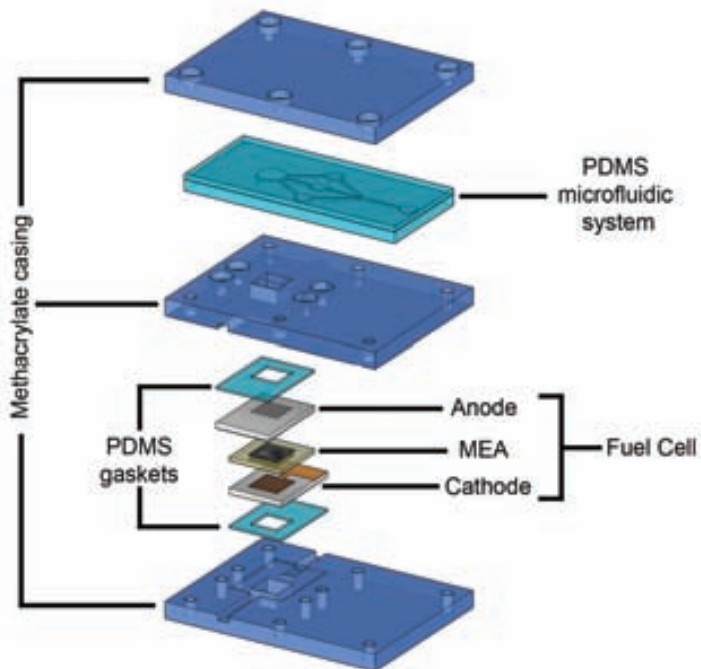
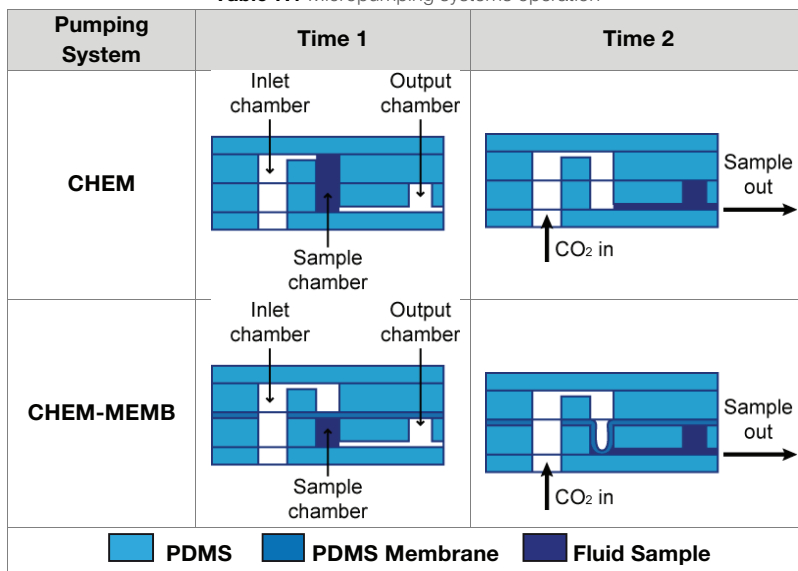


Figure 7.2 Exploded view of the system used for characterization of the fuel cell-powered microfluidic platform.

The components are assembled with an external housing composed of three tailored methacrylate pieces to facilitate the optical characterization of the fluxes. The middle and lower pieces are used to contain the micro fuel cell prototype and two extra PDMS gaskets that improve the sealing of the anodic and cathodic compartments. The top methacrylate piece is used to press the microfluidic system against the middle piece. The PDMS microfluidic system is composed by a set of three chambers connected to a microchannel through which a liquid sample is forced to flow. The combination of this microfluidic system with the micro fuel cell gives rise to a micropump.

The micropumping principle in which the devices are based consist of a combination of two different bubble-driven pumping approaches found in the literature [14, 27]. In the first one, the bubbles produced by the reaction of a Pt/Ag pin in contact with peroxide push the fluid sample through a protein assay microfluidic chip. This chemical pump allows a continuous flow rate until the sample is completely evacuated from the microfluidic chip. In the second approach, the bubbles produced by the electrolysis of water push a polymeric membrane that transfers the pressure to the fluid sample by an intermediate hydraulic fluid. This electro-hydraulic pump approach allows a precise control of the flow rate as well as flexibility in the volume of reagents to be pumped by changing the chambers volume ratios. The configuration of this system has the added advantage of keeping the produced gas separated from the sample. However, it requires a more complex fabrication, which involves filling a hydraulic chamber - avoiding any bubble - prior to the device sealing.

In the present chapter, both micropumping concepts were tested in two different designs. In the first design (labeled as CHEM) the liquid sample is pushed through a microchannel directly pressed by the CO₂ coming from the fuel cell. In the second design (CHEM-MEMB), a thin PDMS membrane separates the sample from the CO₂. In this way, when the gas pressure in the inlet chamber increases, the membrane is deformed and the sample is impelled through the microchannel. The times presented in the table correspond to the device condition before (Time 1) and after (Time 2) starting the CO₂ production. The main features and operation of the fabricated micropumping systems are presented in Table 7.1.

Table 7.1 Micropumping systems operation

7.1.1 Microfluidic system fabrication

The microfluidic components were fabricated by bonding several microstructured PDMS layers (ELASTOSIL 601 RT from Wacker). Fabrication of PDMS components was performed by casting. For that purpose, a SU-8 master was fabricated on a 500 μm thick, 100 mm silicon wafer substrate.

The master defined microchannels of 200 μm width and 13-20 mm length. The channel height (100 μm) was defined by the thickness of the resist. Before starting the lithography process, the wafers were dehydrated at 200 $^{\circ}\text{C}$ for 30 min. Then, a layer of SU-8 50 was spin-coated over the wafer at 2000 rpm for 35 s to obtain a 100 μm thick layer. The soft-bake consisted of a series of temperature steps performed over a hot plate starting with a 60 min resting period at 25 $^{\circ}\text{C}$, followed by 6 min at 65 $^{\circ}\text{C}$, 90 min at 95 $^{\circ}\text{C}$ and 10 hours cool-down to 25 $^{\circ}\text{C}$. The UV-exposure was performed with a dose of 400 mJ/cm^2 . Post-exposure bake consisted of a ramped baking in a hot-plate starting with 15 min at 65 $^{\circ}\text{C}$, 30 min at 95 $^{\circ}\text{C}$ and followed by a 10 h cool-down to room temperature. Finally, the layer was developed with agitation for 15 min in mr-600 Dev and then rinsed in 2-propanol and deionized water. Figure 7.3 shows an image of one of the silicon wafers with the SU-8 structures.

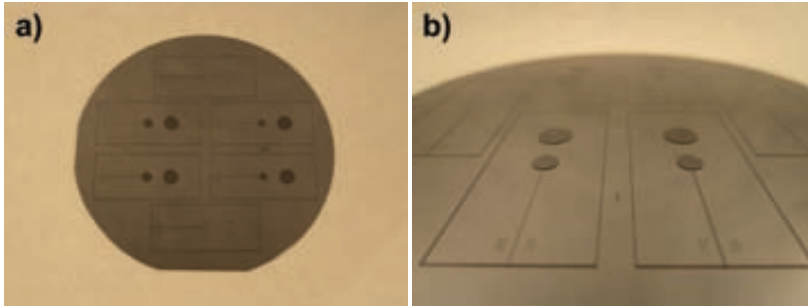


Figure 7.3 SU-8 masters on silicon wafers used for replication of microchannels to PDMS.

The PDMS prepolymer and its curing agent were mixed in a 9:1 proportion and degassed for 10 min to remove air bubbles. The replication was done by fixing the master to a metallic ring that determined the thickness of the PDMS layer (shown in Figure 7.4). The PDMS was poured over the master and covered by a polycarbonate plate to obtain a flat surface. PDMS was then cured at 85° for two hours, removed from the master and cut into individual components with dimensions of 18 mm x 40 mm. The cavities for the inlet, sample and outlet chambers were done using a hole-puncher of diameter (4, 5, 10 mm) depending on the design.



Figure 7.4 Metallic ring used for replication of PDMS master. The picture shows the wafer inside the ring, filled with PDMS and covered by the polycarbonate plate.

The PDMS membranes used in the CHEM-MEMB configuration were obtained by spin-coating the PDMS mixture on 10-mm rounded polycarbonate substrates at different speeds (1000, 2000, 3000, 4000 and 5000 rpm) and cured at 80 °C for 2 hours. After curing, the thickness of the PDMS layer was measured using a White Light Interferometer. Figure 7.5 shows the relation of spin velocity versus thickness of the membranes and device yield. Achieving lower membrane thicknesses is desirable to reduce the mechanical resistance of the material when expanded by the CO₂ pressure. A preliminary characterization confirmed that membranes with a thickness of 50 μm or less were suitable for this application. However, the yield of the working devices drastically decreased as the PDMS membrane thickness was reduced beyond 30 μm. For this reason, the final CHEM-MEMB devices used for the characterization presented in this chapter incorporated membranes with a thickness of 50 μm.

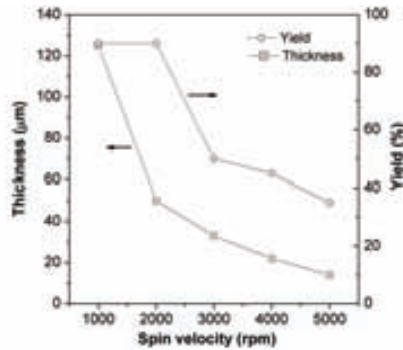


Figure 7.5 Thickness and yield of PDMS membranes at different spinning velocities on polycarbonate substrates.

To obtain the complete micropumping systems, the assemblies of different PDMS layers were bonded by oxygen plasma treatment (40 W, 60 sccm, 30 s) followed by a thermal treatment (25 min at 100 °C) keeping the stack pressed by metallic clips. Figure 7.6 shows pictures of the side and top views of the bonded PDMS microfluidic components. The sample chamber has been filled with the liquid to help visualization. A picture of the assembled microfluidic platform is shown in Figure 7.7.

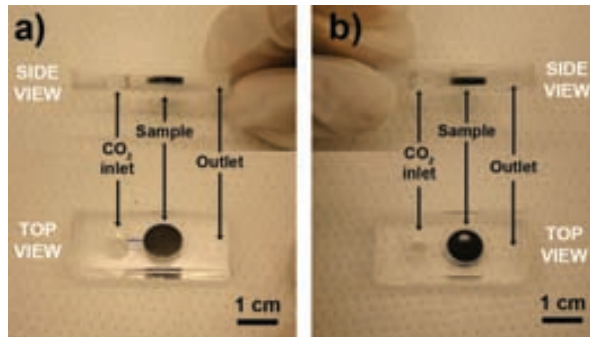


Figure 7.6 Pictures of the PDMS microfluidic systems (a) CHEM and (b) CHEM-MEMB after oxygen plasma bonding. The components have been filled with the liquid sample to help visualizing the chamber.

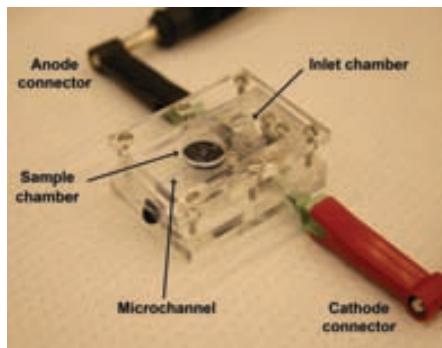


Figure 7.7 Picture of the complete microfluidic platform.

7.2 MICROFLUIDIC PLATFORM CHARACTERIZATION



In order to evaluate the operation of the fuel cell powered microfluidic platform, both micropump configurations were first tested with the fuel cell working in short-circuit. When working at this regime, the fuel cell produces the maximum current, which results in a maximal production of CO_2 . In this case, the generation of the highest pressure was guaranteed, but the power obtained from the fuel cell was zero. This characterization allowed pointing out the attributes of both micropump configurations, which defined the approach that would be the most adequate for a subsequent thorough fluidic characterization.

After the preliminary characterization, one of the systems was subjected to a set of measurements under different fuel cell operating conditions to evaluate the relation of output power and pumping flow rate. This second part of the characterization was performed on one side, using a conventional digital videocamera to monitor the time needed to transfer a known volume of sample, and on the other using a high-speed visual system connected to a transmission microscope to measure the velocity of particles dissolved in the liquid sample.

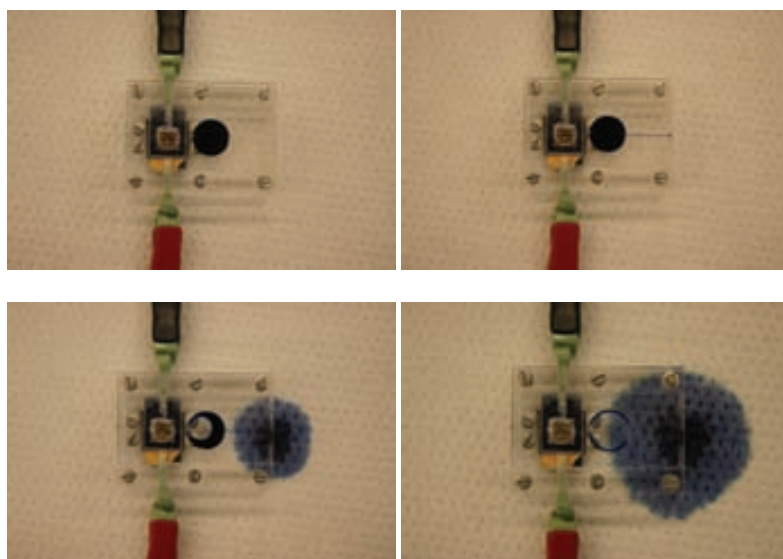
7.2.1 Preliminary testing of micropumps

The two micropump systems were characterized using a μDMFC with silicon current collectors with open ratios of 23% and 40% at the anode and cathode respectively. The fuel cell was fed with a 2M methanol concentration. The correct operation of the fuel cell was verified each time before assembling the entire system. In order to produce the maximum quantity of CO_2 , the fuel cell was short-circuited while monitoring the current with a multimeter. The current measured during the experiments was 25 ± 5 mA. The volume sample used for both systems was 170 μl . The geometric parameters of the characterized microfluidic devices are shown in Table 7.2.

Table 7.2 Description of the characterized micropumping devices.

Pumping Device	Parameters
	Inlet chamber diameter: 6 mm Sample chamber diameter: 10 mm Outlet chamber: No Sample volume: 170 μ l
	Inlet chamber diameter: 6 mm Sample chamber diameter: 10 mm Outlet chamber: No Membrane thickness: 50 μ m Sample volume: 170 μ l

In the CHEM system, the produced gas pushes the sample to the outlet until the sample chamber was completely emptied. After this, the gas production was maintained until the sample was expelled from the microchannel and finally out from the device. The subsequent gas produced by the fuel cell was continuously released through the fluidic network. This system showed a fast response, the microchannel was filled within the first 10 seconds and the sample was completely evacuated in the lapse of 11 minutes. Figure 7.8 shows images of the characterization of the CHEM system.

**Figure 7.8** Operation of CHEM micropump with larger sample volume at different times.

In the CHEM-MEMB system, the membrane covering the sample chamber was deflected by the produced gas pressure, pumping the sample through the microchannel. Even though most of the sample was evacuated from the device, part of the liquid remained at the sample chamber and the microchannel. In contrast with the CHEM system, in this case when the production of CO_2 was maintained after the PDMS membrane reached its maximum deflection, the generated pressure provoked

that the methanol leaked through the union of current collector and MEA. This system needed longer time to start the flow (about 30 seconds) but the time to empty the sample chamber was comparable to the one observed using the CHEM system. Figure 7.9 shows images of the characterization of CHEM-MEMB system.

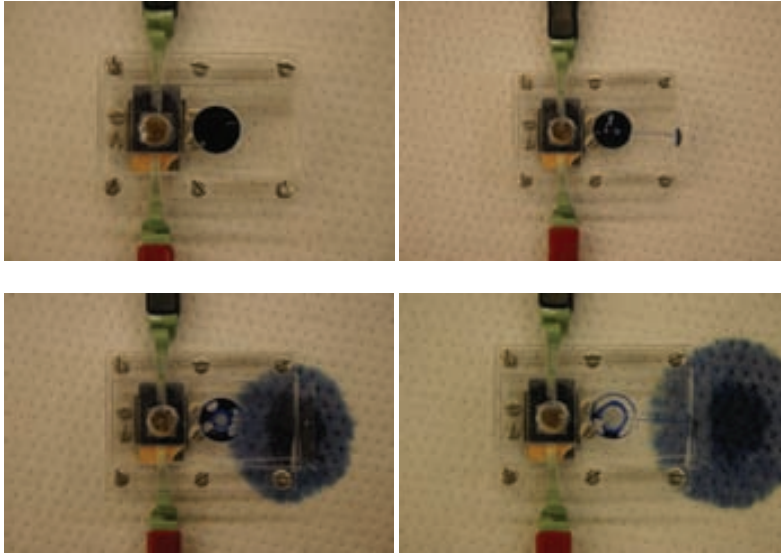


Figure 7.9 Operation of CHEM-MEMB micropump at different times.

From these tests it could be seen that the pumping of a liquid sample through a microfluidic system using the CO_2 produced from a micro fuel cell was successfully achieved with both micropumping systems.

CHEM-MEMB system has the advantage that the CO_2 is not directly in contact with the liquid sample because of the PDMS membrane. This would be very convenient to prevent contamination or disturbance in the sample, particularly important for biological or chemical applications. However, the inclusion of this element represents an additional mechanical resistance against the pressure produced by the micro fuel cell. Another issue that must be taken into consideration is that the production of CO_2 should be controlled to avoid the generation of an excessive pressure in the chamber that would result in methanol leaks or device failure. Additional elements such as escape valves or pressure sensors would then be necessary in a practical application to prevent these problems.

CHEM system has a shorter response time because the pressure of the gas is directly transferred to the liquid sample. As PDMS membranes are not incorporated in this design, the fabrication complexity and processing time are highly minimized. Furthermore, the operation of this design permits the complete ejection of the liquid sample and the consequent exhaustion of the gas through the same microfluidic network. This allows managing the gas pressure without compromising the device integrity.

As it can be seen, each of these systems present their own strengths and weaknesses, thus the election of the best system should be based on the specific application in which it will be used. The main characteristics of the different tested systems are summarized in Table 7.3.

Table 7.3 Main features of the tested micropumping systems.


Characteristic	CHEM	CHEM-MEMB
Gas in contact with liquid sample	X	
Gas not in contact with liquid sample		✓
Resistance to deform PDMS membrane(s)		X
Time of response	+	++
Fabrication complexity	+	++

✓: Advantage X: Disadvantage +: Easy/Short ++: Hard/Long

7.2.2 Characterization of microfluidic platform power and flow rates

The electrochemical reaction of the fuel cell (Eq. 7.1) indicates that CO₂ molecules are produced at the same proportion in which the MeOH molecules are oxidized. Therefore, the current extracted from the fuel cell would determine the pressure in the reaction chamber, as it regulates the number of CO₂ moles produced. For this reason, the relation between the fuel cell output current and the liquid sample flow rate was studied. This characterization was performed with a CHEM micropump because of its higher fabrication simplicity compared to the CHEM-MEMB configuration. The device was designed to hold a sample volume of 30 µl to reduce the duration of the measurements. The geometrical parameters of the fabricated CHEM micropump are shown in Table 7.4.

Table 7.4 Description of the CHEM micropump system used to characterize the flow rates.

Pumping Device	Parameters
	Inlet chamber diameter: 5 mm Sample chamber diameter: 4 mm Outlet chamber diameter: 4 mm Sample volume: 30 µl

The fuel cell was operated at three different output currents while recording the sample flow. The working points were chosen from the polarization curve of the fuel cell (shown in Figure 7.10) as the conditions that yield the maximum power (20 mA), a working point in the ohmic region of the fuel cell curve (10 mA) and a lower current condition where the fuel cell voltage is higher (5 mA). The fluid velocities were determined by two different methods that will be described in the next sections.

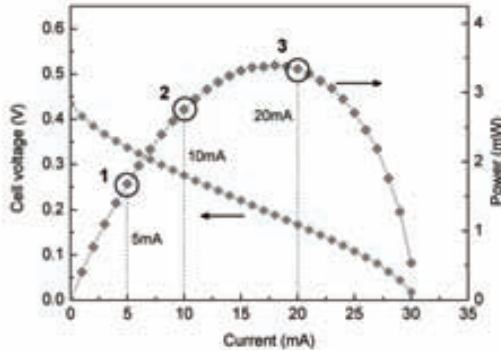


Figure 7.10 Polarization curve from the micro fuel cell used for this study, indicating the output currents with which the characterization was performed.

7.2.2.1 Volume transfer measurement

The average flow rate sustained by the micropump at the different fuel cell currents was obtained measuring the time needed to displace a fixed volume of sample. A fluid volume (V) was injected in the sample chamber using an automated syringe pump. The transference of the fluid from the sample chamber to the output chamber through the microchannel was recorded using a conventional digital video camera (Canon IXUS 120 IS). The total time of transference (t) was taken from the video footage and then used to calculate the average volumetric flow rates (Q) at the given fuel cell current:

$$Q = \frac{V}{t} \quad (7.2)$$

The system was tested five times at each output current and the average time of transference was calculated from the videos. The calculated flow rates and power delivered by the fuel cell at the different conditions are summarized in Table 7.5. Figure 7.11 shows images captured from one of the video recordings at different times of the experiment.

Table 7.5 Flow rates obtained from the videos and power output of the fuel cell.

Fuel Cell Current (mA)	Power (mW)	Sample Volume (μ l)	Time (s)	Average Flow Rate (μ l/min)
5	1.6	30	515 \pm 41	3.5 \pm 0.3
10	2.7	30	268 \pm 15	6.7 \pm 0.4
20	3.2	30	101 \pm 9	17.8 \pm 1.8

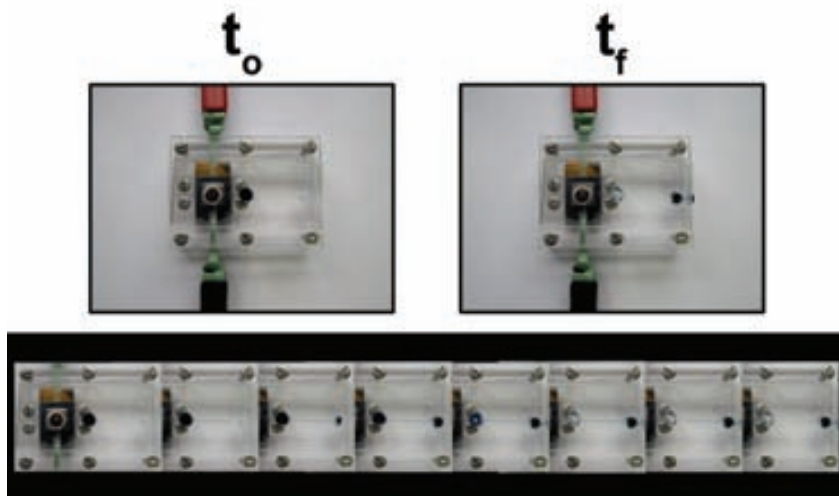


Figure 7.11 Pictures taken from the video footage of the transference of 30 μl of sample.

7.2.2.2 Particle image velocimetry analysis

The flow rate in a microchannel can be characterized by performing a direct measurement of the velocity of micro particles dissolved in the fluid sample. This technique, known as particle image velocimetry (PIV), is used to obtain the instantaneous, spatial measurement of the velocity in a planar section of a flow [28]. The method is based on the analysis of two images taken consecutively with a known interval of time, measuring the distance traveled by one particle in this time.

In the present case, the particle velocimetry was used to verify the flow rate ranges obtained in the previous characterization. Moreover, the validation of this measurement setup would allow its use in further characterizations of the system (e.g. the measurement of a full flow field evolution) or recording the operation of other microfluidic applications using this platform (e.g. cytometry, cell sorting, mixing, etc).

For these experiments, latex particles with a diameter of 25 μm were dissolved in the liquid sample (Milli-Q water). The sample chamber was filled with the solution and the fuel cell was set to work again in a fixed current mode for values of 5, 10 and 20 mA.

An Olympus IX71 inverted optical microscope was used to focus on a section of the microchannel (100 μm height x 200 μm width). The optical high-speed video recording of the flux of the particles was acquired by means of a high-speed CCD camera (Photron FastCam 1024 PCI), working at a rate of 125 frames/s with a shutter speed of 1/5000 s, which was mounted on the microscope. The obtained videos were composed of a series of photographs taken at this high speed.

In this setup only the information in one plane (x-y) could be obtained. The uncertainty of the position of particles in the z-axis led to a dispersion in the obtained values of the particle velocity.

The videos were recorded in time lapses of 20 seconds, taken at a time corresponding to the middle of the measurement, i.e. at half the total time of volume transference obtained in the previous section. A total of ten videos at each fuel cell current were recorded and analyzed. The videos were analyzed in search of particles that flowed within $\pm 25 \mu\text{m}$ the center of the microchannel, where the highest velocity is found in the parabolic laminar flow formed in channels of these dimensions. A mean of 40 particles flowing within this section were counted in each of the videos. The velocity of the selected particles was calculated considering the time difference between two frames and their position in the x-y plane. Figure 7.12 shows extracted frames of the videos from the examined section of the microchannel. The images show particles flowing at the three fuel cell currents.

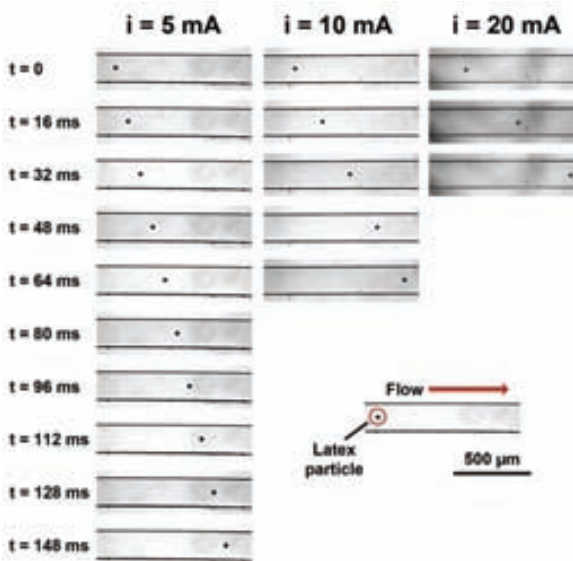


Figure 7.12 Images of the particles trails at different times driven by the pressure produced by the fuel cell working at currents of (a) 5 mA, (b) 10 mA and (c) 20 mA.

After obtaining the particle velocities, an average value of fluid velocity (u_{av}) for each fuel cell current condition was calculated. Assuming that the selected particles were flowing at the maximum velocity (u_{max}), this value was obtained as [29]:

$$u_{av} = \frac{2}{3} u_{max} \quad (7.3)$$

The average volumetric flow rates of the sample in the microchannel were obtained multiplying the average velocities and the channel cross-sectional area ($A = 100 \times 200 \mu\text{m}$):

$$Q = u_{av} A \quad (7.4)$$

The average flow rates of the sample at the different fuel cell current conditions are summarized in Table 7.6.

Table 7.6 Flow rates obtained from the analysis of particle velocity.

Fuel Cell Current (mA)	Power (mW)	Average Velocity (mm/s)	Average Flow Rate ($\mu\text{L}/\text{min}$)
5	1.6	3.9 ± 0.4	4.5 ± 0.5
10	2.7	9.2 ± 1.4	10.8 ± 1.6
20	3.2	18.2 ± 1.5	21.3 ± 1.7

The average flow rates obtained from the recordings of the volume transference and the particle image velocimetry are compared in Figure 7.13.

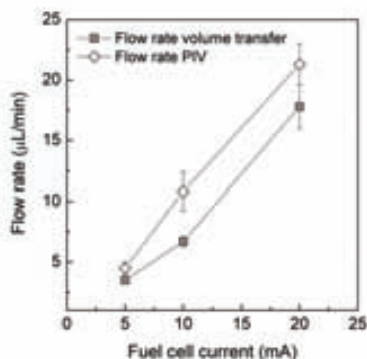


Figure 7.13 Average flow rates with respect to the fuel cell current obtained by two methods.

As it can be seen from the figure, the values of flow rates obtained from both methods show the same trend, the correspondence between the fuel cell current and the sample flow rate follow an almost linear behavior. These results imply that within this range, the flow rate could be accurately adjusted by controlling the output current demanded from the fuel cell.

The error bars in the curve of flow rate calculated from the transference of volume come from the different durations of the measurements. In the case of the flux calculation by particle velocimetry, the error bars are larger because of the uncertainty on the position of the particle in the z-axis of the channel. The discrepancy between the values obtained by the two methods can be attributed to an over estimation of the fluid velocity using the particle velocimetry method. The

videos of particle velocimetry were recorded at a specific moment in the measurement, corresponding to the middle of the volume transference, and only capture a length of 20 seconds of the measurements. Therefore, this method provides an estimation of the flow rate assuming it remains stable along the entire measurement. The difference observed between the methods suggests that the flow rate presents a rather transient behavior, which would have to be taken into account when used in a microfluidic application that requires a specific flow rate at all times.

The power produced by the fuel cell and the magnitude of the flow rate values achieved with this approach lay within the values of interest in a wide range of microfluidic applications [19-21, 30]. Nevertheless, it is important to notice that the fluxes would depend on the particular fluidic resistance of each application. The magnitude of flow rate values obtained in this study correspond to the specific system with which was measured. These values are used here to validate the approach and prove the dependence with the fuel cell current.

As seen in the tables above, the fuel cell was able to deliver an electric power around 1-4 mW, depending on the point of operation, while producing sufficient hydraulic force to pump a fluid through the microchannel. In a practical application, this platform could be used power the analysis or detection modules in a microfluidic system by the electric energy given by the fuel cell, while at the same time use the hydraulic energy to pump the sample through its network.

7.3 DISCUSSION AND SUMMARY

The operation of the fuel cell powered microfluidic platform approach proposed in this chapter was successfully validated. Besides delivering and electric power, a micro direct methanol fuel cell was used to pump a fluid through a microfluidic system. The driving force responsible of making the sample flow in this device is the pressure produced by the CO₂ gas generated in the fuel cell reaction.

The operation was validated with two designs of micropumping systems with the fuel cell working at maximum current regime. A more detailed characterization of one pumping systems allowed demonstrating that the relation between sample flow rate and the current generated by the fuel cell is practically linear. This permits adjusting the desired flow rate for a given application by controlling the fuel cell output conditions.

The hybrid micro fuel cell system presented in Chapter 2 was used to characterize this approach. However, the other micro fuel cell developments described in this thesis could also be applied, combining their advantages to compose a more compact device. Furthermore, the fabrication technology used for the development of the SU-8 fuel cell could be aimed to achieve a Lab-on-a-Chip system with integrated micropump and electric energy source as a fully polymeric device.

Even further ahead, the optimization of the system could allow the fabrication of Lab-on-a-Chip systems where part of the sample to analyze could be used to generate the electric energy and perform pumping functions.

References in Chapter 7.

- [1] Terry S.C., Jerman J.H. and Angell J.B. A gas chromatographic air analyzer fabricated on a silicon wafer *Electron Devices, IEEE Transactions on* **26** (1979) 1880-6
- [2] Petersen K.E. Fabrication of an integrated, planar silicon ink-jet structure *Electron Devices, IEEE Transactions on* **26** (1979) 1918-20
- [3] Gravesen P. and Et Al. Microfluidics-a review *Journal of Micromechanics and Microengineering* **3** (1993) 168
- [4] Shoji S. and Esashi M. Microflow devices and systems *Journal of Micromechanics and Microengineering* **4** (1994) 157
- [5] Manz A., Graber N. and Widmer H.M. Miniaturized total chemical analysis systems: A novel concept for chemical sensing *Sensors and Actuators B: Chemical* **1** (1990) 244-8
- [6] Mark D., Haeberle S., Roth G., Stetten F.V. and Zengerle R. Microfluidic lab-on-a-chip platforms: requirements, characteristics and applications *Chemical Society Reviews* **39** (2010) 1153-82
- [7] Auroux P.-A., Iossifidis D., Reyes D.R. and Manz A. Micro Total Analysis Systems. 2. Analytical Standard Operations and Applications *Analytical Chemistry* **74** (2002) 2637-52
- [8] Reyes D.R., Iossifidis D., Auroux P.-A. and Manz A. Micro Total Analysis Systems. 1. Introduction, Theory, and Technology *Analytical Chemistry* **74** (2002) 2623-36
- [9] Vilkner T., Janasek D. and Manz A. Micro Total Analysis Systems. Recent Developments *Analytical Chemistry* **76** (2004) 3373-86
- [10] Dittrich P.S., Tachikawa K. and Manz A. Micro Total Analysis Systems. Latest Advancements and Trends *Analytical Chemistry* **78** (2006) 3887-908
- [11] West J., Becker M., Tombrink S. and Manz A. Micro Total Analysis Systems: Latest Achievements *Analytical Chemistry* **80** (2008) 4403-19
- [12] Arora A., Simone G., Salieb-Beugelaar G.B., Kim J.T. and Manz A. Latest Developments in Micro Total Analysis Systems *Analytical Chemistry* **82** (2010) 4830-47
- [13] Erickson D. and Li D. Integrated microfluidic devices *Analytica Chimica Acta* **507** (2004) 11-26
- [14] Qin L., Vermesh O., Shi Q. and Heath J.R. Self-powered microfluidic chips for multiplexed protein assays from whole blood *Lab on a Chip* **9** (2009) 2016-20
- [15] Cook-Chennault K.A. and Et Al. Powering MEMS portable devices—a review of non-regenerative and regenerative power supply systems with special emphasis on piezoelectric energy harvesting systems *Smart Materials and Structures* **17** (2008) 043001
- [16] Morse J.D. Micro-fuel cell power sources *International Journal of Energy Research* (2007)
- [17] Ibrahim H., Ilinca A. and Perron J. Energy storage systems - Characteristics and comparisons *Renewable & Sustainable Energy Reviews* **12** (2008) 1221-50
- [18] Tominaka S., Nishizeko H., Mizuno J. and Osaka T. Bendable fuel cells: on-chip fuel cell on a flexible polymer substrate *Energy & Environmental Science* **2** (2009) 1074-7
- [19] Laser D.J. and Santiago J.G. A review of micropumps *Journal of Micromechanics and Microengineering* **14** (2004) R35
- [20] Nguyen N.-T., Huang X. and Chuan T.K. MEMS-Micropumps: A Review *Journal of Fluids Engineering* **124** (2002) 384-92
- [21] Woias P. Micropumps—past, progress and future prospects *Sensors and Actuators B: Chemical* **105** (2005) 28-38
- [22] De Bruijn F.A., Papageorgopoulos D.C., Sitters E.F. and Janssen G.J.M. The influence of carbon dioxide on PEM fuel cell anodes *Journal of Power Sources* **110** (2002) 117-24
- [23] Yan W.-M., Chu H.-S., Lu M.-X., Weng F.-B., Jung G.-B. and Lee C.-Y. Degradation of proton exchange membrane fuel cells due to CO and CO₂ poisoning *Journal of Power Sources* **188** (2009) 141-7

- [24] Prakash S., Mustain W. and Kohl P.A. Carbon dioxide vent for direct methanol fuel cells *Journal of Power Sources* **185** (2008) 392-400
- [25] Meng D.D. and Kim C.J. An active micro-direct methanol fuel cell with self-circulation of fuel and built-in removal of CO₂ bubbles *Journal of Power Sources* **194** (2009) 445-50
- [26] Chan Y.H., Zhao T.S., Chen R. and Xu C. A self-regulated passive fuel-feed system for passive direct methanol fuel cells *Journal of Power Sources* **176** (2008) 183-90
- [27] Lui C., Stelick S., Cady N. and Batt C. Low-power microfluidic electro-hydraulic pump (EHP) *Lab on a Chip* **10** (2010) 74-9
- [28] Westerweel J. Digital Particle Image Velocimetry — Theory and Application. 1993 (Delft, The Netherlands: Delft University)
- [29] Morgan H. and Green N.G. *AC Electrokinetics: colloids and nanoparticles* 2003 (Baldock, Hertfordshire, England: Research Studies Press Ltd)
- [30] Nguyen N.T. and Wereley S.T. *Fundamentals and Applications of Microfluidics* 2002: Norwood: Artech House)

Conclusions

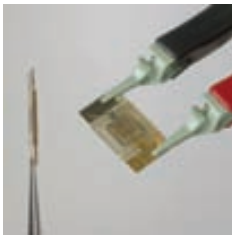
This thesis presents the development of micro fuel cells architectures and components based in technologies compatible with microsystems fabrication. The work includes the design, fabrication and characterization of different approaches. It starts with a hybrid prototype that leads to more compact and integrated designs and ends with the application of the devices to fields of particular interest. In the following, the different contributions of this work to the fuel cell field are presented.



The first development of a micro direct methanol fuel cell using a hybrid approach was tested at different operation conditions and current collector geometry, showing a maximal power density around 12 mW/cm^2 at room temperature. This power density lies within the range obtained for similar devices implemented in the macroscale, which validates the correct function of the miniaturized device. This device was then used as the basis for the consequent developments towards an integrated power source.



A novel and simple approach of a compact micro direct methanol fuel cell was achieved by the combination of a hybrid polymer membrane as an integrable electrolyte with microfabricated silicon current collectors. In this approach, electrodes have been incorporated by electrodeposition techniques. The membrane combines two polymers with different functionalities, Nafion[®] as a proton conducting material and PDMS as a flexible mechanical support. The components proved their operation after being individually characterized and the complete system was capable of generating power. The performance was poor due to the strong contribution of ohmic resistance between electrode and electrolyte. However, this development validated the proof-of-concept towards a compact micro fuel cell device.



An all-polymer micro fuel cell based on SU-8 photoresist was achieved. All fuel cell components (current collectors and MEA) were fabricated with the same material, whose bonding capabilities were exploited to obtain a highly compact device. The integration was achieved in two steps; first, by the embedding of a polymeric electrolyte into a porous SU-8 membrane and second by bonding all SU-8 components together. In this way, the first all-polymeric micro fuel cell was obtained and the drastic reduction of the device dimensions resulted in an increase of more than 50 times the reported volumetric power density.

A fuel delivery component to be incorporated onto a micro fuel cell was designed and fabricated. The main idea was to achieve the lateral fuel feeding and CO₂ degassing in a passive way. In this way, hydrophobic and hydrophilic areas were created in the inner walls of the microfluidic system by topographic modification of the surface. Different polymer micropatterning techniques were used as a way to optimize the device dimensions and reduce materials and production cost. The correct functioning of the fuel delivery system allows envisaging the stacking of the micro fuel cells and their operation with a passive fuel supply.



The hybrid silicon-based micro fuel cell was applied to built a miniaturized microbial fuel cell. The microfabricated device was able to give a remarkable performance due to an efficient biofilm formation on the surface and on the channel walls of the electrodes, showing even an increase in the maximum power density compared to a macro scale device. Furthermore, it was demonstrated that the device could be operated as a toxicity biosensor able to provide an instantaneous response when exposed to the presence of a toxic compound.



The micro direct methanol fuel cell was used to provide both electric and hydraulic power to a microfluidic platform. The pressure produced by the CO₂ gas generated in the fuel cell reaction was used to perform a pumping action. The obtained results showed that the flow rate of the pumped fluid could be accurately adjusted by controlling the output current of the fuel cell. The power produced by the fuel cell and the magnitude of the flow rate values achieved with this approach lay within the values of interest of a wide range of microfluidic applications.



This work represents a significant advance towards the miniaturization of fuel cells, especially with the objective of achieving an overall compact device. This research has required the implementation of micro fuel cell components in silicon compatible materials, dispensing materials with proven effectiveness (e.g. carbon black) due to their incompatibility. Occasionally this resulted in a decrease in the fuel cell performance, which will have to be addressed in a future device optimization. Nevertheless, the obtained results showed a considerable improvement in the volumetric power density, which validates the approach and encourages continuing the work in that direction. Furthermore, it must be highlighted that the use of polymeric materials to the development of micro fuel cells enables the integration of these devices in low cost microsystems markets, such as Lab-on-a-Chip. A particular advantage of this integration has been presented in this thesis, however multiple applications can still be foreseen.

List of publications

During the work of this thesis, the following works have been published:

1. J. P. Esquivel, N. Sabaté, J. Santander, N. Torres and C. Cané
Fabrication and characterization of a passive silicon-based direct methanol fuel cell
Journal of Microsystem Technologies 14 (2008) 535-541
2. D. Davila, J. P. Esquivel, N. Vignes, O. Sanchez, L. Garrido, N. Tomas, N. Sabate, F. J. del Campo, F. J. Munoz and J. Mas
Development and Optimization of Microbial Fuel Cells
Journal of New Materials for Electrochemical Systems 11 (2008) 99-103
3. N.Sabaté, J.P.Esquivel, J.Santander, N.Torres, I.Gràcia, P.Ivanov, L.Fonseca, E.Figueras and C.Cané
Passive Direct Methanol Fuel Cells in Silicon Technology
Journal of New Materials for Electrochemical Systems 11 (2008) 143-146
4. N. Torres, J. Santander, J.P. Esquivel, N. Sabaté, E. Figueras, P. Ivanov, L. Fonseca, I. Gràcia and C. Cané
Performance optimization of a passive silicon-based micro-direct methanol fuel cell
Sensors and Actuators B: Chemical, 132/2 (2008) 540-544
5. J.P. Esquivel, N. Sabaté, A. Tarancón, N. Torres-Herrero, D. Dávila, J. Santander, I. Gràcia and C. Cané
Hybrid polymer electrolyte membrane for silicon-based micro fuel cells integration
Journal of Micromechanics and Microengineering 19 (2009) 065006
6. J.P. Esquivel, N. Sabaté, J. Santander, N. Torres-Herrero, I. Gràcia, P. Ivanov, L. Fonseca and C. Cané
Influence of current collectors design on passive micro direct methanol fuel cell performance
Journal of Power Sources 194 (2009) 391-396
7. N.Torres, M. Duch, J. Santander, N. Sabate, J.P. Esquivel, A. Tarancon and C. Cane
Porous Silicon Membrane for Micro Fuel Cell Applications
Journal of New Materials for Electrochemical Systems 12 (2009) 93-96

- 8.** Tarancón, N. Sabaté, A. Cavallaro, I. Gràcia, J. Roqueta, I. Garbayo, J. P. Esquivel, G. Garcia, C. Cané and J. Santiso
Residual Stress of Free-Standing Membranes of Yttria-Stabilized Zirconia for Micro Solid Oxide Fuel Cell Applications
Journal of Nanoscience and Nanotechnology 10 (2010) 1-11
- 9.** J.P. Esquivel, T. Senn, P. Hernández-Fernández, J. Santander, M. Lörger, S. Rojas, B. Löchel, C. Cané, N. Sabaté
Towards a compact SU-8 micro direct methanol fuel cell
Journal of Power Sources 195 (2010) 8110-8115
- 10.** T. Senn, J.P. Esquivel, M. Lörger, N. Sabate and B.Löchel
Replica molding for multilevel micro-nanostructure replication
Journal of Micromechanics and Microengineering 20 (2010) 115012
- 11.** T. Senn, Ch. Waberski, J. Wolf, J.P. Esquivel, N. Sabaté, B. Löchel
3D structuring of polymer parts using thermoforming processes
Microelectronic Engineering, DOI:10.1016/j.mee.2010.08.003
- 12.** D. Dávila, J.P. Esquivel, N. Sabaté and J. Mas
Microbial fuel cell-based toxicity biosensor
Biosensors and Bioelectronics, DOI:10.1016/j.bios.2010.10.025

APPENDIX

Table I. Physicochemical properties.

Parameter	Symbol	Value
Diffusion coefficient of methanol in water	$D_{MeOH,l}$	$10^{(-5.4163-(999.778/T))}$ m ² /s
Effective diffusion coefficient of methanol in water	$D_{MeOH,l,eff}$	$D_{MeOH,l} \varepsilon^{1.5}$ m ² /s
Diffusion coefficient of methanol in membrane	$D_{MeOH,m}$	$4.9 \times 10^{-10} \exp(2436(1/333 - 1/T)) \xi$ m ² /s
Diffusion coefficient of carbon dioxide in water	$D_{CO_2,l}$	1×10^{10} m ² /s
Effective diffusion coefficient of carbon dioxide in water	$D_{CO_2,l,eff}$	$D_{CO_2,H_2O} \varepsilon^{1.5}$ m ² /s
Binary diffusivity O ₂ -N ₂	$D_{O_2-N_2}$	$0.22 \times 10^{-4} (T/293.2)$ m ² /s
Binary diffusivity O ₂ -H ₂ O	$D_{O_2-H_2O}$	$0.282 \times 10^{-4} (T/308.1)$ m ² /s
Binary diffusivity H ₂ O-N ₂	$D_{H_2O-N_2}$	$0.256 \times 10^{-4} (T/307.5)$ m ² /s
Effective binary diffusivity O ₂ -N ₂	$D_{O_2-N_2,eff}$	$D_{O_2-N_2} \varepsilon^{1.5}$ m ² /s
Effective binary diffusivity O ₂ -H ₂ O	$D_{O_2-H_2O,eff}$	$D_{O_2-H_2O} \varepsilon^{1.5}$ m ² /s
Effective binary diffusivity H ₂ O-N ₂	$D_{H_2O-N_2,eff}$	$D_{H_2O-N_2} \varepsilon^{1.5}$ m ² /s
Thermal diffusion coefficient	D_i^T	0
Porosity of catalyst layer	ε	0.3
Methanol molar weight	M_{MeOH}	0.032 kg/mol
Carbon dioxide molar weight	M_{CO_2}	0.044 kg/mol
Water molar weight	M_{H_2O}	0.018 kg/mol
Oxygen molar weight	M_{O_2}	0.032 kg/mol
Nitrogen molar weight	M_{N_2}	0.028 kg/mol
Density of methanol	ρ_{MeOH}	790 kg/m ³
Density of air	ρ_{air}	1.2 kg/m ³
Density of carbon dioxide gas	$\rho_{CO_2(g)}$	1.87 kg/m ³
Density of carbon dioxide liquid	$\rho_{CO_2(l)}$	705 kg/m ³
Electro-osmotic drag coefficient of water	$n_d^{H_2O}$	2.5

Transfer coefficient of anode	α_a	0.239
Transfer coefficient of cathode	α_b	0.875
Reference exchange current density on anode	i_{a0}	$94.25\exp((35570/R)(1/353-1/T)) \text{ A/m}^2$
Reference exchange current density on cathode	i_{c0}	$0.04222\exp((73200/R)(1/353-1/T)) \text{ A/m}^2$
Electrical conductivity of catalyst	σ_{cat}	1000 S/m
Proton conductivity of membrane	κ_m	12.3 S/m
Thermodynamic potential of methanol oxidation	φ_{eq}^a	0.03 V
Thermodynamic potential of oxygen reduction	φ_{eq}^c	1.24 V
Carbon dioxide saturation concentration	$C_{CO_2(l)}^{sat}$	28.41 mol/m ³
Carbon dioxide saturation mass fraction	$\omega_{CO_2(l)}^{sat}$	$C_{CO_2(l)}^{sat} M_{CO_2} / 1000 \text{ kg/kg}$
Correction factor	ζ	1.5

Table II. Baseline conditions

Parameter	Name	Value
Operating temperature	T	298 K
Gas constant	R	8.314 J/K·mol
Faraday constant	F	96485 C/mol
Oxygen inlet mass fraction	$\omega_{O_2}^{ref}$	0.23 kg/kg
Water cathode inlet mass fraction	$\omega_{H_2O}^{ref}$	0.00343 kg/kg
Reference pressure	P_{ref}	$1.013 \times 10^5 \text{ Pa}$
Reference concentration of methanol	$C_{MeOH_{ref}}$	1000, 2000, 4000 mol/m ³
Membrane thickness	d_m	$115 \times 10^{-6} \text{ m}$
Catalyst layer thickness	d_{ACL}, d_{CCL}	$40 \times 10^{-6} \text{ m}$
Channel height	d_{AC}, d_{CC}	$200 \times 10^{-6} \text{ m}$
Channel section (quarter)		$40 \times 10^{-6} \text{ m}$
Shoulder section (quarter)		$80 \times 10^{-6} \text{ m}$

Resumen en español

En esta tesis se presentan los primeros desarrollos y contribuciones tecnológicas al campo de micro pilas de combustible llevados a cabo en el IMB-CNM (CSIC). En particular, este trabajo está dedicado al estudio de pilas de combustible microfabricadas como fuentes de energía para microsistemas. Esta tesis se compone de siete capítulos: el capítulo de introducción y seis capítulos experimentales divididos en tres secciones.

La primera sección (Capítulo 2) consiste en el desarrollo de una micro pila de combustible de metanol directo utilizando un enfoque híbrido, es decir, los colectores de corriente se han fabricado en silicio con el uso de tecnologías de microfabricación, mientras que los electrodos y electrolito son componentes comerciales. Esta es una primera aproximación en el desarrollo de micro pilas de combustible con el fin de identificar y medir los efectos que más influyen sobre el rendimiento del dispositivo llevado a la microescala. La pila de combustible es medida bajo diferentes condiciones de operación tales como concentración de metanol, temperatura y orientación del dispositivo. Por otra parte, se explora el efecto de la geometría de los colectores de corriente y la eficiencia del dispositivo. Por último, un modelo de la pila de combustible con elementos finitos, transitorio y en tres dimensiones fue construido como una herramienta para predecir el rendimiento del dispositivo cuando se modifican diferentes parámetros.

La segunda sección presenta las estrategias realizadas respecto a la integración de todos los componentes de la micro pila hacia un dispositivo más compacto utilizando tecnologías de microfabricación compatibles. Estos métodos incluyeron el uso de diferentes técnicas de microestructuración de polímeros como una manera de optimizar las dimensiones del dispositivo, así como la reducción de costes de los materiales y producción.

El enfoque presentado en el Capítulo 3 consiste, por un lado, en la adición del electrodo en los colectores de corriente microfabricados incorporando una fina rejilla de silicio que contiene los catalizadores. Por el otro lado, la membrana de Nafion® utilizada anteriormente es sustituida por una membrana de electrolito polimérico híbrida compuesta por una matriz de PDMS rellena del polímero conductor protónico. La ventaja de este enfoque se basa en la capacidad del PDMS para unirse al silicio por medio de oxidación por plasma, lo que permite el montaje de todos los componentes en un dispositivo muy compacto.

Un segundo enfoque, que se describe en el Capítulo 4, hace uso de la resina fotocurable SU-8 para fabricar todos los componentes de la micro pila de combustible. En este caso, las estructuras de resina de los colectores de corriente y la matriz de la MEA fueron realizadas por medio de fotolitografía UV, para luego ser funcionalizadas. Los colectores de corriente fueron metalizados para proporcionar la conducción eléctrica, la matriz de la MEA fue rellena con electrolito polimérico y luego cubierta con las capas de catalizador. Aprovechando las capacidades de

pegado del SU-8, los componentes fueron ensamblados por medio de prensado térmico, logrando una micro pila de combustible plana totalmente polimérica.

El capítulo 5 describe un sistema de suministro de combustible obtenido mediante técnicas de fabricación de polímeros que puede ser incorporado sobre una micro pila de combustible para facilitar la distribución de fluidos de forma pasiva y permitir el futuro ensamblado de varios dispositivos en *stack*. En este componente, la distribución del combustible se realiza definiendo áreas super-hidrofóbicas por medio de la microestructuración de su superficie. De esta forma fue posible la reproducción de estructuras tridimensionales en varios niveles mediante un proceso de fabricación rápido y escalable.

La tercera sección presenta dos aplicaciones a los desarrollos de micro pilas de combustible. El capítulo 6 presenta una biopila de combustible microfabricada utilizando microorganismos como biocatalizadores de compuestos orgánicos. El efecto de la reducción de las dimensiones del dispositivo fue evaluado y comparado con un dispositivo de escala macro. Además, el microdispositivo fue utilizado para evaluar su capacidad para trabajar como un biosensor microfabricado midiendo la variación de la señal de salida después de la exposición de los microorganismos a un material tóxico.

El Capítulo 7 describe el funcionamiento de una plataforma microfluídica alimentada por una micro pila de combustible. Además de suministrar energía eléctrica, una micro pila de combustible de metanol directo se utiliza para bombear un líquido a través de un sistema microfluídico. La fuerza responsable de hacer fluir la muestra a través del dispositivo es la presión producida por el gas de CO₂ generado en la reacción de la pila de combustible. Estas ventajas proporcionadas por la pila de combustible durante su operación pueden ser de gran interés para aplicaciones de microfluídica.

Por último, este trabajo finaliza con unas conclusiones que resumen los resultados presentados. En esta última sección, la dirección de los trabajos futuros y en curso son también comentadas.

List of abbreviations

μ-TAS: Micro Total Analysis System

AC: Anode Channel

ACL: Anode Catalyst Layer

AFC: Alkaline Fuel Cell

BCE: Bis-Cycloaliphatic Epoxide

BioFC: Biological Fuel Cell

BOD: Biochemical Oxygen Demand

BOP: Balance of Plant

CC: Cathode Channel

CCD: Charge-Coupled Device

CCL: Cathode Catalyst Layer

CNC: Computer Numerical Control

CV: Cyclic Voltammogram

CHP: Combined Heat and Power

DET: Direct Electron Transfer

DGE-BPA: Diglycidyl Ether of Bis-phenol A

DMFC: Direct Methanol Fuel Cell

DNA: Deoxyribonucleic acid

DRIE: Deep Reactive Ion Etching

DVE-TEG: Divinylether of Triethylene Glycol

EIS: Electrochemical Impedance Spectroscopy

GDL: Gas Diffusion Layer

GPS: Global Positioning System

LIGA: Lithographie, Galvanoformung, Abformung (Lithography, Electroplating, and Molding)

MCFC: Molten Carbonate Fuel Cell

MEA: Membrane Electrode Assembly

MEMS: Micro Electro-Mechanical Systems

MeOH: Methanol

MET: Mediated Electron Transfer

MFC: Microbial Fuel Cell

MR: Methanol Reservoir

NEMS: Nano Electro-Mechanical Systems

NiMH: Nickel-Metal Hydride

OCV: Open Circuit Voltage

PAFC: Phosphoric Acid Fuel Cell

PDMS: Polydimethylsiloxane

PEM: Proton Exchange Membrane or Polymer Electrolyte Membrane

PEMFC: Polymer Electrolyte Membrane Fuel Cell or Proton Exchange Membrane Fuel Cell

PIV: Particle Image Velocimetry

PMMA: Polymethylmethacrylate

PS: Polystyrene

RF: Radio Frequency

SEM: Scanning electron microscope

SOFC: Solid Oxide Fuel Cell

SOI: Silicon-On-Insulator

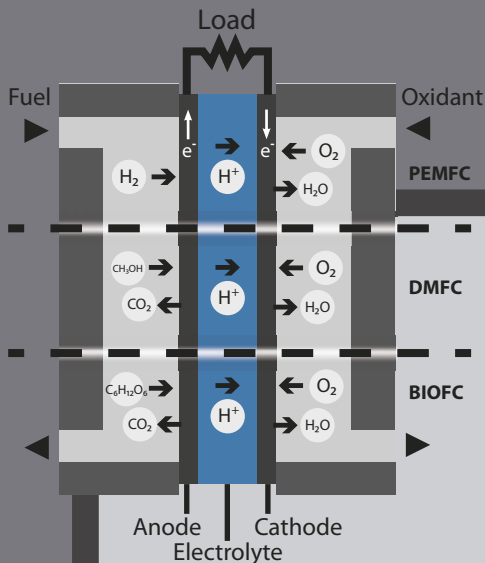
TAS: Triaryl Sulfonium Salt

UV: Ultraviolet

UV-NIL: Ultraviolet-Nanoimprint Lithography

Epílogo

Esta tesis ha salido de esta forma debido a una serie de afortunadas circunstancias entre las que se pueden mencionar: la mecatrónica, la Mercè, el bocadillo con tomate sin tomate, el rosado, los palillos para presionar micropilas, el Piano Bar Regina, las tlayudas, el baile del panda, las pizzas con *feliz cumple* de pimiento, las clases de sax que todavía no empiezan, los viajes (en combi sobre todo), los festivales, los concursos de pintxos, el nado de mariposa, el patxaran y el queso idiazabal, las tardes de MACBA, las carreras de 10K por la ciudad, el campamento volley playa Pals, el baile dormido, las flammkuchen, los jueves cerveceros, step, toe, stamp, stomp, shuffle, ballchange, los interminables calçots, todas las personas con las que compartí piso durante estos años, las innumerables visitas, el *camino*, los conciertos, los roadtrips ibéricos, los duraznos en almíbar, los chakas y las historias de siempre, la tartaleta de escalivada y foie caramelizado, el pa amb tomaquet, la alhambra mezquita y las tapas gratis, el döner groß, santa Eulalia...



The increasing complexity of portable electronic devices demands energy sources that meet the requirement of delivering a high power density within a reduced size, and in many cases the possibility of achieving complete integration. In this sense, an intense research effort has been focused towards the miniaturization of powering devices in a wide variety of technologies. A similar trend has been followed in the micro electromechanical systems (MEMS) technology field, where the smart-system concept has impelled the development of a new generation of powering

devices, such as batteries, fuel cells or energy harvesters, which altogether are known as powerMEMS. Among the different energy generation systems, micro fuel cells have received special attention due to their particular features, i.e. high energy density, non-toxic emissions and the possibility of avoiding movable parts simplifying the fabrication process and reducing the risk of failure. Polymer electrolyte membrane fuel cells (PEMFCs) are particularly attractive due to their capability of working at room temperature using both hydrogen and liquid fuels. The possibility to operate using liquid fuels, such as methanol or organic compounds, represent an important advantage for portable applications due to the great simplification of fuel storage and handling processes.

This thesis presents the first developments and technological contributions to the micro fuel cell field performed at IMB-CNM (CSIC). Particularly, this work is dedicated to the design and fabrication of microfabricated fuel cells as power sources to be integrated within the microsystems to be powered. The work is organized in seven chapters: one introductory chapter and six experimental chapters that have been divided in three sections.

The first section describes the development of a micro direct methanol fuel cell using a hybrid approach, which was used to identify and measure the effects that influence the most on the device performance at a microscale. The second section presents different strategies regarding the integration of all micro fuel cell components into a more compact device by taking advantage of microfabrication compatible technologies. These approaches involved the use of different polymer micropatterning techniques as a way to optimize the device dimensions and reduce materials and production cost. Finally, the third section presents two particular applications of the developed micro fuel cells, a microfabricated bio fuel cell using microorganisms as biocatalysts of organic compounds and a fuel cell powered microfluidic platform that can be of great interest for Lab-on-a-Chip or micro Total Analysis Systems (μ TAS).